

**Application of managed dyke realignment and hydrodynamic modelling
for flood mitigation in Truro, Nova Scotia**

By
Julia Purcell

A Thesis Submitted to
Saint Mary's University, Halifax, Nova Scotia
in Partial Fulfillment of the Requirements for
the Degree of Master of Science in Applied Science.

December, 2020, Halifax, Nova Scotia

Copyright Julia Purcell, 2020

Approved:	Dr. Danika van Proosdij Supervisor
Approved:	Dr. Ryan Mulligan Co-Supervisor
Approved:	Tony Bowron Supervisory Committee Member
Approved:	Dr. Aldona Wiacek Supervisory Committee Member
Approved:	Dr. Barret Kurylyk External Examiner
Date:	December 22, 2020

**Application of managed dyke realignment and hydrodynamic modelling
for flood mitigation in Truro, Nova Scotia**

By Julia Purcell

Abstract

Managed dyke realignment (MR) is to be implemented at a 92-hectare restoration site in the Salmon River Estuary to restore tidal wetland habitat and to help mitigate flooding in Truro. This research examines the accuracy of a hydrodynamic model, predicted flooding within the restoration site and the estuary's response to MR. Field surveys were conducted to update river bathymetry, and water level and current measurements were collected over several tidal cycles for model calibration and validation. The model successfully reproduced measured water levels, the timing of tides and the tidally-dominated velocity profiles in the channel compared to the field measurements. Modelled water levels in the channel decreased by up to 31.9 cm under the MR scenario, indicating the potential for flood reduction in Truro. The predicted spreading of slow-moving floodwater within the site suggests the potential for net sedimentation followed by halophytic vegetation establishment, indicating net positive benefits of MR.

December 22, 2020

Acknowledgements

I would like to acknowledge everyone who played a role in my academic accomplishments. First and foremost, I want to thank my supervisors, Dr. Danika van Proosdij and Dr. Ryan Mulligan. Both of you have gone above and beyond to provide endless guidance, academically and personally, support, patience and knowledge that have significantly helped me push through my graduate degree. I will be forever grateful and would not have finished this thesis without either of you. You both bring so much to the table in many different ways. I would also like to thank Tony Bowron and Dr. Aldona Wiacek for completing my supervisory committee, guiding me in the right direction along the way, taking the time to meet for progress reports and for reading my extremely long thesis. Additionally, I would like to thank Dr. Barret Kurylyk for agreeing to be my external examiner on such short notice.

Next, I want to thank those individuals who worked behind the scenes in the making of this thesis, but were able to provide me with incredible assistance, support and guidance. I want to send a huge thank you to the In_CoaST crew: Emma Poirier, Logan Horrocks, Larissa Sweeney, Sam Cunningham and Blandine Reivillo. I really appreciate your help in the field with deploying and programming instruments, transferring all those ISCO water samples (192 in total) to other containers after each tide, taking detailed notes, keeping on schedule and, of course, for trudging through the mud with me. I want to say thank you to Danika, again, for her participation and contribution to all aspects of the required fieldwork, especially for towing our HydroSurveyor with a kayak in a very fast, turbulent river. I also want to thank Greg Baker and Reyhan Akyol, from MP_SpARC, for conducting my surveys with a remotely piloted aircraft. I want to thank

Greg again, and Ray Jahncke, for their assistance with creating my digital elevation model and helping me navigate through ArcMap. Thank you to Jennie Graham and Tony, from CBWES, for providing me with information, datasets and updates on the progress of the managed realignment project in Truro. I also want to thank the other master's students in our lab who weathered this storm with me for the past few years, especially Graeme Matheson for passing on his wisdom.

Next, I want to thank the individuals from NSDA, NSTIR, NSE, CBWES, CBCL Limited and Saint Mary's University for their collaboration on the managed realignment project in Truro. A special thanks to Ryan, again, at Queen's University for doing the preliminary modelling for this project and providing me with a head start on my own modelling for this thesis. Without the group of you, the topic of my thesis would be something completely different.

On a personal note, I want to thank my family, including my mom (Shannon), dad (Paul), brother (Ian), nana (Helen), papa (Ken) and aunts (Lee and Shelley) for their love, support, patience and encouragement. Even though I did not seem appreciative at the time, I truly did appreciate every single push, word of advice, pep talk and check-in to see how I was progressing and handling things. All of you were there for me and I love you all so much. Thank you to my friends as well for the exact same thing.

Lastly, I want to thank the Natural Sciences and Engineering Research Council of Canada (NSERC), the Canada Foundation for Innovation (CFI), the province of Nova Scotia and Saint Mary's University for their financial support.

Table of Contents

Abstract	i
Acknowledgements	ii
List of Tables	vi
List of Figures	vii
Chapter 1 – Introduction	1
1.1. Climate Change Impacts on Coastal Communities	1
1.2. Motivation and Purpose	4
1.3. Managed Realignment	7
1.3.1. Purpose and Function	7
1.3.2. History and Lessons Learned from Other Sites	8
1.3.3. Stages of Managed Realignment	11
1.3.4. Successful Tidal Wetland Restoration	13
1.4. Tidal Wetlands as Coastal Defense Mechanisms	15
1.5. Morphodynamics of Tidal Wetlands and the Surrounding Environment in a Macrotidal, Tide-Dominated Estuary	19
1.5.1. Components of a Macrotidal, Tide-Dominated Estuary	19
1.5.2. Physical Characteristics of a Tidal Wetland	22
1.5.3. Hydrodynamics	22
1.5.4. Sediment Dynamics	25
1.5.6. Response of an Estuary to Physical Alterations	27
1.6. Hydrodynamic Models	29
Chapter 2 – Study Area	33
2.1. Geographical Setting	33
2.2. History of the Study Area	35
2.3. Managed Realignment Design	37
Chapter 3 – Methods	39
3.1. Experimental Design	39
3.2. Field Data Collection	40
3.2.1. Hydrodynamics	40
3.2.2. Surveying	47
3.3. Hydrodynamic Modelling with Delft3D	54
3.3.1. Model Description	54
3.3.2. Model Setup	55

3.3.3. Model Runs	60
Chapter 4 – Results	65
4.1. Field Data	65
4.2. Model Results.....	80
4.2.1. Response of the Model to Changes in Bathymetric Parameters	80
4.2.2. Impact of Increasing Water Levels on Modelled Flood Extent within the Restoration Site.....	96
4.2.3. Spatial Distribution of Modelled Currents at the Restoration Site	103
4.2.4. Flood Statistics for the Restoration Site.....	112
4.2.5. Water Levels Before and After Breaching the Dykes.....	118
Chapter 5 – Discussion	122
5.1. Delft3D was successful at simulating hydrodynamic conditions in the Salmon River Estuary and simulated minor differences from making realistic changes in bathymetry and bottom roughness	122
5.2. Detailed hydrodynamic modelling of a macrotidal estuarine system requires detailed field measurements to validate and increase confidence in model results	125
5.3. Delft3D predicted extensive flooding within the restoration site during high spring tides with simulated currents that suggest the potential for net sediment deposition.....	128
5.4. Modelled water levels in the main river channel decreased in the scenario with dykes breached at the restoration site	130
5.5. Model Limitations and Recommendations for Future Work	131
Chapter 6 – Conclusion.....	136
References.....	138
Appendices.....	155
Appendix A.....	155
Appendix B	157
Appendix C	159
Appendix D.....	161
Appendix E	163
Appendix F.....	172
Appendix G.....	176
Appendix H.....	177
Appendix I	179
Appendix J	182

List of Tables

Table 1.1. Tidal cycles in the upper Bay of Fundy (modified from Desplanque & Mossman, 2004).....	23
Table 3.1. The four measured and modelled tides, their predicted high tide times (in ADT and GMT) and their predicted tidal ranges (in CD) at Burntcoat Head. The information in this table was acquired from Fisheries and Oceans Canada (2018).....	40
Table 3.2. Instruments and their surveyed locations (in UTM coordinates) and surveyed elevations (in CGVD28). The ADVs/OBSs were surveyed at the sample point and the pressure sensor of the two ADVs. The ADCPs and ISCOs were surveyed at the transducer head and the bottom of the nozzle, respectively.	43

List of Figures

Figure 1.1. Stages of managed realignment for climate change adaptation and tidal wetland restoration (used with permission from TransCoastal Adaptations: Centre for Nature-Based Solutions, 2019).	12
Figure 1.2. Conceptual drawing of a tidal wetland's adaptive capability to vertically accrete sediment and keep pace with sea level rise (modified from van Wesenbeeck et al., 2017).	16
Figure 1.3. Conceptual drawing of a tidal wetland's ability to reduce waves with different heights to almost similar heights (modified from van Wesenbeeck et al., 2017).	17
Figure 1.4. Vertical profile of flow speed passing through and above a tidal wetland canopy near Cedar Creek, Florida (modified from Leonard & Luther, 1995).	18
Figure 1.5. The Salmon River Estuary in the Bay of Fundy (modified from Dalrymple et al., 2012). BLC = bedload convergence.	20
Figure 1.6. Observed (measured) flow velocities (red and green) compared with modelled velocities (black and grey) for different bottom roughness scenarios in Delft3D (modified from Ashall et al., 2016).	32
Figure 2.1. The study area and restoration site in the inner Salmon River Estuary. The inset shows a satellite image of the Bay of Fundy and the relative location of the study area. The satellite image was taken by Joshua Stevens at the NASA Earth Observatory (2019).	34
Figure 2.2. The final managed realignment design for the Onslow-North River restoration site along the Salmon River and North River in Truro (used with permission from CBWES).	38
Figure 3.1. Locations of hydrodynamic instruments and water samplers in the Salmon River and North River.	42
Figure 3.2. (a) ADV 1 + OBS 1 deployed on the south side of the Salmon River at low tide. (b) ADV 2 + OBS 2 deployed on the north side of the Salmon River at low tide. The instrument had to be braced and secured to handle the high currents at this location. (c) ADCP 1 deployed on the south side of the Salmon River near the Highway 102 Bridge at low tide. (d) ADCP 2 deployed on the north side of the North River near the CN Rail Bridge at low tide. (e) ISCO 1 setup on the north side of the Salmon River. The camera was facing upstream towards the Highway 102 Bridge. (f) ISCO 2 setup on the south side of the North River. The camera was facing upstream towards the CN Rail Bridge.	44
Figure 3.3. The HydroSurveyor TM mounted on the HydroBoard being towed by a kayak in the Salmon River.	48
Figure 3.4. (a) Adjusting the tripod of the base station positioned on top of a dyke. This photo was taken on August 12, 2018. (b) A closer view of the HydroSurveyor TM mounted on the HydroBoard. This photo was taken on June 27, 2018.	48
Figure 3.5. HydroSurveyor TM sampling paths for all three data collection days.	50
Figure 3.6. Grids flown by an RPA (DJI Phantom [®]) to capture ground elevation of mudflats at low tide. Grids were flown over a span of three days (August 14, August 16 and August 17, 2018). GCPs are numbered and symbolized as red triangles. The red boxes represent each flight grid. Map created by Greg Baker and Reyhan Akyol, MP_SpARC, Saint Mary's University, 2018.	51

Figure 3.7. Flow diagram illustrating the steps taken to create the 2018 DEM in ArcMap™. SM is short for tidal wetland and IDW is short for inverse distance weighted.	52
Figure 3.8. Spatial representation of the different data collection methods used to retrieve elevations and the resolutions for the updated 2018 DEM.	53
Figure 3.9. The full model domain as illustrated by the input DEM. Blue colours represent lower elevations and red colours represent higher elevations. The inset shows the study area with the model grid overtopping the input DEM. Open boundaries of the model grid are represented by the three red lines labelled A, B and C.	56
Figure 3.10. Predicted tide elevations (in MSL) from WebTide.	59
Figure 4.1. The 2013 DEM (a), the 2018 DEM (b) and elevation differences between the two DEMs (c). Elevations are presented in CGVD28.	66
Figure 4.2. Water depths relative to the pressure sensor (a) and speeds (b) measured at the location of ADCP 1 for all four tides.	68
Figure 4.3. Water depths (a), u-component of velocities (b) and flow directions (c) measured at the location of ADCP 1 for Tide 1. The u-component of velocity is parallel to the river channel, which was oriented approximately 45° in the upstream positive x-direction. For flow direction, 0° represents north and increases clockwise. The vertical black dashed line represents the approximate time of high tide.	69
Figure 4.4. U-component of velocities measured at the location of ADCP 1 for all four tides. Tide 1 (a) occurred on August 12, Tides 2 (b) and 3 (c) occurred on August 13 and Tide 4 (d) occurred on August 14, 2018. The u-component of velocity was parallel to the river channel in the along-channel x-direction. The vertical black dashed lines represent the approximate time of high tide for each tide.	71
Figure 4.5. Water depths ((a) and (b)), speeds (a) and average signal strengths (b) measured at ADCP 1 and suspended sediment concentrations (c) measured at ISCO 1 for Tide 1. The vertical black dashed line represents the approximate time of high tide.	73
Figure 4.6. Mean water depths, mean resolved horizontal velocities, mean suspended sediment concentrations, mean turbulent kinetic energies and mean shear velocities at the location of ADV 1 + OBS 1 for all four tides.	75
Figure 4.7. Box and whisker plot of suspended sediment concentration over all four tides at the locations of ISCO 1 (a) and ISCO 2 (b). The boxes represent the interquartile range, the horizontal lines within the boxes represent the median concentrations of the datasets for a given time, the ‘x’ markers represent mean concentrations and the dots at the ends of the bottom and top whiskers represent the minimum and maximum concentrations of the datasets for a given time, respectively. The grey boxes indicate that no data were collected for that period of time. Note the difference in scale between the two y-axes.	78
Figure 4.8. Measured (black line) and modelled water levels (in CGVD28) and magnitude of depth averaged velocities at the location of ADCP 1. The two models used a bottom friction coefficient (C_D) of 0.002. The red line represents the model results simulated using the 2018 DEM and the blue line represents the model results simulated using the 2013 DEM.	81
Figure 4.9. Measured (black line) and modelled water levels (in CGVD28) and magnitude of velocities at the location of ADV 1 + OBS 1. The two models used a bottom friction coefficient (C_D) of 0.002. The red line represents the model results	

simulated using the 2018 DEM and the blue line represents the model results simulated using the 2013 DEM.	84
Figure 4.10. Measured (black line) and modelled water levels (in CGVD28) at the location of ADV 2 + OBS 2. The two models used a bottom friction coefficient (C_D) of 0.002. The red line represents the model results simulated using the 2018 DEM and the blue line represents the model results simulated using the 2013 DEM.	86
Figure 4.11. ADV 2, and the attached OBS 2, tilted in the upstream direction in the Salmon River at low tide after Tide 1.	87
Figure 4.12. Measured (black line) and modelled water levels (in CGVD28) and magnitude of depth averaged velocities at the location of ADCP 1. The two models used the 2018 DEM. bottom friction coefficient (C_D) of 0.002. The red line represents the model results simulated using a bottom friction coefficient (C_D) of 0.002 and the green line represents the model results simulated using a bottom friction coefficient (C_D) of 0.001. The asterisk (*) indicates that the model results were generated after adjusting water levels at the tidal boundary to match measured water levels.	89
Figure 4.13. Measured (black line) and modelled water levels (in CGVD28) and magnitude of velocities at the location of ADV 1 + OBS 1. The two models used the 2018 DEM. The red line represents the model results simulated using a bottom friction coefficient (C_D) of 0.002 and the green line represents the model results simulated using a bottom friction coefficient (C_D) of 0.001. The asterisk (*) indicates that the model results were generated after adjusting water levels at the tidal boundary to match measured water levels.	90
Figure 4.14. Measured (black line) and modelled water levels (in CGVD28) at the location of ADV 2 + OBS 2. The two models used the 2018 DEM. The red line represents the model results simulated using a bottom friction coefficient (C_D) of 0.002 and the green line represents the model results simulated using a bottom friction coefficient (C_D) of 0.001. The asterisk (*) indicates that the model results were generated after adjusting water levels at the tidal boundary to match measured water levels.	91
Figure 4.15. Modelled magnitude of depth averaged velocities at the beginning of the flood tide for Tide 2. Model results were simulated using the 2018 DEM and a bottom friction coefficient of 0.002. The black line represents the existing dyke infrastructure with no breaches.	93
Figure 4.16. The Salmon River near ADCP 1 and ISCO 1 before (a) and after (b) the tidal bore passed through. In the photos, upstream is left and downstream is right.	94
Figure 4.17. Modelled magnitude of depth averaged velocities during the flood tide of Tide 1. Model results were simulated using the 2018 DEM and a bottom friction coefficient of 0.002. The black line represents the existing dyke infrastructure with no breaches.	95
Figure 4.18. Modelled water depths with a maximum tide height of 9.6 m (in CGVD28) at the approximate time of high tide during Tide 2.	97
Figure 4.19. Modelled water depths with a maximum tide height of 9.65 m (in CGVD28) at the approximate time of high tide during Tide 2.	99
Figure 4.20. Modelled water depths with a maximum tide height of 9.7 m (in CGVD28) at the approximate time of high tide during Tide 2.	100
Figure 4.21. Modelled water depths with a maximum tide height of 9.75 m (in CGVD28) at the approximate time of high tide during Tide 2.	101

Figure 4.22. Modelled water depths with a maximum tide height of 9.8 m (in CGVD28) at the approximate time of high tide during Tide 2.....	102
Figure 4.23. Modelled water depths (a) and magnitude of depth averaged velocities (b) with a maximum tide height of 9.6 m (in CGVD28). Model results are for Tide 2 and are shown 40 minutes before high tide. Arrows show the direction of flow.....	105
Figure 4.24. Modelled water depths (a) and magnitude of depth averaged velocities (b) with a maximum tide height of 9.6 m (in CGVD28). Model results are for Tide 2 and are shown 10 minutes before high tide. Arrows show the direction of flow.....	107
Figure 4.25. Modelled water depths (a) and magnitude of depth averaged velocities (b) with a maximum tide height of 9.6 m (in CGVD28). Model results are for Tide 2 and are shown 20 minutes after high tide. Arrows show the direction of flow.....	109
Figure 4.26. Modelled water depths (a) and magnitude of depth averaged velocities (b) with a maximum tide height of 9.6 m (in CGVD28). Model results are for Tide 2 and are shown 140 minutes after high tide. Arrows show the direction of flow.....	111
Figure 4.27. Modelled water depths with calculated flood volume, flood area, average water depth and maximum water depth values within the restoration site at the approximate time of high tide for Tide 2. Maximum tide height at high tide was 9.6 m (in CGVD28).....	113
Figure 4.28. Modelled water depths with calculated flood volume, flood area, average water depth and maximum water depth values within the restoration site at the approximate time of high tide for Tide 2. Maximum tide height at high tide was 9.8 m (in CGVD28).....	115
Figure 4.29. Flood volume, flood area, average water depth and maximum water depth at the managed realignment site for each 5-cm increment in maximum tide height. A bottom friction coefficient of 0.002 was selected for these models, the 2018 DEM was used and the results shown are those simulated for Tide 2 at the approximate time of high tide. Maximum tide height is in CGVD28. Note the difference in scale for the two axes in the bottom panel.....	117
Figure 4.30. Modelled water levels (in CGVD28) at five different locations throughout the Salmon River over four spring tides. The black line represents the results of the no-breach scenario and the red line represents the results of the breach scenario. The two variations of the 2018 DEM were used for these simulations and a bottom friction coefficient of 0.002 was used for both model runs.....	119
Figure 4.31. Approximate locations of points selected to compare water levels simulated for the non-breach scenario and the breach scenario. Average changes in water level over all four simulated tides are also included. The hatched area is the restoration site.	120

Chapter 1 – Introduction

1.1. Climate Change Impacts on Coastal Communities

One of the greatest challenges communities, natural systems, coastal habitats and infrastructure are currently facing is a changing climate unnaturally accelerated by anthropogenic emissions of potent greenhouse gases, such as carbon dioxide and methane (Intergovernmental Panel on Climate Change [IPCC], 2014). Apart from rising global mean temperature and changing precipitation patterns, the other most notable consequence of the earth's warming climate is rapid sea level rise, caused by the melting of continental glaciers and polar ice sheets and thermal expansion of warming oceans (Weissenberger & Chouinard, 2015). The mean rate of global-averaged sea level rise was 1.7 ± 0.2 mm/year between 1901 and 2010 and 3.2 ± 0.4 mm/year between 1993 and 2010, indicating an increase in rates of sea level rise in recent years (IPCC, 2014). Post-glacial rebound is a process that also contributes to increasing sea level (Greenberg et al., 2012). For example, retreat of the glacier centered in Hudson Bay, Canada, at the end of the last ice age caused the center of the continent to rise and the coast of the continental shelf to fall (Greenberg et al., 2012). Another consequence of climate change is the increase in storm frequency and intensity, which has already been detected in many parts of the world (IPCC, 2014). The areas that are most at risk to sea level rise, and periodic storm surges, are those along the coast.

Coastal zones are the interface between land and ocean, exposing them to coastal processes. However, low-lying coastal zones, and the communities within, are most vulnerable. Although coastal communities have been coping with dynamic coastal processes for thousands of years (Singh et al., 2007), they, along with the rest of the

world, are now experiencing climate change at an accelerating rate, so it will be even more challenging to adapt to these changes. According to the Intergovernmental Panel on Climate Change (IPCC) Response Strategies in the First Assessment Report (1990) and reiterated in the Fifth Assessment Report (Wong et al., 2014), there are three categories of adaptation strategies for sea level rise: accommodation, protection, and retreat.

Under the accommodation category, coastal communities continue to occupy and use the land that is vulnerable to flooding or damage by altering their infrastructure to a more adaptable state (IPCC, 1990). For example, the elevation of residential and small commercial buildings on pilings for flood protection, drainage system modification, and growing saltwater-tolerant crops instead of traditional crops are all examples of accommodation strategies (IPCC, 1990).

Traditional adaptation strategies that fall under the protection category include the construction of seawalls, dykes, and levees, which act as coastal barriers to prevent inundation, tidal flooding, wave impact on infrastructure, shore erosion, and loss of natural resources (Singh et al., 2007; IPCC, 1990). These traditional coastal barriers are drawn from an array of ‘hard’ engineering solutions, meaning they are solid, man-made structures that prevent the passing of water (IPCC, 1990). Unfortunately, these structures traditionally fail and require maintenance over time because of erosion or deterioration due to incoming waves and other forces exerted by water or land-based freshwater flow (Morris et al., 2018).

The last category of adaptation strategies for sea level rise is retreat, which refers to moving inhabitants and infrastructure from vulnerable areas near the coastline to lower risk areas further inland (IPCC, 1990). Selecting this option means that coastal

communities either abandon or relocate some of their structures and land, such as residential buildings and agricultural fields, respectively. However, it is often the most sustainable option and can provide extra protection if planned and managed properly (Temmerman et al., 2013; Ruckelshaus et al., 2016). For example, the failure of a dyke can lead to inundation of agricultural land and subsequent loss of crops, but it can also lead to the restoration of a tidal wetland within the floodplain. Advantages of this include the provision of habitats for animals and plants that are ecologically and economically important, sequestering carbon and other nutrients and filtering upland and runoff waters from pollutants (Propato et al., 2018). In this scenario, the community can change the location of the dyke by constructing a new dyke further inland (retreat) and rely on the restored tidal wetland to protect the new dyke and, by extension, the remaining land and structures behind it.

Conventional ‘hard’ coastal engineering is perceived as the solution to combat flood risks, yet it is often unsustainable as it runs into issues of continual and costly maintenance, such as heightening and widening the existing coastal barriers to keep up with increasing flood risk (Temmerman et al., 2013). In recent years, there has been a transition from the large-scale practice of ‘hard’ engineering to ‘soft’ engineering, or nature-based adaptation (Temmerman et al., 2013; Sierra-Correa and Kintz, 2015; Cheong et al., 2013; Harman et al., 2013). Instead of always using hard coastal engineering structures to adapt, experts are now starting to enhance and utilize natural assets (i.e., tidal wetlands) to provide those same services, often with added benefits (Ruckelshaus et al., 2016). According to Rahman et al. (2019), common examples of this include the creation of natural foreshore tidal marsh habitat by realigning existing coastal

defense lines (i.e., managed realignment), planting along shorelines and restoring tidal wetlands. In contrast to conventional ‘hard’ coastal engineering, these nature-based coastal adaptation strategies typically include the restoration of large wetlands between rivers and human settlements, which can provide extra water storage, reduce flood risks in populated areas and slow down flood propagation (Temmerman et al., 2013).

Additionally, restored wetlands have a high capacity for sediment deposition (Vandenbruwaene et al., 2011), allowing them to grow vertically in the tidal frame, which can potentially keep up with the rising sea level. The ability of a restored wetland to be largely self-sustaining and cost-efficient (Temmerman et al., 2013), by naturally being able to grow vertically and migrate landward in response to sea-level rise, makes nature-based coastal adaptation a growing and popular option that could change the way society adapts.

1.2. Motivation and Purpose

The motivation for this research derives from the frequent occurrence and consequences of flooding in Truro, Nova Scotia. Truro is a rural town located in the innermost reaches of the Bay of Fundy that experiences flooding almost every year (Marvin & Wilson, 2016). Although these flood events are mainly attributed to heavy rainfall, they are often a result of complex interactions between high Bay of Fundy tides, ice jamming, dyke presence and location, high river flows and floodplain infilling (Marvin & Wilson, 2016).

Unfortunately, because of its location along the floodplain of the Salmon River Estuary and its low-lying urban development, there will always be a risk of flooding within the floodplain and Truro will likely continue to flood as a result (CBCL Limited,

2017). To help understand the problem better and potentially alleviate some of the risk, a comprehensive flood risk study was conducted by CBCL Limited (2017) looking at over 40 flood scenarios and options that may reduce the level of risk. These scenarios were modelled to obtain a comprehensive understanding of the complex processes that cause flooding, and different mitigation options were compared to help identify the one(s) that would be most cost-effective, provide the most protection, forfeit the least amount of land and have the least environmental impact (CBCL Limited, 2017). As a result, CBCL Limited (2017) had identified the managed realignment of dykes as one of the most realistic options to reduce the impacts of flooding by increasing the natural capacity of the floodplain. Managed dyke realignment, in this scenario, is defined as the construction of new dykes further inland followed by the deliberate breaching or decommissioning of existing dykes to restore floodplain area. This would allow for the diversion of some floodwater (from the ocean and rivers) to the floodplain instead of flooding the town. Implementation of this flood mitigation option, in addition to the installation of water pumps, would provide an approximate 30% reduction in priority areas that currently experience flooding (CBCL Limited, 2017). Although Truro will always be at risk, reducing the current flood area in town by approximately 30% would better ensure public safety and minimize flood damage in the future.

In response to the initial draft of the flood risk study, a project emerged as a collaboration between Nova Scotia Department of Agriculture (NSDA), Nova Scotia Transportation and Infrastructure Renewal (NSTIR), Nova Scotia Environment (NSE), CB Wetlands & Environmental Specialists Inc. (CBWES), and the Intertidal Coastal Sediment Transport (In_CoaST) Research Unit at Saint Mary's University to employ

managed dyke realignment as a flood mitigation strategy (Sherren et al., 2019). The project involves the construction of two new inland dykes and excavation of drainage channels at the restoration site, building two new aboiteaux (i.e., one-way flood gates), upgrading one aboiteau, eliminating three aboiteaux, extending an existing culvert with an added gate and the decommissioning of approximately 3 km of the existing dyke structure. Prior to construction, preliminary hydrodynamic modelling was done to determine the best managed realignment design out of those that were drafted using river conditions and a digital elevation model (DEM) from 2013.

The purpose of this thesis is to better understand the dynamics of the Salmon River Estuary with field measurements, to investigate the response of a validated hydrodynamic model (Delft3D) to changes in bathymetry and bottom roughness, to use that model to determine the flood extent and velocities at a restoration site, with updated river bathymetry, along the Salmon River and North River in Truro and to examine how simulated water levels change after breaching the dykes according to the managed realignment design. This type of research in this particular river system is important because the bathymetry changes so dramatically. Not only do larger morphological features change year by year, but bed level elevations change season by season, and sometimes even over the course of a single tide (Crewe, 2004).

This thesis aims to explore and answer the following research questions:

1. What are the water levels, velocities and suspended sediment concentrations in the Salmon River and North River within the study area?
2. How do modelled water levels and velocities generally change in response to a change in:

- a. The model bathymetry/DEM?
 - b. The bottom friction coefficient of the model?
3. What is the model prediction of the flood extent and spatial distribution of flow velocities at the restoration site and surrounding estuarine environment with the dykes breached and aboiteaux removed according to the managed realignment design?
4. How do water levels change downstream of, adjacent to and upstream of the restoration site after the dykes are breached in the model?
5. What are the general implications and considerations for management and decision-making that can be derived from the model results for a managed realignment or tidal wetland restoration project?

1.3. Managed Realignment

1.3.1. Purpose and Function

Managed realignment is more generally defined as a hybrid engineering technique that involves the deliberate breaching and retreat of a coastal barrier, creating space for coastlines to evolve into intertidal habitats more naturally (Esteves, 2014). This technique has been implemented worldwide along vulnerable coastlines for climate change adaptation and tidal wetland restoration (e.g., Boone et al., 2017; Friess et al., 2014; Garbutt et al., 2006; Watts et al., 2003). However, this thesis investigates the application of managed realignment for the purpose of flood mitigation and will provide insight into how well this technique can mitigate flood events.

In the case of flood mitigation in Truro, managed dyke realignment will function by allowing tidal water to infiltrate an area of the floodplain and restoring it back to its natural state as a tidal wetland, which acts as its own line of defense against flooding. It will also allow for the drainage of freshwater from the associated watershed, through two new aboiteaux and a hybrid creek network flowing into three primary channels connected to the main river, after intense rainfall events or snow melt in the spring. These are the two main ways in which the managed realignment project will mitigate flooding in Truro.

1.3.2. History and Lessons Learned from Other Sites

The first managed realignment projects emerged in the 1980s in France, Germany, and the Netherlands, and only in the early 2000s became an important climate change adaptation mechanism (Esteves, 2014). One of the first managed realignments, and one of the more well-studied sites in the literature, is that in Tollesbury, Essex, UK (Garbutt et al., 2006). Tollesbury is in southeast England and the realignment site is located within the Blackwater estuary. This managed realignment project was implemented as a test case to remove uncertainties about returning agricultural land to intertidal habitat in a macrotidal (tidal range >4 meters) environment (Garbutt et al., 2006). A single 60-meter section of the original sea defense was breached in 1995, allowing 21 hectares of arable land to flood with saltwater (Garbutt et al., 2006). Managed realignment success depends on the ability of the soil within the restoration site to resist erosion by waves and tidal currents, allowing the accretion of sediment, and subsequently, vegetation establishment (Watts et al., 2003). Sedimentation must also occur at a rate equal to or greater than mean sea level rise for managed realignment success (Watts et al., 2003), otherwise, the

floodplain will eventually become permanently inundated and fail to provide coastal protection. At Tollesbury, the predicted sea level rise relative to the land surface is up to 6 mm/year (Watts et al., 2003). In the case of the Tollesbury realignment, the floodplain quickly accreted intertidal mudflats, with constant and relatively high mean sedimentation rates of 23 mm/year from 1995 to 2001 (Garbutt et al., 2006). Within the first year, tidal wetland species began colonizing the floodplain, and by 2001, a dense colonization of 15 species of tidal wetland vegetation were recorded (Garbutt et al., 2006). Because sedimentation rates were consistently greater than the predicted rate of sea level rise and vegetation colonized the floodplain, the managed realignment at Tollesbury was considered successful.

Another European example is the managed realignment project in Freiston Shore, UK, which began in 2002 and was monitored until 2008 (Friess et al., 2014).

Unfortunately, this project was not as successful as the one in Tollesbury because the dimensions of the breaches caused Freiston Shore's tidal prism to increase by 776,398 m³, which caused significant channel erosion (Friess et al., 2014). The tidal prism is the volume of water moving past a location during each half tidal cycle (Dalrymple et al., 2012). The establishment of water surface slopes, which create high flow velocities and extensive pooling within the floodplain contributed to channel erosion as well (Friess et al., 2014). The erosional response was so significant that within 2.5 months of breaching the sea defense, the channels that were initially excavated within the breaches increased in width by up to 960% (Friess et al., 2014). The lessons learned from this study were that one must have a comprehensive understanding of the processes that occur in each unique coastal system, through hydrodynamic modelling, and that sea defense breaches

must be carefully designed prior to implementing any managed realignment scheme in the future.

In response to the large amount of research and implementation of managed realignment projects in Europe, other regions around the world began to experiment with this technique along their coastlines as well, especially the United States (Esteves, 2014; Williams & Orr, 2002). In Canada, however, managed realignment is a fairly new practice. Tidal wetland restoration projects in Atlantic Canada, with a focus on habitat restoration, have grown over the past two decades, most of which were in the Bay of Fundy (Bowron et al., 2012; Boone et al., 2017). CBWES implemented managed realignment at Walton in 2005 (Neatt et al., 2013), Cogmagun in 2009 (Bowron et al., 2015a) and St. Croix in 2009 (Bowron et al., 2015b) by breaching dykes, but these restorations did not include the building of new dykes. Another example is the managed realignment of dykes at Fort Beauséjour in Aulac, New Brunswick. The goal of this project was to restore tidal wetland habitat in two adjacent sections of the floodplain, but it was not solely to test the effectiveness of managed realignment as a tidal wetland restoration technique. The dykes were starting to fail from erosion due to high relative exposure to waves (Boone et al., 2017), hence, one of the reasons why this site was chosen for managed realignment. Breaching of the dykes began in 2010 and tidal wetland restoration was monitored until 2015 (Boone et al., 2017). After breaching the dykes, the northwest section showed steady vegetation recovery (indicative of a high and steady rate of sedimentation), but the southeast section showed little vegetation growth (Boone et al., 2017). This was most likely because the southeast section had lower initial surface elevations and a much higher rate of sediment deposition resulting in a soft

unconsolidated surface (Boone et al., 2017). However, these results were expected based on previous empirical work done at the site and the two-dimensional hydrodynamic model used to properly implement a successful breach design that met the required project criteria (Boone et al., 2017).

Overall, these examples showed that managed realignment can be successful, but only if one understands how the system will respond to future environmental conditions and can utilize other tools (e.g., hydrodynamic models) to test designs for successful managed realignments. Regardless, the key message is that for a managed realignment project to succeed as a climate change adaptation technique, successful tidal wetland restoration must occur for it to function effectively as a form of coastal protection.

1.3.3. Stages of Managed Realignment

In the case of managed realignment, because each case is different in terms of geography and governance, there is no official set of guidelines available. However, there are some key stages of managed realignment that one would typically follow for climate change adaptation and tidal wetland restoration. These stages are: (1) Engage, (2) Gather Baseline, (3) Design, (4) Implement, and (5) Monitor, as shown in Figure 1.1 below.

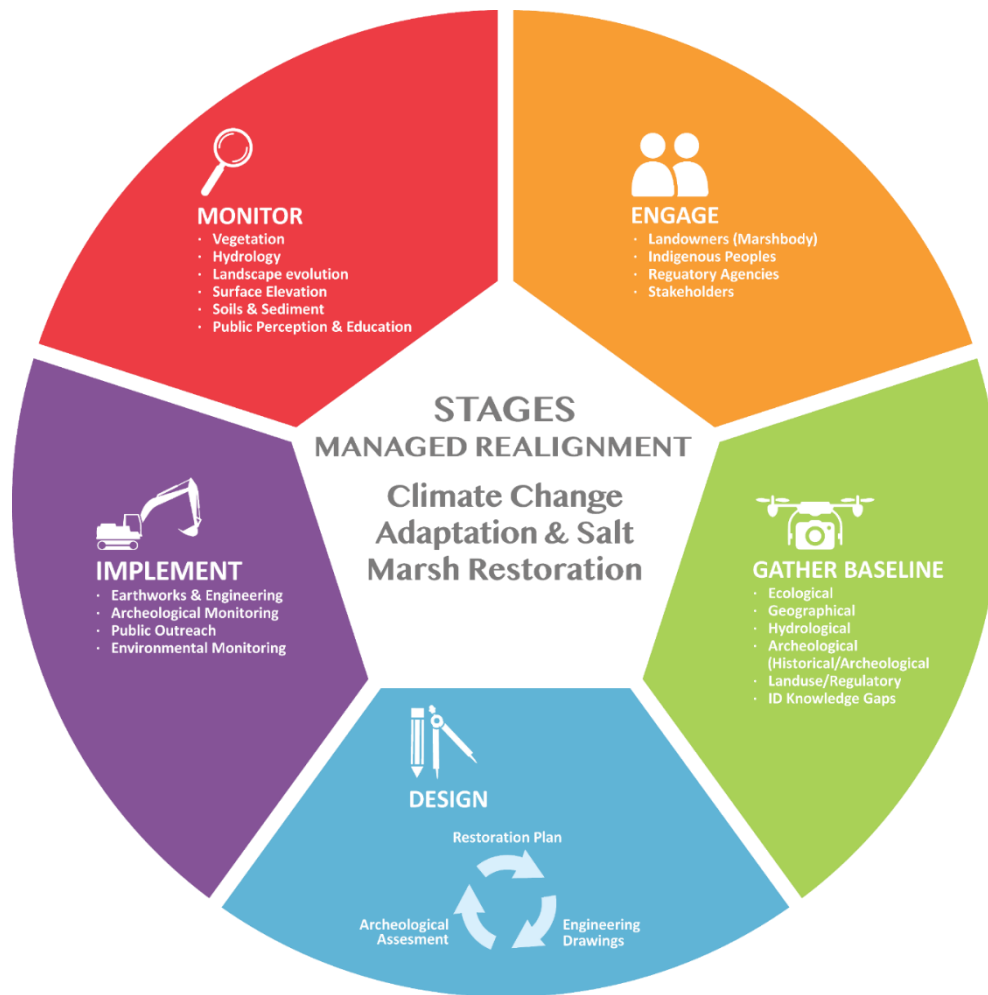


Figure 1.1. Stages of managed realignment for climate change adaptation and tidal wetland restoration (used with permission from *TransCoastal Adaptations: Centre for Nature-Based Solutions*, 2019).

The first stage, “Engage”, involves communication with proprietors (the Marsh Body), Indigenous peoples, regulatory agencies and stakeholders. In this stage, these individuals are informed of the idea of managed realignment, and they are given the opportunity to raise concerns, ask questions and provide input on the project as it develops. The second stage, “Gather Baseline”, refers to the collection of baseline data near the managed realignment and restoration site. The purpose of this is to create a better understanding of the site in terms of its ecology, geography, hydrology, archaeology, land

use and identifying any knowledge gaps. The third stage, “Design”, involves the cyclic process of creating the restoration plan (i.e., managed realignment design), drawing up engineering plans for construction and an archaeological assessment. The fourth stage, “Implement”, is the part of the process when site construction occurs (e.g., building inner dykes and breaching outer dykes), along with archaeological and environmental monitoring and public outreach. The last stage, “Monitor”, includes monitoring the site after construction by keeping an eye on how well and where vegetation establishes, how hydrology is restored, landscape evolution, surface elevation changes, where soils and sediment either deposit or erode and public perception and education. These five stages generalize the processes involved in managed realignment projects and are meant to educate those who are interested in managed realignment or who plan to implement it.

One key component that is not explicitly shown in Figure 1.1, but is critical for implementation and managed realignment/restoration design, is hydrodynamic modelling. The modelling part of the process would occur within the “Gather Baseline” and “Design” stages. It would occur here because some of the baseline data are required to initiate and calibrate the model. The model may then inform the realignment and restoration design.

1.3.4. Successful Tidal Wetland Restoration

Once managed realignment has been implemented, there are two approaches to the restoration of wetland habitat: (1) a passive approach, relying heavily on natural processes to restore the sites, but only when there is a high level of confidence in the outcome and (2) an active approach, which involves interventions within the site to

ensure successful restoration (Almeida et al., 2017). This section will briefly cover the conditions that lead to successful tidal wetland restoration.

The key indicator of tidal wetland restoration success is the colonization of appropriate tidal wetland vegetation. For vegetation to establish, there are certain conditions that must be met within the restoration site. The first condition is that rates and patterns of sediment accumulation and erosion must be suitable for each individual restoration site (Spencer & Harvey, 2012). For instance, excess accumulation can result in the burial of seedlings, while excess erosion may affect seed retention (Spencer & Harvey, 2012). Additionally, if sedimentation rates are too high, the surface may become too soft and unconsolidated for seeds to settle long enough to germinate, as was the case at the managed realignment site in Aulac, New Brunswick in the initial years (Boone et al., 2017).

Another key condition, and one mentioned in multiple studies (Erfanzadeh et al., 2010; Spencer & Harvey, 2012; Wolters et al., 2005; Wolters et al., 2008), is the ability of tidal wetland species to reach and colonize the restoration site. The concept being referred to is the species pool concept, which describes all species available that could potentially colonize and inhabit a habitat area (Wolters et al., 2005). The existence of an already established tidal wetland adjacent to a restoration site is vital for fast vegetation colonization and greater colonization success because the seed source is a short distance away from the restoration site (Wolters et al., 2008; Erfanzadeh et al., 2010). These two conditions are crucial for vegetation colonization.

1.4. Tidal Wetlands as Coastal Defense Mechanisms

Tidal wetlands are vegetated platforms that establish in intertidal zones of temperate coastal areas and are sheltered enough to permit the deposition of fine sediments and establish halophytic vegetation (Woolnough et al., 1995; Allen, 2000). Because tidal wetlands establish in intertidal zones, they are naturally exposed to ocean water, which means there are certain climate change stressors they must face, like rising sea levels. Evidence shows that sea level rise does not necessarily lead to loss of tidal wetland area because some can migrate landward and/or maintain their elevation with respect to sea level as they accrete sediment vertically (Erwin, 2009), however, this is not the case for all tidal wetlands. For those that do not have space to accommodate landward migration and/or do not have the sediment supply to keep up with sea level rise, coastal squeeze is the greatest threat (Borchert et al., 2018). Tidal wetlands can be squeezed between rising sea level and hard infrastructure (i.e., dykes, causeways and other forms of development), resulting in the loss of tidal wetland habitat (Borchert et al., 2018). Other climate change stressors, such as temperature increases and substantial changes in precipitation rates, can dramatically affect tidal wetlands as well (Erwin, 2009). Overall, tidal wetlands are vulnerable to climate change, but if managed properly, they can be great tools for climate change adaptation and mitigation. As explained previously, one such technique that restores and utilizes tidal wetlands for coastal protection is managed realignment.

As mentioned earlier, one indicator of managed realignment success is sediment accretion rates on the marsh platform that can keep up with or exceed rates of sea level rise (Morris et al., 2002). This is illustrated in Figure 1.2.

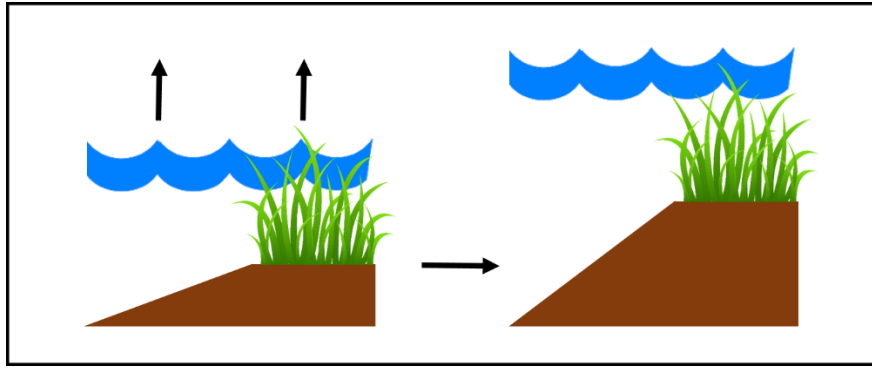


Figure 1.2. Conceptual drawing of a tidal wetland's adaptive capability to vertically accrete sediment and keep pace with sea level rise (modified from van Wesenbeeck et al., 2017).

However, the main component of a tidal wetland that provides coastal defense is its vegetation, which has been found to dampen (attenuate) wave energy, reducing its impact on coastal barriers, and decrease flow velocities (Cranford et al., 1989; Leonard & Luther, 1995; Möller et al., 1999; van Proosdij et al., 2006; Leonard & Croft, 2006; Neumeier & Amos, 2006; Vuik et al., 2016; Narayan et al., 2016; van Wesenbeeck et al., 2017).

Surface waves, which also propagate throughout the water column, can lose a significant amount of energy when passing through a vegetated tidal wetland due to depth-induced wave breaking, frictional forces along the bed, and friction drag forces applied by vegetation stems (Vuik et al., 2016). The greater the stem diameter, height, and density of the vegetation, the greater the energy loss and wave attenuation. Figure 1.3 illustrates this, as well as showing that vegetation can dampen waves of different incoming heights, over a certain distance, to almost similar heights (van Wesenbeeck et al., 2017). This is because wave attenuation is proportional to the incoming wave height

(van Wesenbeeck et al., 2017). With this ability, tidal wetlands can reduce the impact of incoming waves on coastal barriers, such as a dyke.

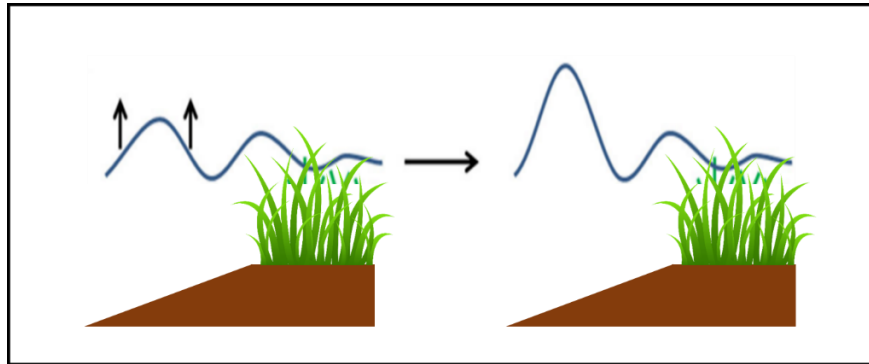


Figure 1.3. Conceptual drawing of a tidal wetland's ability to reduce waves with different heights to almost similar heights (modified from van Wesenbeeck et al., 2017).

The same principle of energy extraction applies to incoming tides or high flow velocities. Figure 1.4 illustrates the vertical profile of measured flow speed as it passes through and above a tidal wetland canopy.

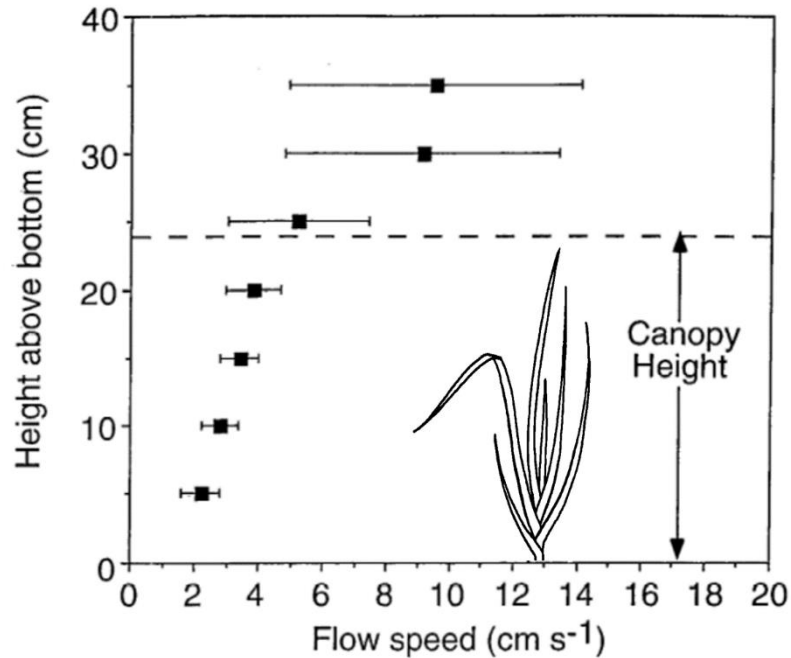


Figure 1.4. Vertical profile of flow speed passing through and above a tidal wetland canopy near Cedar Creek, Florida (modified from Leonard & Luther, 1995).

The concern with the scenario in Figure 1.4 is the unobstructed flow (i.e., skimming flow) above the canopy, which occurs in tidal wetlands where maximum water height is higher than the maximum canopy height. If vegetation is fully submerged, skimming flow can develop immediately downstream of the vegetation edge and increase the further inland it travels (Neumeier, 2007). In this case, skimming flow creates high unobstructed flow velocities above the canopy that are still able to reach coastal barriers and potentially cause damage. However, this would only be the case if the entire tidal wetland platform had a low profile continuing back to the coastal barrier. If a tidal wetland increased in elevation from the low marsh platform to the high marsh platform closer to the coastal barrier, vegetation on the high marsh platform could still dissipate the skimming flow before reaching the coastal barrier (Neumeier & Amos, 2006).

Regardless of the above, vegetated foreshores of tidal wetlands are still effective at wave attenuation, sediment capture, vertical accretion, erosion reduction and the mitigation of storm surge and debris movement (Vuik et al., 2016; Spalding et al., 2014), making them critical climate change mitigation and adaptation tools. This also emphasizes the benefits of nature-based infrastructure, which includes the restoration of tidal wetland area by managed realignment, either on its own or in conjunction with more conventional engineering methods. However, to properly design and understand the response of any managed realignment project, one needs to understand the broader scale morphodynamics in estuaries in general, as well as those modified by human activity.

1.5. Morphodynamics of Tidal Wetlands and the Surrounding Environment in a Macrotidal, Tide-Dominated Estuary

1.5.1. Components of a Macrotidal, Tide-Dominated Estuary

According to Dalrymple (2006, p. 11), “an estuary is a transgressive coastal environment at the mouth of a river, that receives sediment from both fluvial and marine sources, and that contains facies influenced by tide, wave and fluvial processes”. A macrotidal estuary is one which has a tidal range greater than 4 meters (Dalrymple et al., 2012). The Salmon River Estuary is one such estuary and is illustrated in Figure 1.5 along with the different zones of a typical macrotidal estuary. From downstream to upstream, the zones are elongate tidal bars, braided sand flats and tidal-fluvial channel; the latter of which includes the bedload convergence zone and the tidal limit.

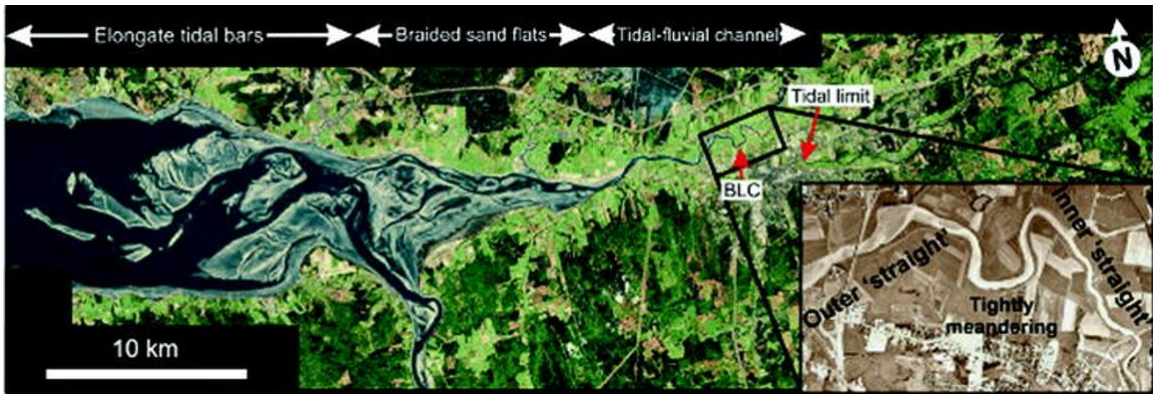


Figure 1.5. The Salmon River Estuary in the Bay of Fundy (modified from Dalrymple et al., 2012). BLC = bedload convergence.

In general, tide-dominated estuaries are characterized by a funnel-shaped geometry with a high width-to-depth ratio (Wells, 1995). Tidal sand ridges with superimposed sand waves are perhaps the most pronounced morphological feature of tide-dominated estuaries (Wells, 1995). They are oriented roughly parallel to the axis of main tidal flow (Wells, 1995). Another common feature is the flanking tidal wetlands with incised tidal channels (Wells, 1995).

For the Salmon River Estuary, the elongate tidal bars separate a complex system of channels in the outer estuary. In general, the bars lie roughly parallel to the main flood and ebb currents of a tide and can range from 1 to 15 km in length and a few hundred meters to about 4 km in width (Dalrymple et al., 2012; Wells, 1995). Bars are commonly asymmetric, shaped by the stronger of the ebb and flood currents, and because the elongate tidal bars exist in the outer estuary, where there is overall flood dominance, the steeper side of the bars typically face the direction of the flood currents (Dalrymple et al., 2012).

Typically, in most tide-dominated estuaries, there is a transition between the zone of elongate tidal bars and the narrower inner part of the estuary, where the channel becomes simpler (Dalrymple et al. 2012; Wells, 1995). In the case of the Salmon River Estuary, there exists a unique braided sand flat area between the zone of high relief elongate tidal bars and the inner estuary with a single channel (Dalrymple et al., 2012; Dalrymple et al., 1990). According to Dalrymple et al. (2012), the braided sand flat zone exists due to the shallowness of the estuary, very strong tidal currents and fine sand. However, unlike the elongate tidal bars, the braided sand flats are subtle (Dalrymple et al., 2012).

In the inner estuary, the tidal-fluvial channel zone exists, which includes the bedload convergence zone and the tidal limit. This zone encompasses the length of the estuary from where the tidal limit is upstream to where the channel significantly widens downstream (Dalrymple et al., 2012). The tidal limit is the furthest upstream point in the estuary that tidal water reaches at high tide. Generally coinciding with the tidal-fluvial channel zone is the bedload convergence zone, characterized by the ‘straight’ – meandering – ‘straight’ channel pattern (shown in Figure 1.5). In the bedload convergence zone, bedload material transport from the fluvial portion of the estuary (material moving downstream) tends to equal bedload material transport from the tidal portion of the estuary (material moving upstream) in the long term (Dalrymple et al., 2012; Dalrymple et al., 1992). This is generally a low-energy zone and typically contains the finest-grained bedload sediment present in the estuary (Dalrymple et al., 1992).

All tide-dominated estuaries tend to exhibit the zones and characteristics described above (Wells, 1995), except for the braided tidal flats which seem to be unique to the Salmon River Estuary (Dalrymple et al., 2012).

1.5.2. Physical Characteristics of a Tidal Wetland

Tidal wetlands consist of two main geomorphological elements: (1) a vegetated platform, and (2) a network of tidal channels or creeks (Allen, 2000). The vegetated platform exists high in the tidal frame and is regularly flooded by the tide (Allen, 2000). The vegetation itself is halophytic, meaning it is able to grow in waters of high salinity (salt-tolerant) and can extend upward to tidal freshwater (Woolnough et al., 1995; Allen, 2000).

The tidal creeks within a tidal wetland form a network that functions to distribute tidal water and suspended sediment over the marsh platform (Allen, 2000). The evolution of these tidal wetland creeks is largely determined by the tidal prism (Friedrichs & Perry, 2001). The tidal prism is the volume of water moving past a location during each half tidal cycle (Dalrymple et al., 2012).

1.5.3. Hydrodynamics

The hydrodynamics of an estuary are heavily influenced by the morphology of the estuary and can, in return, influence further evolution of the estuary itself (Friedrichs & Perry, 2001). The primary hydrodynamic components are tides and tidal currents. Wind-driven currents and storm surge are excluded in this thesis due to their episodic and unpredictable nature.

Tides are the alternating and predictable rise and fall of sea level due to gravitational forces exerted on the earth by the moon and sun (Desplanque & Mossman, 2004; Desplanque & Mossman, 2001), although they can be influenced by meteorological forces as well, such as atmospheric pressure and strong winds (Allen, 2000). The rising tide is the flood tide, the falling tide is the ebb tide and the moment at which the tide transitions from flood to ebb is called slack tide (Wolanski & Elliott, 2015).

Tides are either diurnal (occur once daily), semi-diurnal (occur approximately twice daily) or mixed and vary over time based on hundreds of different constituents (Pugh & Woodworth, 2014; Kidd, 2016). Tidal constituents are sinusoidal waves and are smaller components superimposed on each other to create the tide (Kidd, 2016). There are many complex interactions between different tidal constituents that can create repeat tidal cycles. The most common of these cycles are summarized in Table 1.1.

Table 1.1. Tidal cycles in the upper Bay of Fundy (modified from Desplanque & Mossman, 2004).

Cycle	Period	Approximate tidal range
1. Diurnal cycle due to relation of Moon to Earth	0.517 days (12 hr 25 min)	11.0 m
2. Spring/neap cycle	14.77 days	13.5 m
3. Perigee/apogee	27.55 days	14.5 m
4. 206-day cycle due to spring/neap and perigee/apogee cycles	206 days	15.5 m
5. Saros cycle (last peaked in 2012-2013)	18.03 years	16.0 m

One of these cycles is the spring-neap tidal cycle (Wolanski & Elliott, 2015). The spring-neap tidal cycle includes two spring tides (strong tides of increased tidal range) and two neap tides (weak tides of decreased tidal range) (Wolanski & Elliott, 2015; Pugh & Woodworth, 2014). Within this 28-day cycle, the spring and neap tides bring different volumes of water into an estuary (i.e., tidal prism) depending on the relative height of the tide (Hume, 2005). The tidal prism is the same during the ebb tide (excluding any contribution from freshwater inflows) as it is with the flood tide (Hume, 2005), however, the speed and duration at which the water goes in and out of an estuary is not always the same. This is called tidal asymmetry.

Tidal asymmetry is a result of friction, the shape of an estuary and the interaction between different tidal constituents (Dronkers, 1986; Guo et al., 2018; Pugh & Woodworth, 2014; Wolanski & Elliott, 2015; Kidd, 2016). In regard to tidal asymmetry, an estuary can either be flood dominant or ebb dominant. In general, a shorter rising tide than falling tide, stronger peak flood currents than ebb currents or a longer high-water slack tide than low water slack tide result in a flood-dominated estuary (Guo et al., 2018). The opposite is true for ebb-dominated estuaries (Guo et al., 2018).

The tidal currents that play a part in determining whether or not an estuary is flood dominant or ebb dominant are a large component of the hydrodynamics within an estuary. They are driven by the tides and influenced by bed morphology, but are also considered the dominant agent of sediment dynamics (Dalrymple et al., 2012).

1.5.4. Sediment Dynamics

Sediment dynamics within an estuary are crucial to understand when studying tidal wetlands, intertidal bedforms and other morphological characteristics of an estuary. They are also very complicated and influenced by multiple hydrodynamic and sedimentological factors (Wang, 2012). However, in order to understand what influences sediment dynamics, one must first understand the basics of sediment transport.

There are three phases of sediment transport: (1) initiation of motion (erosion), (2) transport and (3) deposition (Wang, 2012). Initiation of motion, or erosion, occurs when the fluid force exceeds frictional force and submerged gravitational force (Wang, 2012). Once sediment motion is initiated, transport of the sediment occurs, either along the bed or suspended in the above water column (Wang, 2012). The mode in which it is transported depends mainly on the size of the sediment or grain. In general, the smaller the grain size, the easier it is to erode and transport (Wang, 2012; Costa, 2016). The opposite can be said for larger grain sizes. Eventually, when the fluid force no longer exceeds the submerged gravitational force, the sediment will settle and deposit. There are multiple forces and factors that influence the movement of sediment within an estuary, with tidal currents being the dominant agent. Other forces and factors that will be discussed are river currents and suspended sediment concentrations.

Tidal currents are key for sediment transport. If tidal currents reach a particular velocity, they can erode sediment from its source and transport it throughout the estuary. For example, this may happen during a flood and/or ebb tide, when velocities are highest during the tidal cycle. If tidal currents decrease in velocity, it may result in sediment deposition and the inability to entrain sediment. This may happen during slack tide, for

example, when velocities are lowest during the tidal cycle. Tidal currents usually control sedimentation along the axis of an estuary because the tidal prism and resulting tidal currents become larger (Dalrymple, 2012). However, the further upstream one goes into an estuary, the more sediment transport will depend on the river currents as opposed to tidal currents.

River currents play an important role in sediment dynamics locally at certain times (Dalrymple, 2012). The most common modes of sediment transport in rivers are those of bedload (along the bed) and suspended load (in the above water column), which is similar to that of tidal currents (Wang, 2012; Garcia, 2008). What is unique about sediment transport by river currents is that it varies at different times of the year. For example, during the spring when snow is melting, river currents tend to be stronger with higher river discharge. This can cause flushing of sediment further downstream. During the summer, however, higher temperatures and less precipitation decrease water levels and result in weaker river currents with lower river discharge. At this time of year, decreasing freshwater influence allows buildup of sediment. This seasonal dynamic can lead to seasonal changes in bed level (Crewe, 2004). Therefore, river currents can play a critical role in where sediment is eroded, transported and deposited.

The concentration of suspended sediment within the water column has an affect on sediment dynamics as well. Particularly in a broad zone known as the turbidity maximum, which contains abnormally high suspended sediment concentrations (Wells, 1995; Dalrymple et al., 2012; Wang, 2012). The sediment in this zone also tends to be fine-grain sediment, such as clays and silts (Wang, 2012; Doxaran et al., 2009). This zone is the result of flocculation and density-driven water-circulation patterns, but is very

complex and unpredictable (Doxaran et al., 2009; Dalrymple & Choi, 2007). However, a study done by Doxaran et al. (2009) concluded that the dynamics of the turbidity maximum zone in macrotidal estuaries plays an important role in the transfer of suspended sediment and other particulates from the continent to the ocean due to the seasonal migration of the turbidity maximum zone. Because the nature of the turbidity maximum zone is to have abnormally high concentrations, it is common for these zones to exhibit a layer of fluid mud along the bed (Wang, 2010). Fluid mud is a highly concentrated suspension of fine-grained cohesive sediment that is said to be characterized as 10 g/L or greater in concentration (Wang, 2010; Faas, 1991). Unfortunately, the characteristics of fluid mud are not well known (Dalrymple & Choi, 2007). Lastly, the turbidity maximum zone is likely to be similar in location within an estuary to the bedload convergence zone (Dalrymple & Choi, 2007; Dalrymple et al., 2012).

1.5.6. Response of an Estuary to Physical Alterations

Estuaries are naturally shaped by their hydrodynamics and sediment dynamics; however, they can also be altered by human activities. These activities include the dredging (removal) of sediments, the construction of flood management infrastructure (i.e., dykes or dams), the construction of tidal barriers (i.e., causeways) or the restoration of the floodplain. This action of altering an estuary can also be conceptualized as removing an estuary from its state of equilibrium. What happens to an estuary in disequilibrium, such as through managed realignment, and how does it adjust?

Dredging, for example, is a common practice and one way to remove an estuary from its state of equilibrium (Kidd, 2016). It is the removal of sediment from the bed of

an estuary. The sediment is then either placed elsewhere in the estuary or removed from it entirely (Kidd, 2016). This does a number of things to an estuary. First and foremost, it increases the volume of water the estuary can hold (Nichols, 1988), meaning it increases the tidal prism. It also increases water depth, and therefore, increases currents (Nichols, 1988). The way that an estuary adjusts to dredging is to regain equilibrium by accretion of more sediment (Kidd, 2016). However, even more common than dredging in this day and age is opening up floodplains by breaching coastal barriers such as dykes.

Opening up a floodplain in an estuary is different than dredging, in that it adds more space horizontally for tidal water to go instead of just digging deeper into the existing estuary channels. According to Kidd (2016), there have been studies in New Brunswick and South Australia that illustrated a decrease in tidal prism by adding a barrage within each respective estuary. If one does the opposite, removing a barrage or some sort of barrier, the estuary will adjust by increasing its tidal prism because opening up more accommodation space for water will result in more water coming into the estuary (Kidd, 2016). In terms of how water levels change, introducing a managed realignment site with breaches has the potential to raise water levels throughout the estuary because newly created intertidal areas draw in additional water into the estuary (Pontee, 2015; French, 2006). This finding was for the Parret Estuary in the UK, which is located near the mouth of the estuary, and was simulated using a hydrodynamic model (Pontee, 2015). Townend and Pethick (2002) did similar modelling for the Humber Estuary in the UK and found that managed realignment sites in the outer estuary tend to increase water levels in the estuary and rivers and managed realignment sites in the inner estuary tend to decrease water levels. However, a study by Bennett et al. (2020) found

that managed realignment sites did not change water levels in the estuary, except for an increase in water levels within the managed realignment site. Overall, these studies suggest that changes in water level depend on the location of the managed realignment site in the estuary.

1.6. Hydrodynamic Models

In addition to observing the processes that influence tidal wetlands, modelling of these processes can be done to increase one's understanding of the system. For instance, modelling the hydrodynamics in a floodplain after implementing managed realignment can provide insight into tidal wetland restoration. On a larger scale, modelling can also provide insight into how sediment delivery and hydrodynamics are influenced by changes in an estuary.

There are two types of models: physical models and numerical models (Hughes, 1993). As defined by Hughes (1993), a physical model is a representation of a physical system, usually at a reduced size, for which the major dominant forces acting on the system are applied and are represented in the model in correct proportion to the actual physical system. A numerical model is a mathematical representation of a physical system, in which the equations are discretized and solved using a computer (Hughes, 1993). For this thesis research, a numerical hydrodynamic model was used, and thus, will be the focus going forward.

A hydrodynamic model is a type of model that describes the flow of water in different environments, such as a tidal wetland (Seenath et al., 2016). A numerical hydrodynamic model can be one of three different spatial dimensions: one-dimensional

(1D), two-dimensional (2D), and three-dimensional (3D). One-dimensional models are the simplest of the three and are best suited for describing flows within interconnected channel networks (Moffatt & Nichol, 2005). These models are fast, require a small amount of field data to set up, and can describe control structures better than higher-dimensional models (Moffatt & Nichol, 2005). However, they are unable to describe two-dimensional characteristics, such as channel meander, circulation with larger water bodies, and stratification (Moffatt & Nichol, 2005). Two-dimensional models can describe complicated circulation patterns within larger bodies of water, such as estuaries, but they are more time-consuming to set up and run, require much more field data, and can run into problems with numerical stability when simulating environments that have rapid wetting and drying cycles (e.g., tidal wetlands) (Moffatt & Nichol, 2005). Three-dimensional models can compute all the same physical processes that a two-dimensional model can, except they can also model through a number of vertical layers to describe the vertical structure of the water column (Moffatt & Nichol, 2005). These models provide the most detailed look at a hydrodynamic system, but they require a substantial amount of field data and take much longer to compute (Moffatt & Nichol, 2005).

For a numerical hydrodynamic model to run properly and produce accurate results, it must solve a collection of equations that describe the motion of fluids, transport of sediment, salinity, and other critical constituents that occur in real systems (Moffatt & Nichol, 2005). These governing equations are usually the partial differential Navier-Stokes equations of motion, which are based on the principles of conservation of momentum and mass (Moffatt & Nichol, 2005; Seenath et al., 2016). The two key equations solved in a hydrodynamic model simulation are the horizontal momentum

equation and the depth-averaged continuity equation (Lesser et al., 2004). The 3D equations are described in detail in Lesser et al. (2004) and the 2D equations (1a, 1b and 2) are briefly summarized in Appendix A. Within a model, these equations are solved for each cell within a grid, and based on the grid structure, it can fall into one of two categories: structured or unstructured grid models (Seenath et al., 2016). Structured grids are usually based on quadrilateral grid cells and compute flow using a finite difference approach, whereas unstructured grids are composed of triangular elements and compute flow through a finite element or finite volume method (Seenath et al., 2016). Unstructured grid models have greater grid flexibility, but structured grid models are computationally simpler (Seenath et al., 2016).

What is unique about hydrodynamic models is that they are able to simulate water flow and transport over time. Unlike modelling through a computerized system like GIS, which can provide similar hydrodynamic information (e.g., water levels and final location of water after transport), hydrodynamic models can simulate how the water gets to its final location and how long it takes to get there (Seenath et al., 2016). This is a significant benefit to hydrodynamic models. Another benefit of hydrodynamic models is that the user is able to control what is integrated within the model in terms of parameters and modules. For example, a vegetation module can be integrated into a hydrodynamic model, which is critical in order to simulate more accurate flow velocities in areas where vegetation exists, as demonstrated by Ashall et al. (2016) and Hu et al. (2018). Figure 1.6 shows how adding a vegetation module affects flow velocities.

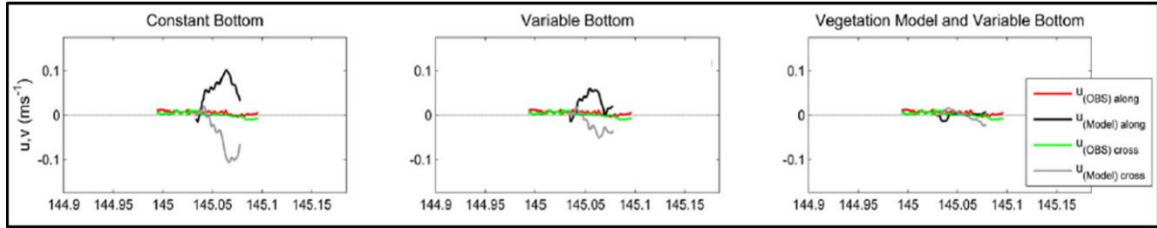


Figure 1.6. Observed (measured) flow velocities (red and green) compared with modelled velocities (black and grey) for different bottom roughness scenarios in Delft3D (modified from Ashall et al., 2016).

It is clear that adding a vegetation module results in a better match between observed velocities and modelled velocities. Figure 1.6 also illustrates the importance of using realistic, varying bottom roughness throughout the model domain.

Chapter 2 – Study Area

2.1. Geographical Setting

This research took place in the Salmon River Estuary in the Cobequid Bay, which is located in the upper Bay of Fundy, Nova Scotia, Canada (Figure 2.1). The Bay of Fundy is located on the east coast of Canada and forms the northeast extension of the Gulf of Maine (Davidson-Arnott et al., 2002). It is a macrotidal environment with the highest tides in the world, measuring up to 17 meters at Burntcoat Head in the upper Bay of Fundy (Desplanque & Mossman, 2004; Todd et al., 2014). There are two reasons as to why the tides in this region of the world are so high: (1) the Bay of Fundy is funnel-shaped, causing water levels to be higher in the narrowest and shallowest parts of the Bay of Fundy (e.g., the upper region), and (2) the natural period of oscillation of the Bay of Fundy is very close to the M_2 lunar semidiurnal tidal period, creating a near-resonant condition (Desplanque & Mossman, 2004; Ashall et al., 2016; Garrett, 1972). The tides here are semi-diurnal and are dominated by the tidal constituent M_2 , with a period of 12.42 hours, with significant contributions from the S_2 constituent (12 hours), the N_2 constituent (12.66 hours) and the diurnal tides (Garrett, 1972).

In terms of sediment in the upper Bay of Fundy, the four principal sources are eroding cliffs (major contributor), rivers, the sea bed and the open sea (Amos, 1977). The lower portions of the Bay of Fundy are characterized by the presence of sandy material, while in the upper Bay of Fundy there are considerable accumulations of fine sediments (Davidson-Arnott et al., 2002).

One feature of this region, in the larger of the rivers leading into the upper Bay of Fundy, are the tidal bores. A tidal bore is the leading edge of a flood tide (incoming tide)

that manifests itself as a wave going against the flow of the river it occurs in (Lynch, 1982). Ideal conditions for tidal bores include a high tidal range, a shallow river and a slight channel gradient (Desplanque & Mossman, 2004). The Salmon River, which flows into the Bay of Fundy through the Salmon River Estuary, possesses these conditions (Figure 1.5).

The study area covers a much smaller area and is where field measurements were collected. The managed realignment and tidal wetland restoration site is known as the Onslow-North River marsh and is located on the north side of the Salmon River and North River confluence (Figure 2.1).



Figure 2.1. The study area and restoration site in the inner Salmon River Estuary. The inset shows a satellite image of the Bay of Fundy and the relative location of the study area. The satellite image was taken by Joshua Stevens at the NASA Earth Observatory (2019).

2.2. History of the Study Area

According to Shaw et al. (2010), the majority of tidal wetlands in the Bay of Fundy were dyked beginning in the late 1600s and still remain today. The purpose of dyking was to convert tidal wetland habitat into what is now referred to as dykelands or marshlands, which were, and in most cases still are, used for agricultural purposes. This practice, along with the construction of transportation infrastructure and related development activities, has resulted in the loss of approximately 85% of tidal wetlands in the Bay of Fundy (Hanson and Calkins, 1996). As with much of the Bay of Fundy, the Salmon River Estuary is also heavily dyked. This, however, is one factor out of many that play a role in the local area's historical and current issue with flooding.

Truro is a small regional centre located on the floodplain of the Salmon River with a dyke network that was originally constructed to protect agricultural land, and now also protects residential, commercial and transportation infrastructure (Rahman et al., 2019). At certain locations along the dykes there are aboiteaux that allow freshwater to drain into the Salmon River at low tide but prevent tidal waters from entering the land behind the dykes. Although the dykes and aboiteaux are there to protect infrastructure and agricultural land, they are a contributing factor to the flooding in Truro when the right set of conditions occur. Conditions include extreme rainfall, high or spring tides, aboiteaux blocked by sediment buildup, large ice blocks and storm surges (CBCL Limited, 2017).

Truro's flooding history is extensive, with the first documented flood occurring in 1792 and flood studies conducted in 1971, 1983, 1988, 1997 and 2006, each inspired by major flood events (CBCL Limited, 2017; Rahman et al., 2019). The most recent flood

study was published in 2017 by CBCL Limited, which identified and described in detail the complex interactions of factors that cause flooding, involved comprehensive modelling in order to better understand these complex flooding processes and provided recommendations for short term and long term solutions to flooding in Truro. The recommendations from this study led to the inception of the managed realignment project at the Onslow-North River restoration site.

The ecomorphodynamics of the Salmon River Estuary and the Salmon River itself are quite understudied. However, the studies that do exist provide information on the system as a whole and details on some of the morphological features of the Salmon River Estuary, from large scale features like the shape of the estuary and sand bar formations, to small scale features like grain size distribution throughout the estuary (Dalrymple et al., 1990; Dalrymple et al., 1992; Dalrymple, 2006; Dalrymple and Choi, 2007; Dalrymple et al., 2012). For example, the Salmon River Estuary is progradational, with sediment primarily derived from areas seaward of the estuary, and is flanked by mudflats and tidal wetlands in the inner half of the funnel-shaped estuary (Dalrymple et al., 1990). Additionally, Dalrymple and Choi (2007) state that the Salmon River Estuary is flood dominant, with ebb dominance occurring only in the uppermost reaches of the estuary where ebb currents are supplemented by river flow. Another study, carried out by Crewe (2004), characterizes sediment in the Salmon River Estuary. He found that suspended sediment concentrations in the upper estuary were highly variable with values exceeding 20 g/L, well above the threshold that defines fluid mud (Wang, 2010; Faas, 1991), for more than 80% of the samples collected annually. Crewe (2004) also found that sediment deposits in the river channels in the upper estuary can build up to a point where they

restrict river discharge and can cause winter ice jams, which sometimes result in flooding. Crewe's research focused on the same sections of the Salmon River and North River as this research (see Figure 2.1). Additionally, van Proosdij et al. (2018) and Matheson (2020) studied the rates of erosion and progradation of foreshore tidal wetlands in the Salmon River Estuary, finding that foreshore tidal wetlands in the outer estuary are most sensitive to dyke realignment while those located in the inner estuary are most responsive to dredging activities. With a better understanding of the morphodynamics specific to the managed realignment site, and the potential for reducing Truro's flood risk by restoring 92 hectares of floodplain, gaps in the existing literature for this region will be filled. In addition, the current research contributes by being the first to measure and model the hydrodynamics in the inner Salmon River Estuary.

2.3. Managed Realignment Design

The development of a managed realignment project should be an interactive process, incorporating stakeholder and rights holder engagement in the design process, leading to implementation and followed by monitoring, as previously illustrated in Figure 1.1. It should also include the use of a hydrodynamic model to inform and support the managed realignment design. The design selected for the managed realignment project in Truro is shown in Figure 2.2 and was created based on preliminary modelling of hydrodynamic conditions near the restoration site.

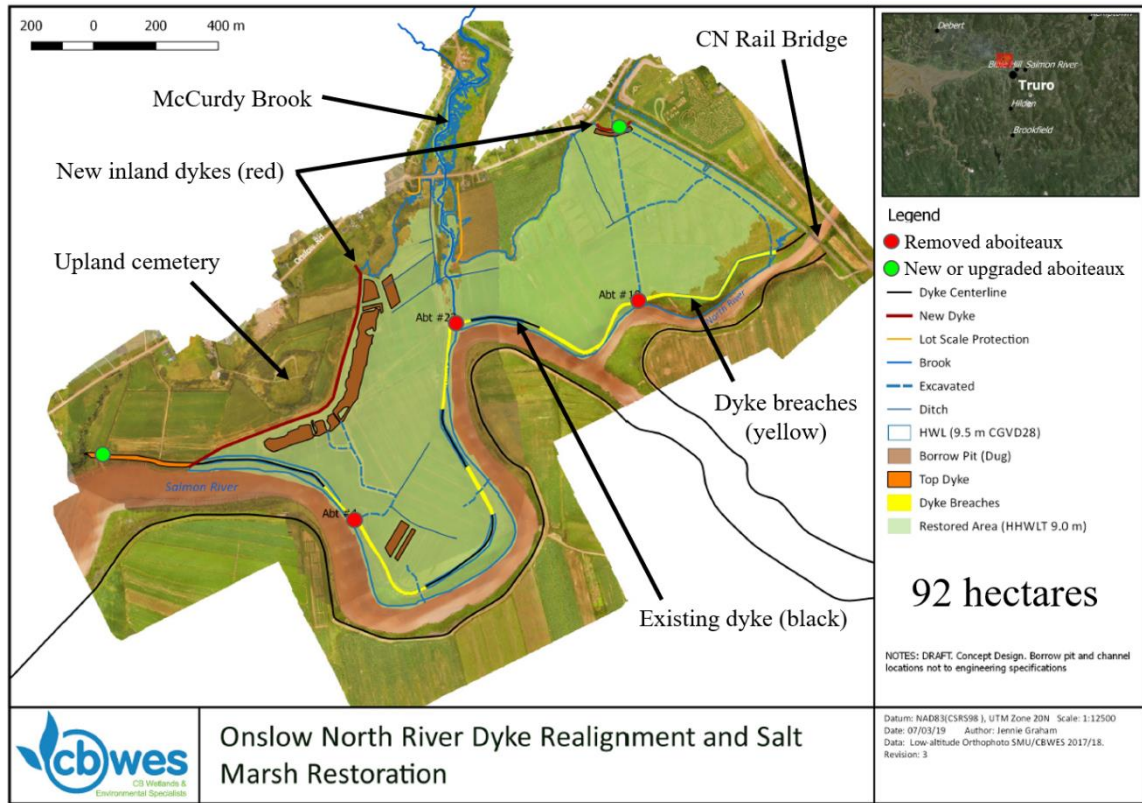


Figure 2.2. The final managed realignment design for the Onslow-North River restoration site along the Salmon River and North River in Truro (used with permission from CBWES).

The final design included the construction of two new sections of dyke, two new aboiteaux (one of which is not included in Figure 2.2), topping approximately 500 m of existing dyke, upgrading one aboiteau, excavation of tidal channels within the restoration site, decommissioning 3 km of dyke by strategically excavating four breaches and the removal of three aboiteaux. At the time of this thesis, managed realignment had not yet been implemented as the construction of the inner dykes and the removal of aboiteaux were in progress. At this time as well, dykes had not been breached, which is the last step of construction for a managed realignment project. Once the existing dyke infrastructure is breached, monitoring of the site will occur.

Chapter 3 – Methods

3.1. Experimental Design

This research was divided into two parts: (1) field data collection and analysis, and (2) hydrodynamic modelling. Field data was collected for two reasons. One reason was to help characterize the Salmon River in terms of its hydrodynamics, which is currently understudied. This included measuring velocities, water depths and suspended sediment concentrations, surveying the river bed elevations (bathymetry) for the digital elevation model (DEM) and making general observations at different locations along the river near the restoration site. Additionally, georeferenced low-altitude aerial photographs were obtained of the study area using a remotely piloted aircraft (RPA) in order to produce a high resolution orthomosaic and digital surface model (elevation). The second reason was to calibrate and validate model results.

The hydrodynamic modelling portion of this thesis had multiple objectives. One was to calibrate and validate the model results with the measured data collected in the field to determine how well the model was able to reproduce the field measurements. The second objective was to investigate the response of the model to changes in two model parameters: bathymetry (the DEM) and bottom roughness (the bottom friction coefficient). The third objective was to determine the maximum flood extent and flow velocities, as water flooded the restoration site, using a DEM that incorporated the managed realignment design.

This research integrated both field data and hydrodynamic modelling. This combination is key because it can increase confidence in the performance of the model.

3.2. Field Data Collection

3.2.1. Hydrodynamics

Hydrodynamic data were collected from August 12 to August 14, 2018 in the Salmon River and North River in Truro. During this time period, measurements were taken over four spring tides. The tides, their predicted high tide times (in Atlantic Daylight Time (ADT) and Greenwich Mean Time (GMT)) and their predicted tidal ranges (in Chart Datum (CD)) at Burntcoat Head are summarized in Table 3.1.

Table 3.1. *The four measured and modelled tides, their predicted high tide times (in ADT and GMT) and their predicted tidal ranges (in CD) at Burntcoat Head. The information in this table was acquired from Fisheries and Oceans Canada (2018).*

Tide Number	Date	High Tide Time (ADT)	High Tide Time (GMT)	Tidal Range in CD (m)
Tide 1	August 12, 2018	14:23 (2:23 pm)	17:23 (5:23 pm)	14.9
Tide 2	August 13, 2018	02:46 (2:46 am)	05:46 (5:46 am)	15.4
Tide 3	August 13, 2018	15:12 (3:12 pm)	18:12 (6:12 pm)	15.1
Tide 4	August 14, 2018	03:34 (3:34 am)	06:34 (6:34 am)	15.3

High tide in the study area occurred, on average, 19 minutes after the predicted time at Burntcoat Head (approximately 40 km west of the study area). The times of high tide are provided in GMT in addition to local time zone ADT because the Delft3D model references the GMT time zone.

Four different types of instruments were deployed in the Salmon River and North River to collect data over the four spring tides. Two Nortek Acoustic Doppler Velocimeters (ADV) were deployed at two locations within the study area (Figure 3.1). The two ADVs measured 3D velocity at a sample point located approximately 15 cm

above the bed and water depth via a pressure sensor located approximately 55 cm above the bed. The ADVs were programmed using Nortek's Vector software to sample at 16 Hz with a burst interval of 600 seconds (10 minutes) and 4800 samples per burst. Each sampling burst was 5 minutes long with a subsequent rest burst of 5 minutes. Two Campbell Scientific Optical Backscattering Sensors (OBSs) were deployed with the two ADVs, sampling simultaneously at the same sample point 15 cm above the bed. This instrument measures particle backscatter which can later be processed and converted to suspended sediment concentrations. Deployment settings for the two ADVs and OBSs are found in Appendix C.

Two Nortek Acoustic Doppler Current Profilers (ADCPs) were also deployed at two locations within the study area (Figure 3.1). This instrument measures velocity in pre-determined intervals throughout the water column, particle backscatter and water depth among other variables. The ADCPs were programmed using Nortek's AquaPro software. ADCP 1 is an Aquadopp Profiler 2 MHz and was programmed to operate continuously at a frequency of 2 MHz (the maximum frequency for ADCP 1) with a sampling rate of 10 seconds, a cell size of 0.2 m with 20 cells and a blanking distance of 0.2 m. ADCP 2 is an Aquadopp Profiler 1 MHz and was programmed to operate continuously at a frequency of 1 MHz (the maximum frequency for ADCP 2) with a sampling rate of 10 seconds, a cell size of 0.5 m with 10 cells and a blanking distance of 0.4 m. The transducer heads of ADCP 1 and ADCP 2 were positioned approximately 10 cm and 5 cm above the bed, respectively.

Lastly, two Teledyne ISCO water samplers were deployed within the study area (Figure 3.1). This instrument draws in water (including suspended sediment) through a

tube at set time intervals and fills a series of 24 bottles within its canister. After collection, the bottles were taken back to the lab to be measured, filtered, dried and weighed in order to calculate the suspended sediment concentration per bottle. For both ISCOs, the nozzle was positioned 5 cm above the bed, the pump suctioned approximately 250 mL of water per bottle and the samples were collected at 10-minute intervals. Figure 3.1 illustrates the locations of all the instruments throughout the study area.

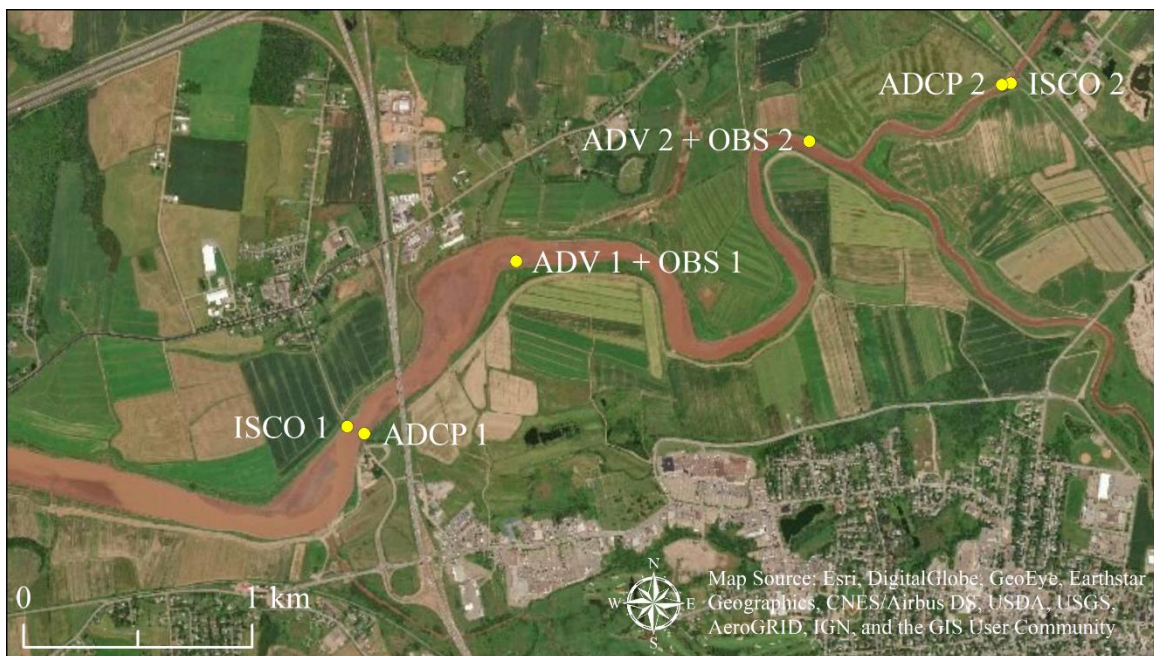


Figure 3.1. Locations of hydrodynamic instruments and water samplers in the Salmon River and North River.

The surveyed locations (in UTM coordinates) and elevations (in CGVD28) of the instruments' sampling volumes (ADV/OBSs) or transducer heads and nozzles (ADCPs and ISCOs) are provided in Table 3.2. Elevations of the pressure sensors on the ADVs are provided as well. The pressure sensors on the two ADCPs are at the same elevations as the instruments' transducer heads.

Table 3.2. Instruments and their surveyed locations (in UTM coordinates) and surveyed elevations (in CGVD28). The ADVs/OBSs were surveyed at the sample point and the pressure sensor of the two ADVs. The ADCPs and ISCOs were surveyed at the transducer head and the bottom of the nozzle, respectively.

Instrument(s)	Surveyed Location (m)	Surveyed Elevation (m)	
ADV 1 + OBS 1	(x,y) = (475429.589, 5025115.292)	Sample point	7.455
		Pressure sensor	7.822
ADV 2 + OBS 2	(x,y) = (476712.308, 5025640.776)	Sample point	7.047
		Pressure sensor	7.414
ADCP 1	(x,y) = (474765.378, 5024359.021)	6.537	
ADCP 2	(x,y) = (477555.502, 5025887.447)	8.173	
ISCO 1	(x,y) = (474690.840, 5024389.521)	5.321	
ISCO 2	(x,y) = (477595.286, 5025895.089)	7.839	

The ADVs/OBSs, ADCPs and ISCOs were programmed and deployed on the morning of August 12, 2018, well before Tide 1 was scheduled to arrive in the early afternoon. Figure 3.2 shows all instruments after deployment.

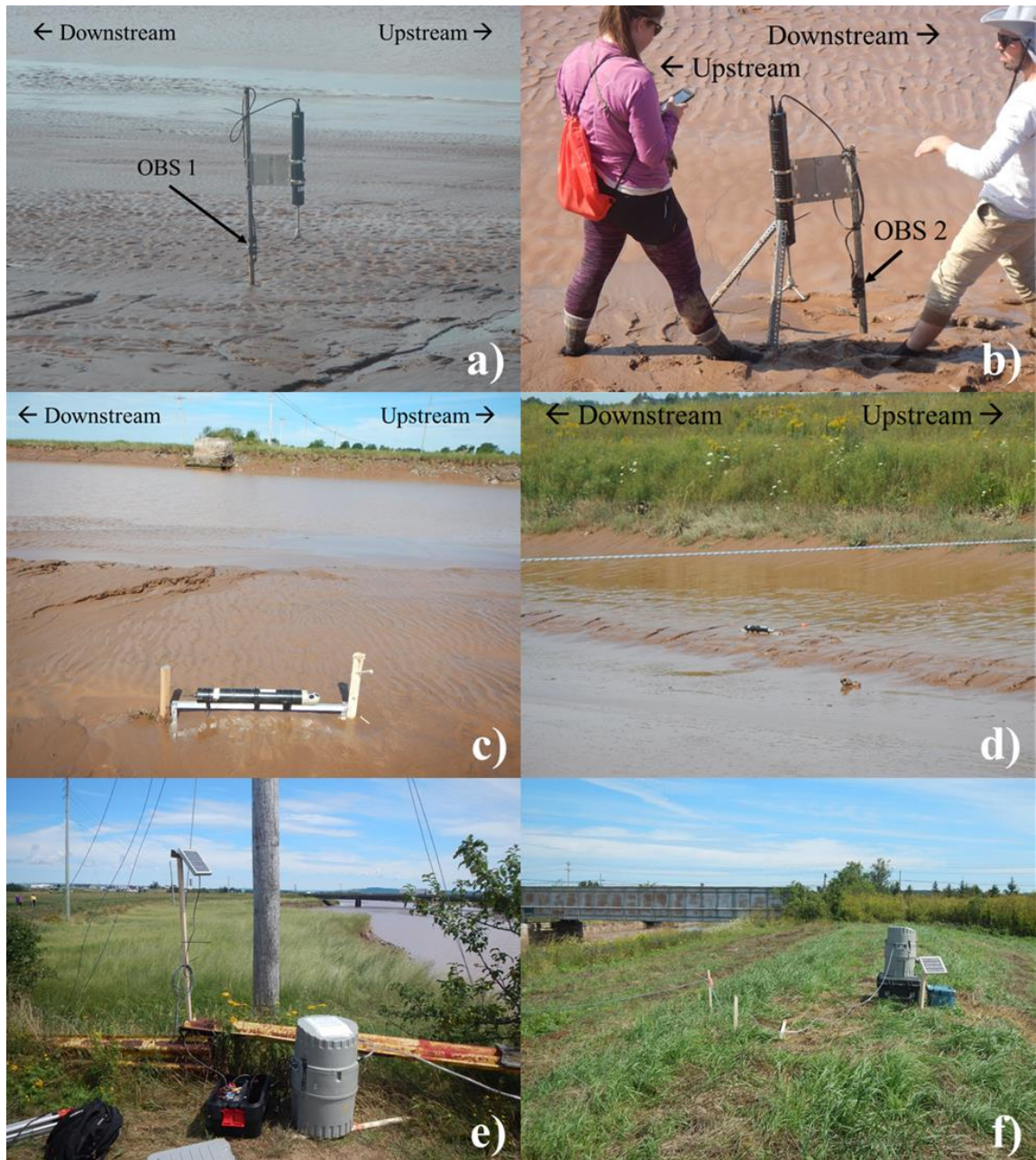


Figure 3.2. (a) ADV 1 + OBS 1 deployed on the south side of the Salmon River at low tide. (b) ADV 2 + OBS 2 deployed on the north side of the Salmon River at low tide. The instrument had to be braced and secured to handle the high currents at this location. (c) ADCP 1 deployed on the south side of the Salmon River near the Highway 102 Bridge at low tide. (d) ADCP 2 deployed on the north side of the North River near the CN Rail Bridge at low tide. (e) ISCO 1 setup on the north side of the Salmon River. The camera was facing upstream towards the Highway 102 Bridge. (f) ISCO 2 setup on the south side of the North River. The camera was facing upstream towards the CN Rail Bridge.

The positive x-axis of the two ADVs were pointed upstream so that flood tide velocities were positive and ebb tide velocities were negative. The ADVs collected data for all four tides and were retrieved after the fourth tide. A sample of the ADV files can be viewed in Appendix D. The processing was done using a script written in MATLAB[®] (Appendix E). The script read the data from each of the eight files (one at a time) and was able to calculate and plot multiple variables, such as water depth, u-, v- and w-components of velocity, resolved horizontal velocity, magnitude of velocity, suspended sediment concentration (from the OBS data), turbulent kinetic energy, shear stress and shear velocity. Suspended sediment concentrations were calculated by applying a calibration equation to the raw signal data (column 16 in Appendix D) measured by OBS 1. All variables were averaged over each 5-minute sampling burst and plotted at 10-minute intervals (accounting for the 5-minute rest period after each sampling burst) over the span of each tide.

Both ADCPs were positioned with the positive x-axis pointed upstream, collected data for all four tides and were retrieved after the fourth tide. Deployment settings for both ADCPs can be found in Appendix C. The ADCP data were processed and plotted using Nortek's Storm software.

Both ISCO 1 and ISCO 2 were programmed using the same settings (Appendix C). Once the 24 bottles in the water sampler units were filled over the course of each tide, they were removed, water volumes in each bottle were measured and recorded before transferring into Nalgene bottles and then all bottles were labelled and subsequently stored in a cooler with ice. When transferring the samples into Nalgene bottles, purified water was used to rinse the remaining sediment from the inside of the 24 ISCO bottles.

This changed the water volume of the sample, diluting the concentration of sediment, therefore, new water volumes were recorded. Afterwards, the ISCO was filled with the same 24 empty bottles and programmed again for the next tide. This process was repeated for all four tides. In total, there were 192 samples (from both ISCOs) to process. After mixing the samples well, subsamples from the Nalgene bottles were filtered via suction filtration onto individual pieces of filter paper and left in petri dishes to air dry for several days (Chen et al., 1992). Subsample volumes were measured and recorded. After air drying, the samples were placed in a sealed desiccator for a minimum of one hour to remove the remaining moisture from the sediment. The samples were removed from the petri dishes and individually weighed, in grams. The following equation was used to calculate the weight of the sediment only, where W_{FS} is the weight of the filter with the dried sediment, W_F is the weight of the filter paper with no dried sediment and W_S is the weight of just the dried sediment.

$$W_{FS} - W_F = W_S \quad (3)$$

To obtain the concentration of sediment in each sample, the weight of the sediment, W_S , was divided by the subsample water volume. However, the subsamples processed through suction filtration were diluted, therefore, the dilution formula was applied to calculate the suspended sediment concentrations in the non-diluted samples. Below is the dilution formula, where C_1 is the concentration of sediment in the non-diluted samples, C_2 is the concentration of sediment in the diluted samples, V_1 is the volume of water in the non-

diluted samples, V_2 is the volume of water in the diluted samples and V_{SUB} is the volume of water in the subsample.

$$C_1 V_1 = C_2 V_2 \quad (4)$$

$$C_1 = C_2 V_2 / V_1 \quad (5)$$

$$C_2 = W_S / V_{SUB} \quad (6)$$

This formula was applied to all 192 samples and resulted in suspended sediment concentrations, in g/L. The data were then entered and plotted in Microsoft Excel.

3.2.2. *Surveying*

Ground and river bed elevation surveys were conducted to make an updated DEM for the hydrodynamic model. Two types of surveys were conducted by the In_CoaST lab and the Maritime Provinces Spatial Analysis Research Centre (MP_SpARC) at Saint Mary's University: (1) bathymetric surveys of the Salmon River and North River at high tide, and (2) RPA surface elevation surveys of the exposed mudflats in both rivers at low tide.

In the summer of 2018, the In_CoaST team conducted the bathymetric surveys using a SonTek M9 HydroSurveyorTM that was mounted on a SonTek HydroBoard and towed behind a kayak (Figure 3.3).



Figure 3.3. The HydroSurveyor™ mounted on the HydroBoard being towed by a kayak in the Salmon River.

On top of the HydroSurveyor™ was an RTK GPS antenna that received positional data by communicating with satellites and a base station that was situated on a nearby dyke (Figure 3.4).

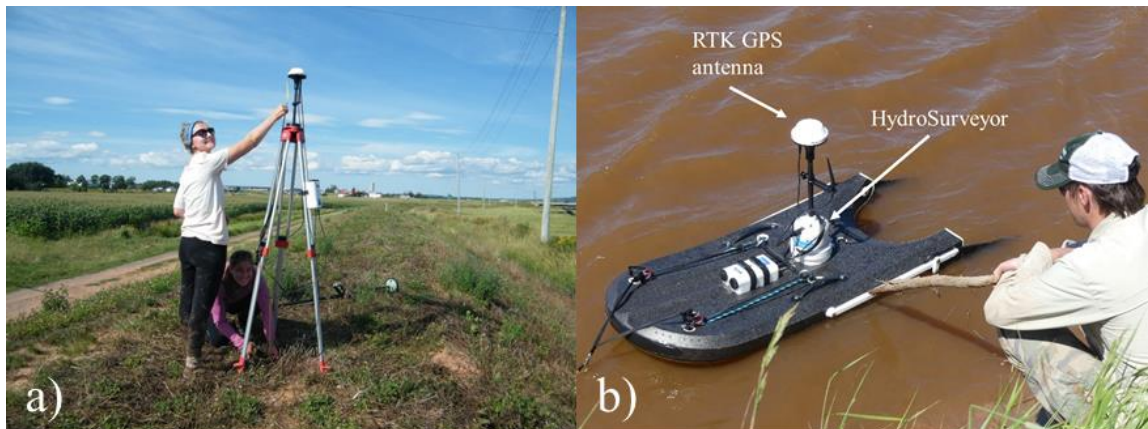


Figure 3.4. (a) Adjusting the tripod of the base station positioned on top of a dyke. This photo was taken on August 12, 2018. (b) A closer view of the HydroSurveyor™ mounted on the HydroBoard. This photo was taken on June 27, 2018.

The HydroSurveyor™ unit itself has nine beams, but only five beams are active at a time (SonTek, 2012a; SonTek, 2012b). The centre beam provides direct measurements below the instrument, similar to a single beam echosounder, and is always active when sampling. The other eight beams surround the centre beam and are projected at a 25-degree angle from the vertical axis. Only four of these beams are active at once, depending on water depth. The beams will automatically switch from one set of four beams to the other set of four beams once the water depth reaches a certain threshold (SonTek, 2012a; SonTek, 2012b). The HydroSurveyor™ has a depth accuracy of 0.02 m and a horizontal accuracy of < 1.0 m (SonTek, 2012b).

Once the HydroSurveyor™ was mounted on the HydroBoard, the base station was set up, a successful connection was made between the two and a compass calibration was performed on the instrument, the surveying began using a program called HYPACK®. HYPACK® is integrated with the HydroSurveyor™ unit and allows one to view depth data in real time as the instrument is surveying. In order to cover as much area as possible, surveying was done by paddling the kayak back and forth along the width of the river while being pushed along the river by the incoming and outgoing tides. Figure 3.5 illustrates the path taken by the kayak along the Salmon River and North River for all three survey days.

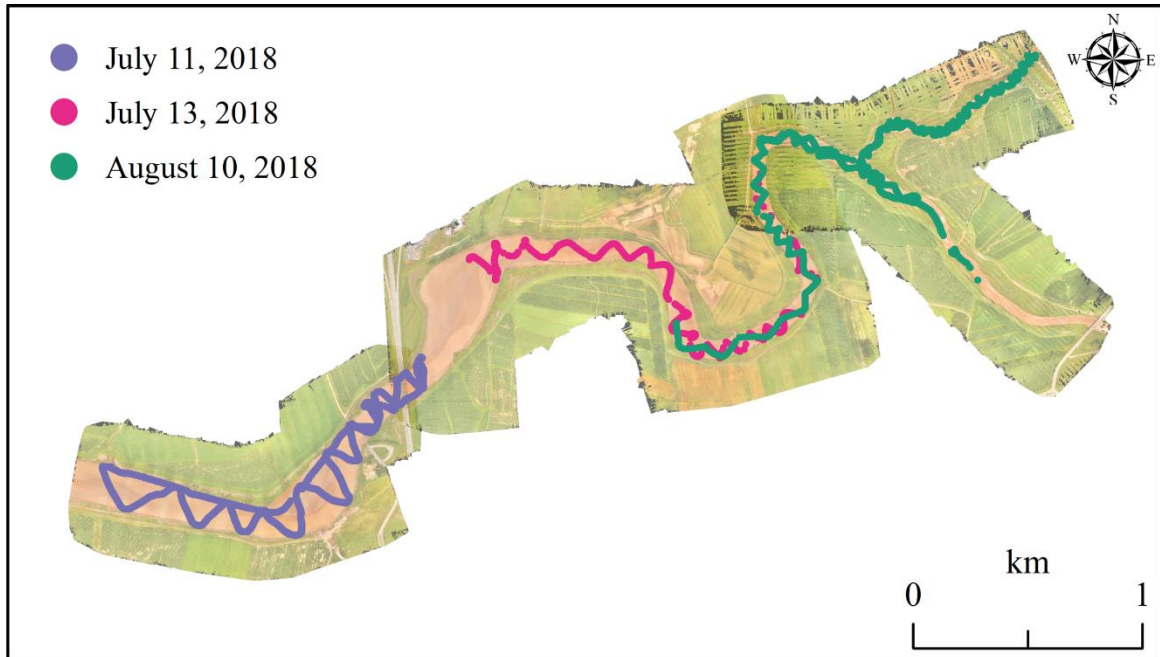


Figure 3.5. *HydroSurveyor™ sampling paths for all three data collection days.*

After the surveys were completed, the depth values were converted to elevation (in CGVD2013) using HYPACK®'s processing tool and then exported as a text file.

CGVD28 was selected as the vertical datum for all datasets to be consistent with previous modelling efforts and surveys, therefore, the HydroSurveyor™ data was converted from CGVD2013 to CGVD28 using an online tool called GPS-H found on the Natural Resources Canada website. Lastly, the data were opened in ArcMap™ to create the 2018 DEM.

The second round of surveying involved using a DJI Phantom® RPA over the course of three days. The RPA was flown at 90 m above ground level with an average vertical accuracy of 3.4 cm. The purpose of these flights was to survey the elevation of mudflats at low tide. Before going out into the field to survey, a flight plan was designed and ground control point (GCP) locations were selected. Once in the field, GCPs were

installed and surveyed using an RTK GPS, followed by the RPA surveys. Figure 3.6 illustrates the location of GCPs, the flight grids and the three areas that were surveyed.

August 14 is Day 1, August 16 is Day 2 and August 17 is Day 3.



Figure 3.6. Grids flown by an RPA (DJI Phantom[®]) to capture ground elevation of mudflats at low tide. Grids were flown over a span of three days (August 14, August 16 and August 17, 2018). GCPs are numbered and symbolized as red triangles. The red boxes represent each flight grid. Map created by Greg Baker and Reyhan Akyol, MP_SpARC, Saint Mary's University, 2018.

Once the RPA surveys were completed, the imagery and elevation data from each individual flight grid were opened in ArcMap[™] to create the 2018 DEM.

Figure 3.7 summarizes the steps taken to create the full 2018 DEM. It is important to note that this 2018 DEM was named according to the updated 2018 river bathymetry and mudflat elevations. Everything else, from the edge of the foreshore marsh to the outer

boundaries of the full DEM, represents surface elevations from a LiDAR survey conducted in 2013.

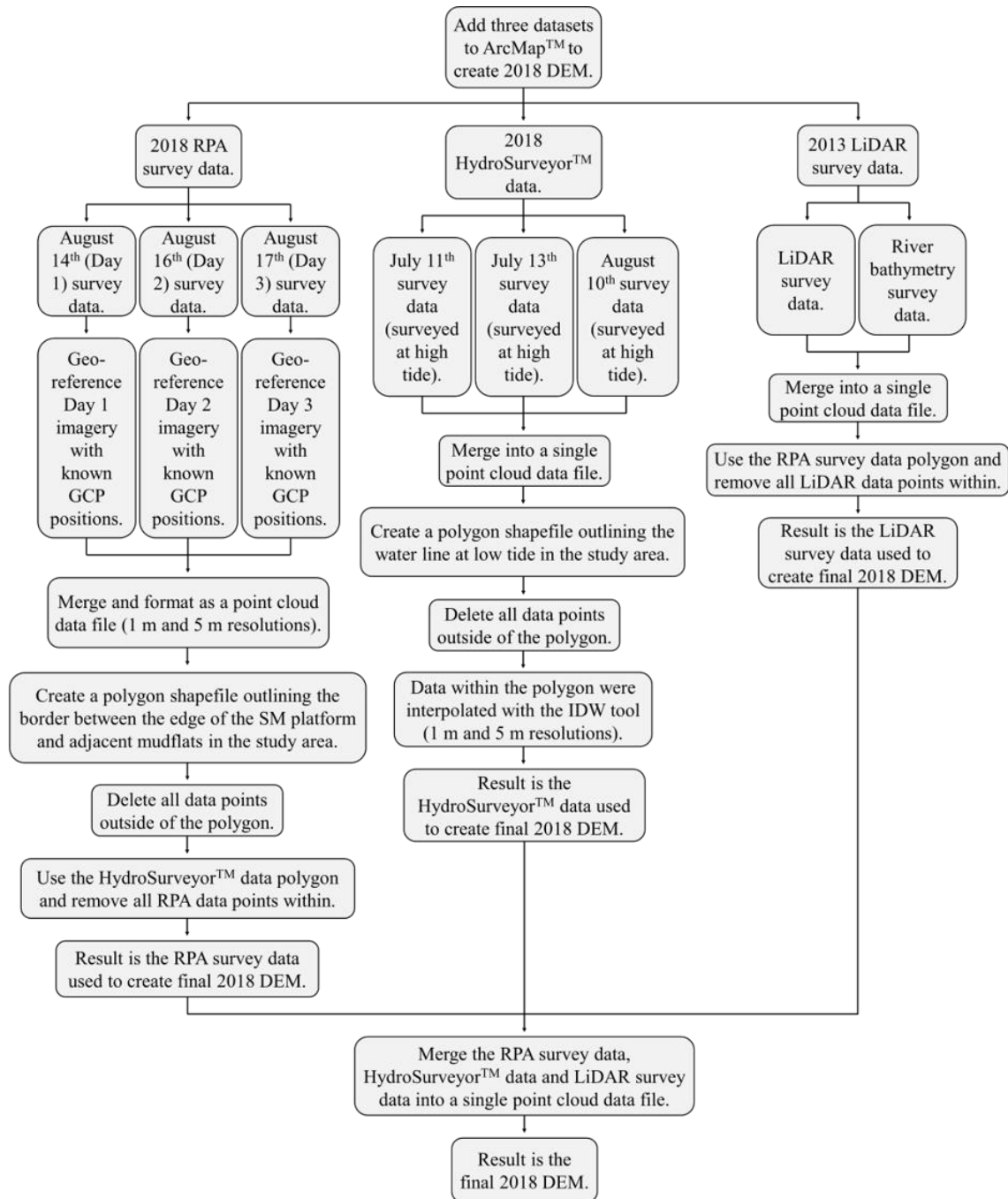


Figure 3.7. Flow diagram illustrating the steps taken to create the 2018 DEM in ArcMap™. SM is short for tidal wetland and IDW is short for inverse distance weighted.

Figure 3.8 illustrates the different survey methods used and the spatial resolutions of the study area for the 2018 DEM. Not shown is the rest of the 2018 DEM, which covers a much larger area of the Salmon River Estuary and consists of the 2013 LiDAR data at a spatial resolution of 5 m.

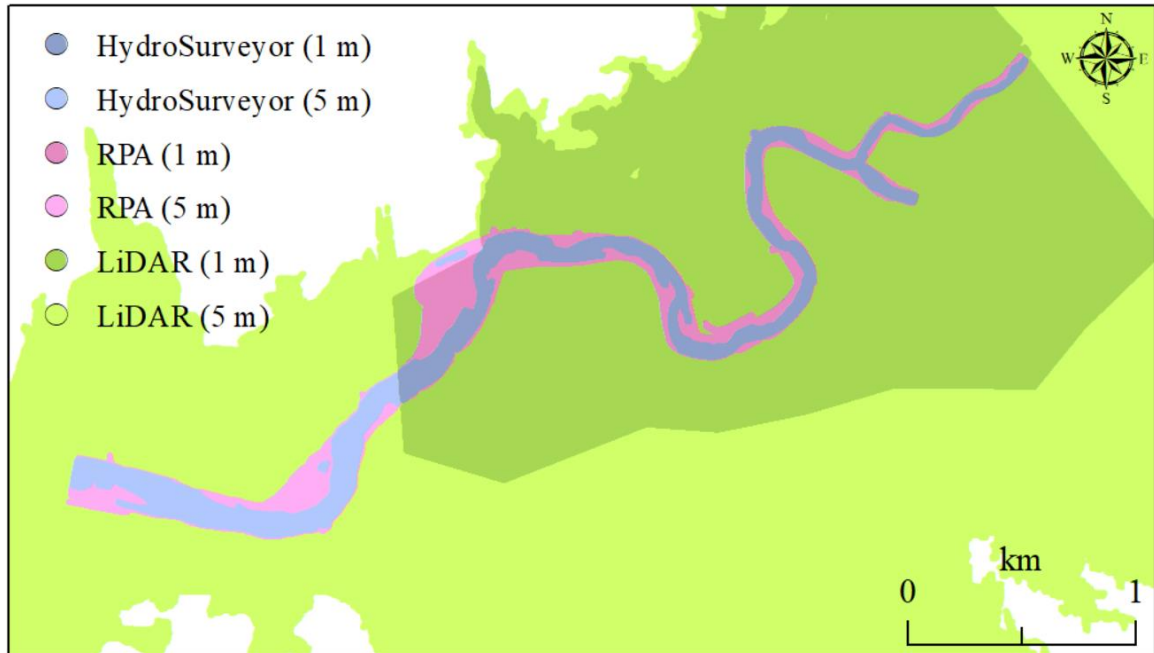


Figure 3.8. Spatial representation of the different data collection methods used to retrieve elevations and the resolutions for the updated 2018 DEM.

Two versions of the 2018 DEM were required: (1) a 2018 DEM with the dykes intact as they existed in 2018 and (2) a 2018 DEM with the dykes breached and aboiteaux removed according to the managed realignment design in Figure 2.2. The dykes were breached and the aboiteaux were removed in ArcMapTM. To breach the dykes, a selection polygon was drawn around each portion of dyke to be breached and the point elevations within the polygon were changed to the average surface elevation of the foreshore marsh in front of each breach. To remove the aboiteaux structures, a selection polygon was

drawn to cut perpendicularly through the dyke and the value of these point elevations within the polygon were changed to the average elevation of the brook or ditch existing behind each aboiteaux structure. The only other features in both versions of the 2018 DEM that were removed were the bridge crossings (Highway 102 Bridge, CN Rail Bridge, Onslow Road Bridge and Park Street Bridge). Once the DEMs were completed, they were exported from ArcMap™ as text files. All subsequent changes to the DEMs were done in Delft3D.

This research also included the use of a DEM (1 m resolution) derived from two surveys conducted in 2013: (1) a LiDAR survey of the Salmon River Estuary in the summer of 2013 and (2) a bathymetric survey in the spring of 2013. The LiDAR survey data are available from GeoNOVA and the bathymetric survey data were collected by CBCL Limited for modelling presented in their flood risk study (2017).

3.3. Hydrodynamic Modelling with Delft3D

3.3.1. Model Description

The Delft3D software suite, developed by Deltares, is a fully integrated computer software with a multi-disciplinary approach that can carry out simulations of flows, sediment transport, waves, water quality, morphological developments, and ecology. This suite is composed of a set of modules, grouped around a mutual interface, that each cover a certain range of aspects of a research or applied problem (Moffatt & Nichol, 2005). These modules can also be coupled with one another. The only module used for this research was Delft3D-FLOW, which uses structured curvilinear grids and calculates non-steady flow and transport phenomena by solving the nonlinear shallow-water equations

derived from the Reynolds-averaged Navier Stokes equation for incompressible free surface flow (Moffatt & Nichol, 2005; Clunies et al., 2017; Lesser et al., 2004). The 2D horizontal momentum equations and the depth-averaged continuity equation solved in Delft3D are found in Appendix A. Multiple studies have used Delft3D to model the hydrodynamics in the Bay of Fundy (Mulligan et al., 2013; Wu et al., 2011; Ashall et al., 2016), but not for the purpose of understanding flooding at a managed realignment site, and not using a high-resolution grid with detailed bathymetry.

3.3.2. *Model Setup*

The model domain extended from the mouth of the Shubenacadie River near Maitland, Nova Scotia to Valley, Nova Scotia along the Salmon River, covering an area of approximately 24 km in the east-west direction by 13.5 km in the north-south direction. The 2D model was implemented on a Cartesian rectangular structured grid of multiple resolutions, with the highest resolution of 6 m at the restoration site and the lowest resolution of 25 m at the outer boundaries of the model domain (Figure 3.9). The maximum number of grid cells in the M-direction was 653, the maximum number of grid cells in the N-direction was 1264 and the total number of grid cells was 352,403.

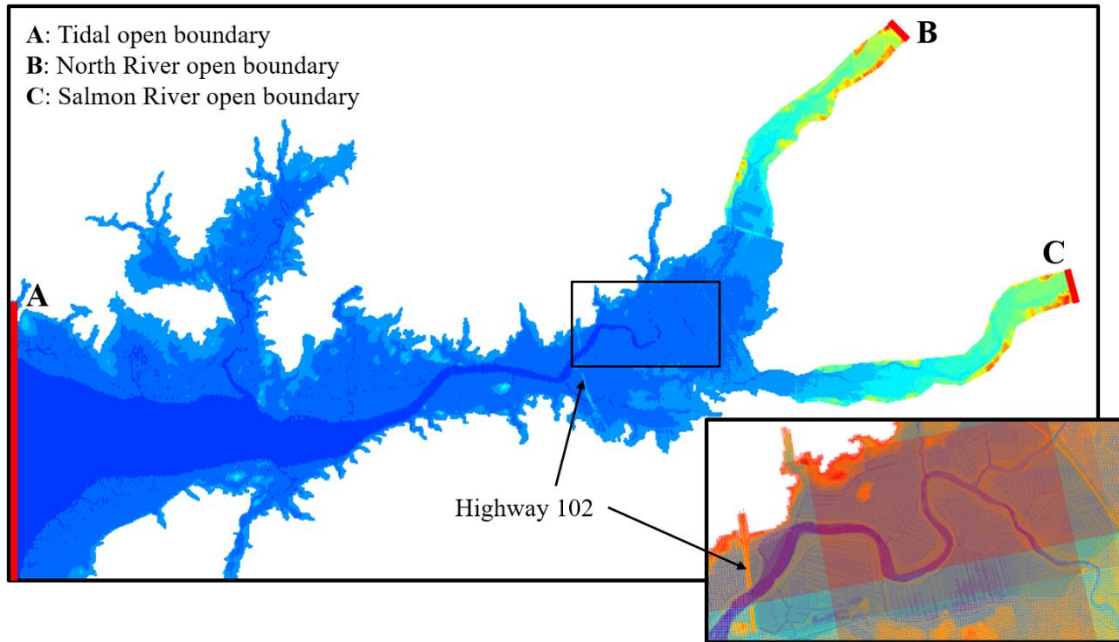


Figure 3.9. The full model domain as illustrated by the input DEM. Blue colours represent lower elevations and red colours represent higher elevations. The inset shows the study area with the model grid overtopping the input DEM. Open boundaries of the model grid are represented by the three red lines labelled A, B and C.

The model grid was created using a boundary fitted grid generation tool called RGFGRID with three open boundaries assigned to the grid (Figure 3.9). These open boundaries let the model know where water propagates from in the simulation. The first open boundary was assigned to the far west side of the model domain (tidal water propagation). The second and third open boundaries were assigned to the far east side of the model domain, one open boundary at the end of each river arm (river discharge).

Once the grid was created and open boundaries were assigned, it was exported from RGFGRID and imported into QUICKIN along with the DEM (in text file format). QUICKIN interpolated the imported DEM to a computational grid. For this research, the following steps were taken to create a computational grid, otherwise known as a depth file in Delft3D. The first step was to assign each grid cell an elevation from the DEM

using a grid cell averaging technique. The portion of the DEM east of Highway 102 was interpolated using an ‘Average Value of Near Points’ technique. For each grid cell, this technique averaged the values of all of the DEM point elevations within the cell boundary and assigned an averaged value to that cell. This averaging technique was used here because it was the default option in QUICKIN and the grid was fine enough within the study area to properly resolve the dykes with appropriate dyke elevations. The portion of the DEM west of Highway 102 was interpolated using a ‘Maximum Value of Near Points’ averaging technique. For each grid cell, this technique identified the DEM point elevation with the highest value within the cell boundary and assigned it to that cell. This averaging technique was used here because the default option resolved the dykes with overall lower elevations, resulting in tidal water overtopping the dykes in the model simulation and flooding areas that do not flood. The next step was to execute an operation called ‘Internal Diffusion’. This assigned an elevation to grid cells that remained empty after performing the grid cell averaging techniques based on the elevations of surrounding cells. The ‘Smoothing’ operation was then applied, which smoothed out any large depth gradients. This was performed along the open tidal boundary and at two locations within the Salmon River where depth gradients were too large and unrealistic. The next step was to multiply all of the grid depth values by -1. This changed negative elevations to positive water depths and areas that are dry to negative values. All the steps just described were applied to all three DEMs. Lastly, small fixes were made to two of the depth files: the depth file created using the 2018 DEM (no breaches) and the depth file created using the 2018 DEM (with breaches and aboiteaux removed). The fixes made were originally overlooked when altering the DEMs in ArcMap™. In both versions of the

2018 depth files, a section of the North River upstream of the CN Rail Bridge had a large depth gradient which was fixed by manually changing the depth values in each grid cell of that small section of the North River. In the 2018 depth file with the dykes breached and aboiteaux removed, the road crossing over McCurdy Brook had to be removed to allow tidal water to flow further upstream if water levels were high enough. The three depth files (2013, 2018 with dykes intact and 2018 with dyke breaches and aboiteaux removed) were then exported from QUICKIN and were ready to load into the model.

The model was run over a period of 6 days with computations performed at a time step of 3 s. The simulation start time was 10:30 am (GMT) on August 9, 2018 and the simulation stop time was 10:00 am (GMT) on August 14, 2018. The model was given 3 days of spin-up time to reach a steady state under the applied tidal and river forcings from the three open boundaries. However, the model was only set to store results for the last four tides of the simulation (from August 12, 2018 to the morning of August 14, 2018), which were the four tides field measurements were collected for. Map results were saved to a file at every 30-minute interval and computations were saved to a file at every 1-minute interval.

The model was forced by tides at the western open boundary and the open boundary conditions were retrieved from WebTide, a tidal prediction model (Dupont et al., 2005). The WebTide model ran from 10:30 am (GMT) on August 9, 2018 to 3:30 pm (GMT) on August 14, 2018. The model simulated 10 tides: 6 tides for model spin-up and 4 tides for field measurement comparisons. The predicted tide elevations from WebTide, referenced to mean sea level (MSL), are illustrated in Figure 3.10.

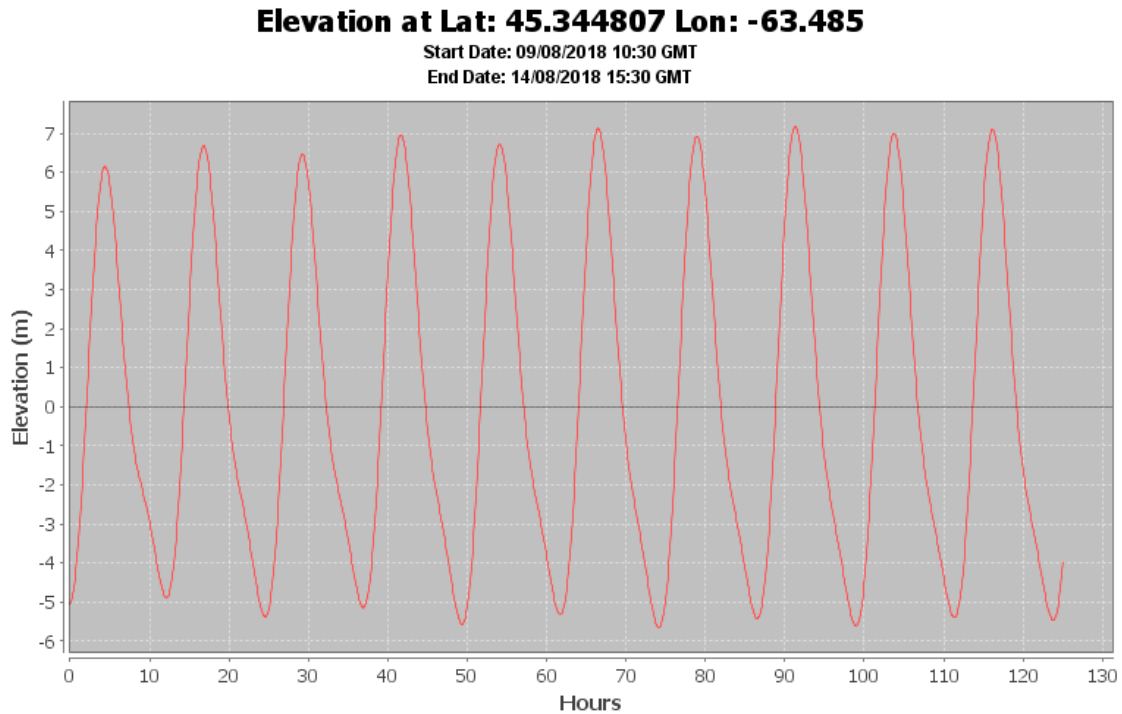


Figure 3.10. Predicted tide elevations (in MSL) from WebTide.

At the other end of the model domain, the two open boundaries in the Salmon River and North River were forced by a time series of river discharges measured by Environment Canada. The data are available from Environment Canada’s Water Office website under Historical Hydrometric Data (2018). However, historical river discharge data were only available for the North River, so a time series of discharge for the Salmon River was estimated based on the ratio of discharges used in the preliminary model runs conducted prior to the present research. In the preliminary model runs, the North River was assigned a single discharge value of $15 \text{ m}^3/\text{s}$ and the Salmon River was assigned a single discharge value of $20 \text{ m}^3/\text{s}$. The discharge in the Salmon River was approximately 1.3 times greater than in the North River, therefore, the August 2018 time series of

measured discharges in the North River was multiplied by 1.3, resulting in a time series with estimated discharges for the Salmon River.

Lastly, in regard to initial model setup, observation points were assigned throughout the model domain corresponding to the locations of the six deployed instruments (Figure 3.1) to directly compare model results to the field measurements. Observation points were used to monitor the time-dependent behaviour of all computed quantities as a function of time at these specific locations. Although observation points for all six instruments were created, only the model results from three observation points (ADV 1 + OBS 1, ADV 2 + OBS 2 and ADCP 1) were used in the analysis for this research. The reason for using only three observation points in the analysis is explained in Chapter 4 – Results.

3.3.3. Model Runs

The modelling process involved many alterations and iterations in order to achieve final results. For this research, 47 simulations were executed with each run building off of the previous. All of these alterations and iterations in the modelling process, and more, are described in a run list found in Appendix F. The following provides an overview of the modelling process carried out for this research.

The first step of the process involved checking different model input files to see if they were formatted correctly and contained the appropriate information, making sure there were no issues with the depth files. The main issue with the depth files was that portions of the dykes within the model domain were not resolved due to unsuitable grid cell averaging techniques. This resulted in the model showing flooding behind the dykes

in areas where flooding does not occur. As for calibrating the model, a simple process was employed. As mentioned earlier, the tide elevations predicted in WebTide were referenced according to MSL and the field measurements were collected and presented in CGVD28. Unfortunately, because there are no permanent water level recorders in the upper Bay of Fundy, there was no way to properly convert the tide elevations from MSL to CGVD28. Therefore, the field measurements collected from August 12 to August 14, 2018 within the study area were used to indirectly “convert” these WebTide tide elevations. This was done by running the model, using the 2018 depth file (dykes intact), with a series of WebTide tide elevation predictions (Figure 3.10), and comparing the modelled water levels at each observation point with the measured water levels from each instrument over the course of four tides. Then, the average difference obtained by subtracting the peak measured water levels from the peak modelled water levels was subtracted from the initial WebTide tide elevations. This change in the open tidal boundary conditions produced model results where the peaks of the measured and modelled water levels matched fairly well. The limitations and assumptions of this calibration method are that the values used to “convert” water levels from MSL to CGVD28 may not be the true offsets for this location, which may have produced unreliable results. In addition, other factors that influence water levels, such as atmospheric pressure, were not accounted for in the model.

Once the model was calibrated and working properly, realistic changes in bathymetry and bottom roughness were made to quantify the model’s response and determine its accuracy. The first model run used the 2018 depth file (dykes intact). Modelled depth averaged velocities were compared to measured velocities at two

instrument locations (ADV 1 + OBS 1 and ADCP 1). Measured velocities at ADV 2 + OBS 2 were discarded because the quality of the data were poor, but water depth measurements were still valid, which is why they were used in calibrating the model. The second model run used the 2013 depth file.

After bathymetry had been changed in the model by inputting different DEMs, the bottom friction coefficient of the model was changed. The bottom friction coefficients selected were 0.002 (Chezy coefficient of 65) and 0.001 (Chezy coefficient of 92). A bottom friction coefficient of 0.002 was selected because it is the default coefficient in Delft3D and a bottom friction coefficient of 0.001 was selected because it is half the roughness of Delft3D's default coefficient. The bottom friction coefficient of 0.002 had already been modelled (the previous model run that used the 2018 DEM (dykes intact)), therefore, the only model run left in this series of sensitivity tests was one that used a bottom roughness coefficient of 0.001. All other parameters and files used in the model remained the same. Once the model was finished running, the modelled depth averaged velocities from both model runs (same 2018 DEM, different bottom friction coefficients) were plotted against the measured velocities. From there, it was determined that the model that used a bottom roughness coefficient 0.001 had to be re-simulated with newly adjusted water levels to match the measured water levels. Once the model was recalibrated, the comparison between the two model results and the measured results could be analyzed properly.

After this series of bathymetric parameter alterations, the parameters used to create the most realistic model results, as compared to observations, were used in a new model run, but this time with the 2018 depth file (dyke breaches and aboiteaux removed)

to determine the flood extent and to observe velocities one might see once the dykes are actually breached. The simulation was executed and results were produced and mapped to show maximum flood extent at the restoration site during Tide 2 (the highest of the four tides that were analyzed for this research). Next, changes in modelled flood extent, average water depth and flood volume within the restoration site were observed by slightly increasing water levels. Water levels were increased in increments of 5 cm from a maximum tide height (in CGVD28) of 9.6 m (representing the scenario with the 2018 depth file with dykes breached and aboiteaux removed and with a Chezy coefficient of 65, where the modelled water levels matched well with the measured water levels) to 9.8 m. An increase in water level of 20 cm could represent future sea level rise, higher tides than those measured for this research or storm surge. Additionally, key statistics (flood area, flood volume, average water depth and maximum water depth) were calculated in MATLAB[®] using the model results for each of the five different maximum tide heights (9.6 m to 9.8 m in 5-cm increments).

After looking at and analyzing how the flood extent and water depths changed for different water levels, the focus was directed to the distribution of modelled velocities throughout the study area (in the river and within the restoration site) by creating velocity maps every 30 minutes throughout Tide 2 for the base case with a maximum tide height of 9.6 m. The sequence of velocity maps started at 40 minutes before high tide (as the tide front passed by the restoration site), ended at 140 minutes after high tide and were paired with their respective flood extent maps.

Lastly, five locations within the Salmon River were selected to compare water levels between the model scenario with no dykes breached and the model scenario with

managed realignment implemented (dykes breached). One location was selected downstream of the restoration site, three locations were selected adjacent to the restoration site and one location was selected upstream of the restoration site.

Chapter 4 – Results

The goal of this chapter is to present the results obtained by applying a numerical model to simulate the tidal hydrodynamics in the present estuary channel that is confined by dykes, and to examine the suitability of the model for predicting possible flood scenarios related to managed realignment of the dykes for controlled flooding. In addition, results from the DEM surveys and field measurements are presented to illustrate the differences between the two DEMs (2013 and 2018) and to contribute to the characterization of the Salmon River Estuary, respectively.

4.1. Field Data

The surveys conducted in the summer of 2018 were used to update the DEM from 2013, both of which were used in this research. The reason for having two DEMs was to investigate the response of Delft3D to changes in bathymetry. The 2013 DEM is shown in Figure 4.1(a), the 2018 DEM is shown in Figure 4.1(b) and the differences in elevation between the two DEMs are shown in Figure 4.1(c).

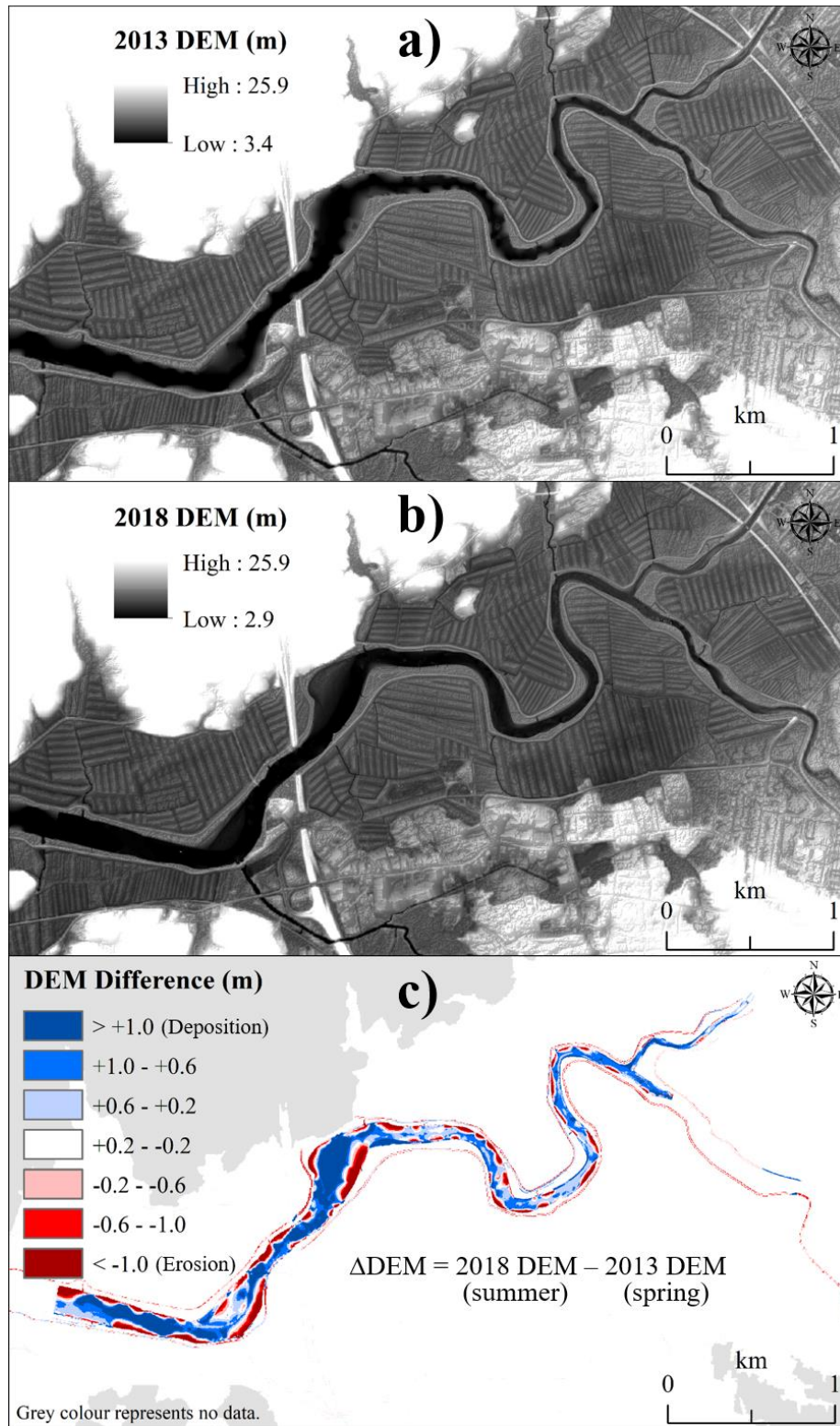


Figure 4.1. The 2013 DEM (a), the 2018 DEM (b) and elevation differences between the two DEMs (c). Elevations are presented in CGVD28.

The changes in elevation from 2013 to 2018 are in un-vegetated areas within the river channels, shown in Figure 4.1(c). The centre of the river channel experienced a net accumulation of sediment of 1 m or greater over this time period, whereas pockets along the edges of the river channel, mainly inside of meander bends, experienced net sediment erosion of 1 m or greater. This indicates overall widening, shallowing and flattening of the channel. The differences between the 2013 and 2018 DEMs are likely related to the time of year during which the data were collected. Although the LiDAR data in the 2013 DEM were collected in the summer, the bathymetry data in the 2013 DEM were collected in the spring. In the spring, there is typically an increase in river discharge, and in the summer, river discharge tends to decrease. Based on 2018 field observations in the North River, sediment deposition rates were high in the summer, with approximately 4 cm of sediment deposited on top of the transducer head of ADCP 2 per tidal cycle. Overall, water depth in the main river channel was shallower in the summer and deeper in the spring. Figure 4.1 is indicative of a dynamic estuary with bed morphology changing significantly in a relatively short period of time.

The hydrodynamic instruments and water samplers measured water depths, velocities (at a single point and throughout the water column) and suspended sediment concentrations over four spring tides from August 12 to August 14, 2018. Figure 4.2 showed the results collected by ADCP 1 for all four tides.

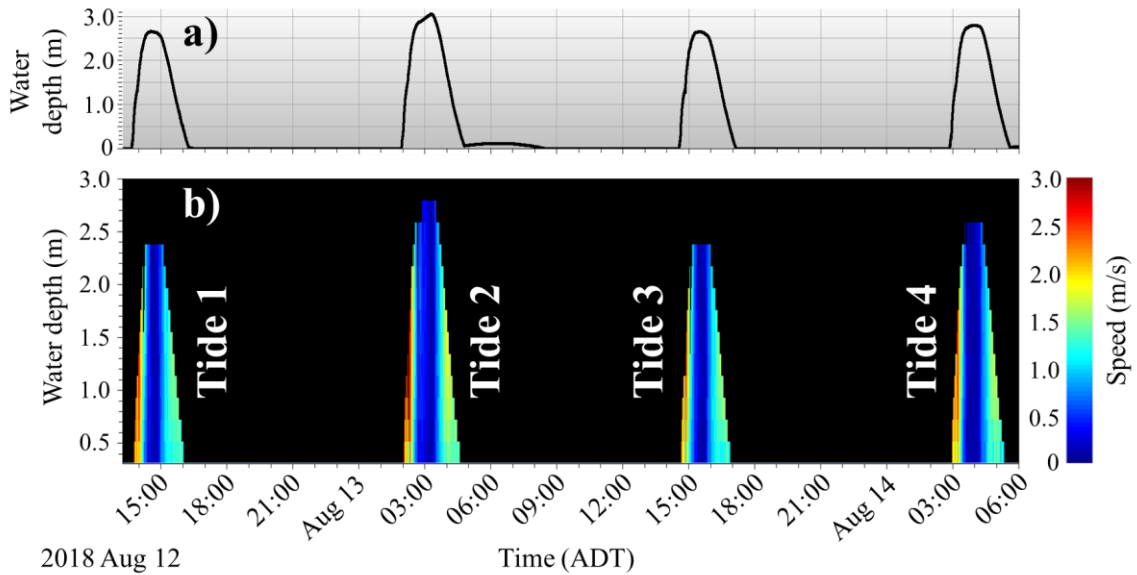


Figure 4.2. Water depths relative to the pressure sensor (a) and speeds (b) measured at the location of ADCP 1 for all four tides.

In Figure 4.2(a), Tide 2 was the highest tide out of the four spring tides, as predicted at Burntcoat Head, with a maximum water depth of 3.05 m. Additionally, one can identify a pattern in speed for all four tides in Figure 4.2(b). At the beginning of each tide, the incoming tide created fast currents, measuring up to 3 m/s. Right before and after high tide, currents fluctuated between 0.5 and 1.2 m/s. At high tide, current speeds dropped to 0.5 m/s and below. At the start of the ebb tide, currents began to increase again until the water dropped below ADCP 1's sensors, but ebb tide velocities were slower than flood tide velocities. A closer view of these profiles are shown in Figure 4.3 for Tide 1 only.

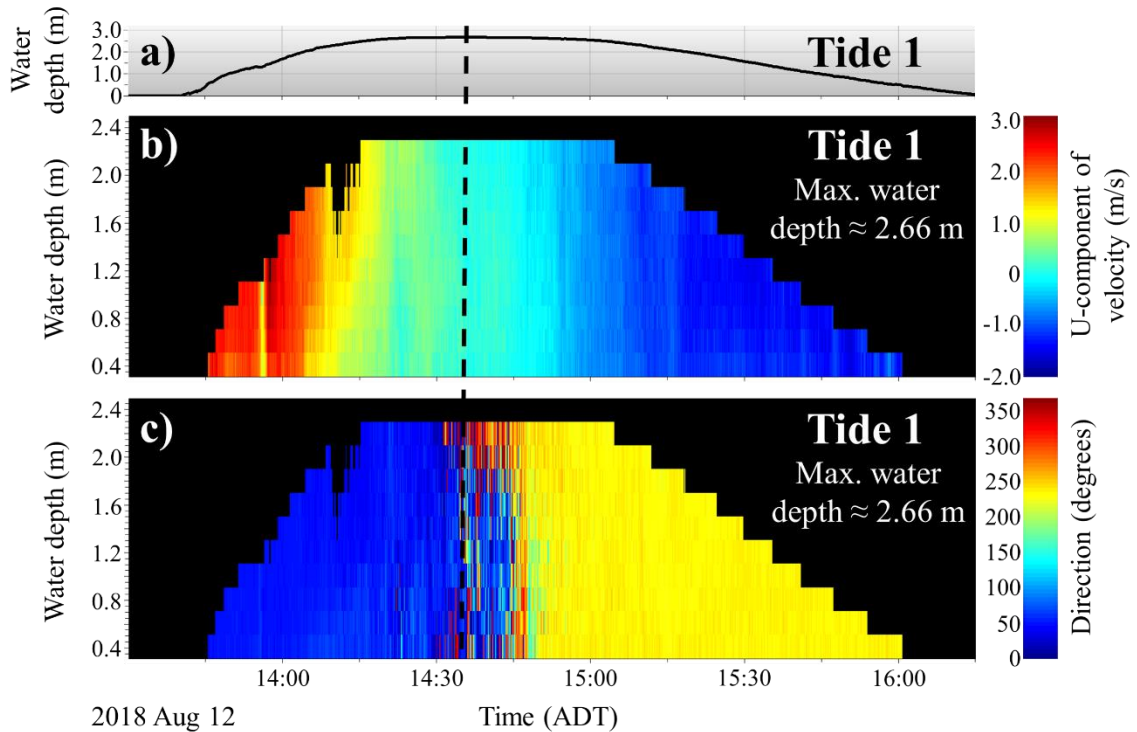


Figure 4.3. Water depths (a), u-component of velocities (b) and flow directions (c) measured at the location of ADCP 1 for Tide 1. The u-component of velocity is parallel to the river channel, which was oriented approximately 45° in the upstream positive x-direction. For flow direction, 0° represents north and increases clockwise. The vertical black dashed line represents the approximate time of high tide.

Similar to the current speeds shown in Figure 4.2(b), the u-component of velocities were high in the positive x-direction along stream (pointing upstream/northeast at the location of ADCP 1) at the beginning of the flood tide. Figure 4.3(b) showed low u-component of velocities close to 0 m/s at, just before and just after high tide, and high u-component of velocities in the negative x-direction (pointing downstream/southwest at the location of ADCP 1) at the end of the ebb tide. In Figure 4.3(c), the direction of the incoming tide fluctuated around 45° (northeast) and the direction of the outgoing tide fluctuated around 225° (southwest). Around high tide the direction of water flow began to fluctuate, making it difficult to pinpoint a dominant flow direction. Within this short period of time was the

180°-change in flow direction. Figure 4.3 also showed that the change in flow direction did not happen simultaneously throughout the water column. The top of the water column changed flow direction first. Lastly, the flood tide was measured over a shorter period of time than the ebb tide. However, the u-component of velocities were much higher during the flood tide than during the ebb tide, meaning the Salmon River Estuary at this location is most likely flood dominant.

Figure 4.4 provided a closer view of the u-component of velocities (in the along-channel x-direction) measured at the location of ADCP 1 for all four tides.

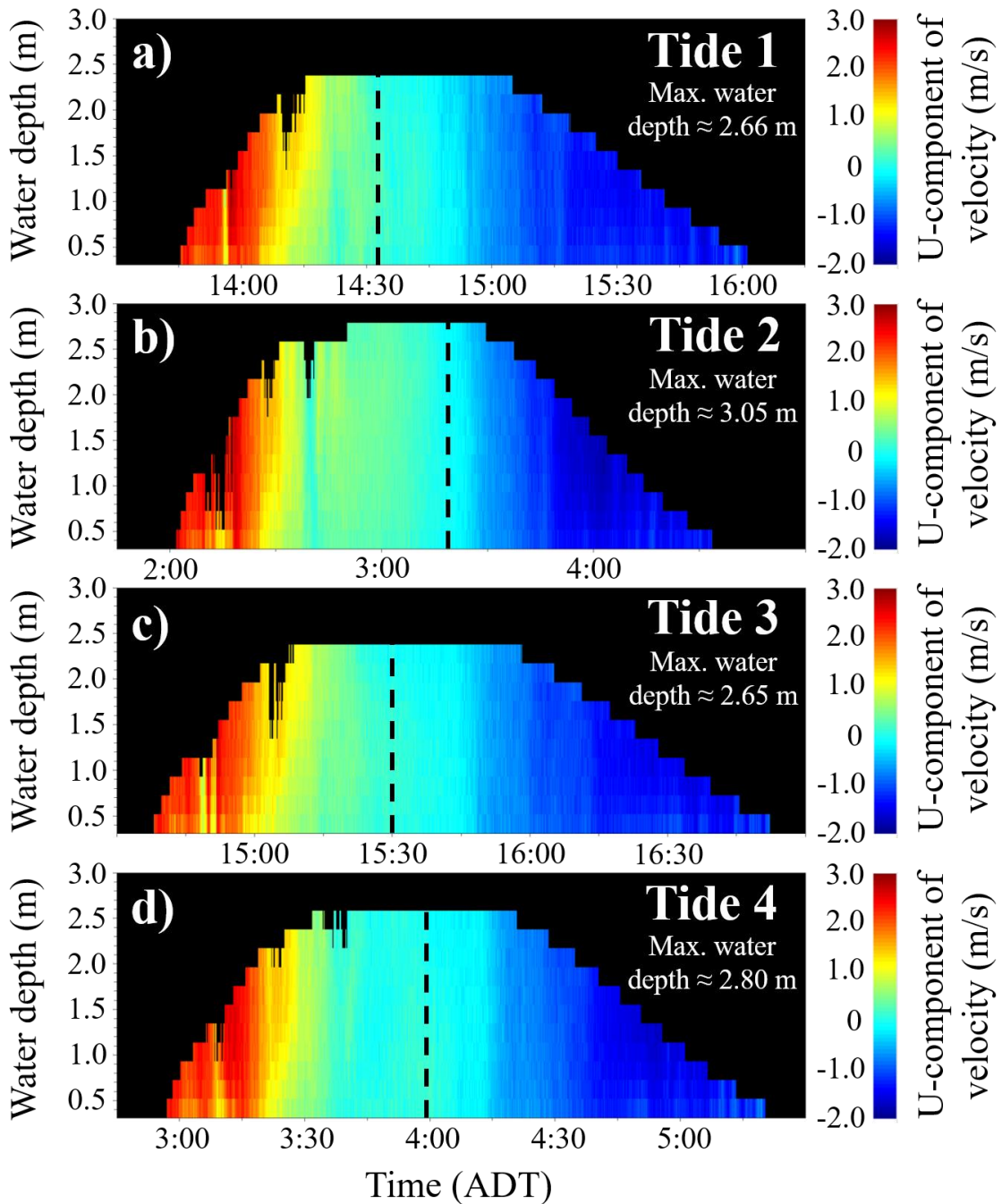


Figure 4.4. *U*-component of velocities measured at the location of ADCP 1 for all four tides. Tide 1 (a) occurred on August 12, Tides 2 (b) and 3 (c) occurred on August 13 and Tide 4 (d) occurred on August 14, 2018. The *u*-component of velocity was parallel to the river channel in the along-channel *x*-direction. The vertical black dashed lines represent the approximate time of high tide for each tide.

Figure 4.4 showed similar u-component of velocities at ADCP 1 throughout the water column and over the duration of each tide, as well as exhibiting flood dominance: shorter, stronger flood tides and longer, weaker ebb tides. However, the time of high tide for Tide 2 (around 3:15 am ADT) almost made the flood and ebb tides equal in duration. Otherwise, the tides had similar velocity profiles and measured velocities. The high tide times for each tide were determined based on the greatest water depth along the water depth curve.

Similar data were collected with the ADCP 2 (in the North River). Unfortunately, due to unsuitable parameters selected when programming the instrument, measurement limitations and extensive sediment deposition on the instrument in this part of the estuary, the data from ADCP 2 are unusable for analysis and model comparison. The data collected by ADCP 2 for all four tides are found in Appendix G.

To help characterize the Salmon River and North River within the boundaries of the study area, different variables were compared by aligning the horizontal time axes to identify relationships at specific times and locations throughout the study area. For example, Figure 4.5 illustrated the relationship between current speed, average signal strength and suspended sediment concentration for Tide 1 at the locations of ADCP 1 and ISCO 1, both of which were deployed west of Highway 102 (Figure 3.1).

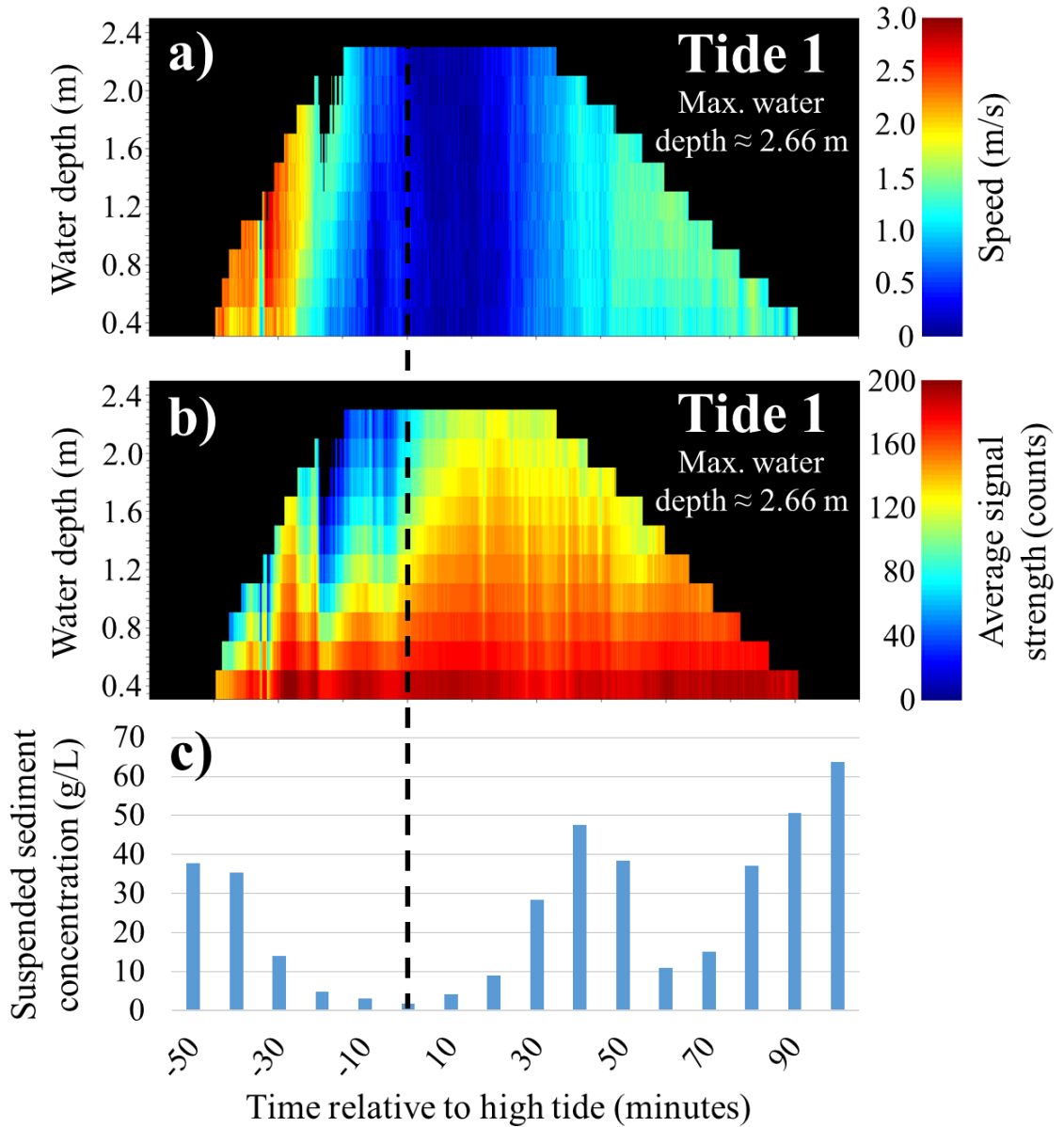


Figure 4.5. Water depths ((a) and (b)), speeds (a) and average signal strengths (b) measured at ADCP 1 and suspended sediment concentrations (c) measured at ISCO 1 for Tide 1. The vertical black dashed line represents the approximate time of high tide.

The average signal strength measured from backscatter, in Figure 4.5(b), was useful since it corresponds to the amount of sediment in the water. However, care must be taken in the analysis of average signal strength when suspended sediment concentrations

are high. A portion of the signal coming from an acoustic instrument can be absorbed by the sediment, reflecting back a portion of the signal that underestimates the amount of sediment in the water (Urick, 2005). The true suspended sediment concentrations calculated from the ISCO 1 data, shown in Figure 4.5(c), gave confidence to the interpretation of average signal strength. The approximate time of high tide, as shown in Figure 4.5(a), separated a short, high-velocity flood tide from a long, low-velocity ebb tide. In Figure 4.5(b), before high tide, there was a sudden increase in average signal strength that aligned with the sudden increase in velocity, shown in Figure 4.5(a), at the beginning of the flood tide. Around high tide, when velocities decreased, average signal strength also decreased. After high tide, average signal strength increased and was sustained throughout the water column for about 30 minutes before it slowly decreased. At 50 minutes after high tide, when velocities started to increase again on the ebb tide, average signal strength also increased until the water line fell below ADCP 1's pressure sensor. The observations shown in Figure 4.5(c) illustrated a similar pattern in the velocity signal to the data shown in Figure 4.5(b). Overall, Figure 4.5 was consistent with the fact that high velocities erode sediment from the river bed and keep it in suspension until velocity begins to decrease, followed by gradual sediment deposition. The one exception to this is the prolonged sediment suspension between high tide and 50 minutes after high tide when velocities were still low. Both ADCP 1 and ISCO 1 recorded this pattern.

A different set of variables were measured at and calculated for the ADV 1 + OBS 1 location. The variables included mean water depth, mean resolved horizontal velocity, mean suspended sediment concentration, mean turbulent kinetic energy and

mean shear velocity (Figure 4.6). ADV 1 + OBS 1 was located just east of Highway 102 in the middle of the study area (Figure 3.1).

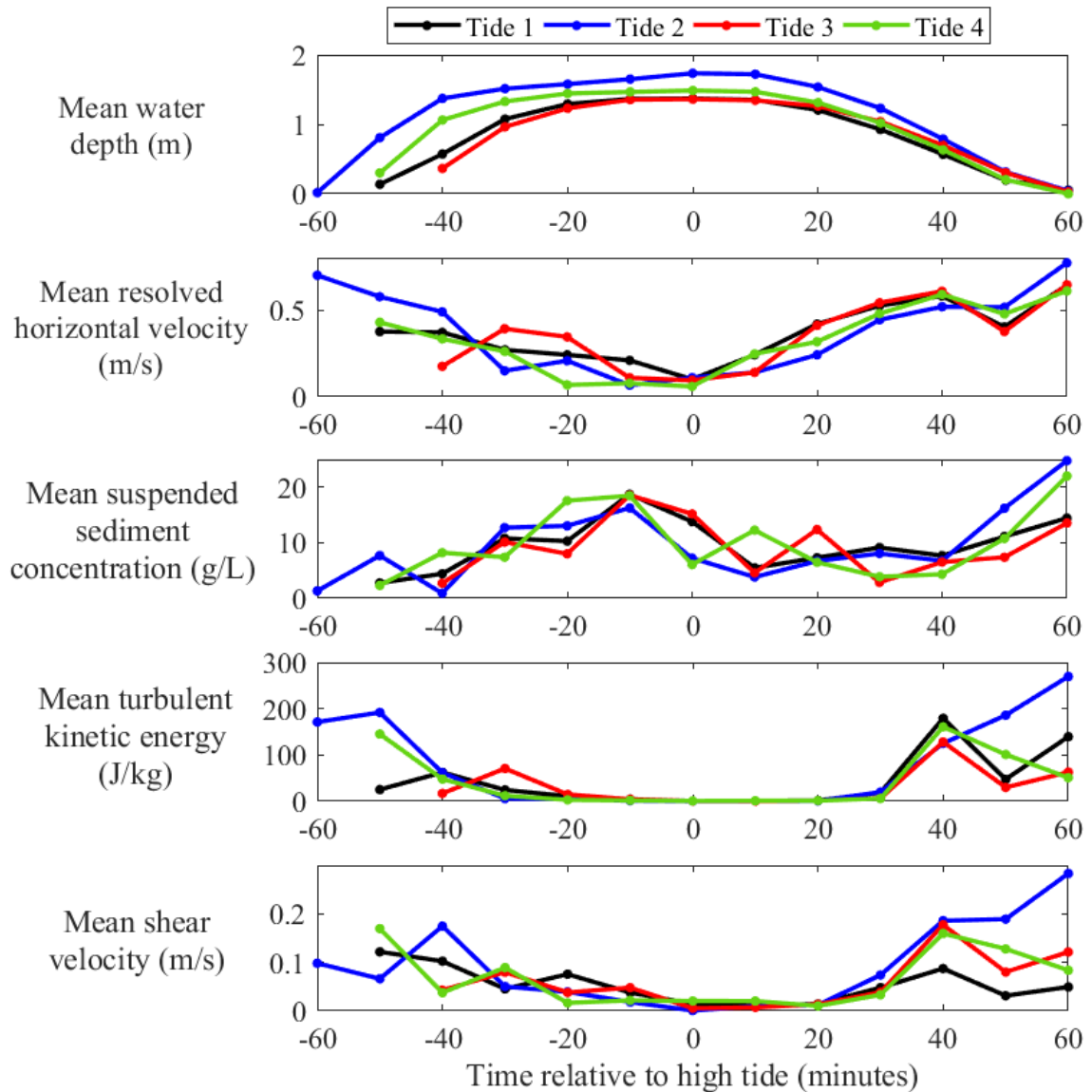


Figure 4.6. Mean water depths, mean resolved horizontal velocities, mean suspended sediment concentrations, mean turbulent kinetic energies and mean shear velocities at the location of ADV 1 + OBS 1 for all four tides.

In Figure 4.6, the only variable the instrument measured, without any subsequent processing, was water depth. Resolved horizontal velocities, turbulent kinetic energies and shear velocities were calculated using the u-, v- and w-components of velocities measured by the instrument. Suspended sediment concentrations were calculated by applying a calibration equation to the raw acoustic signal data (column 16 in Appendix D) measured by OBS 1.

The mean water depth curves showed that Tide 2 was the largest of the four tides, with a water depth of 1.7 m at ADV 1 + OBS 1. Mean resolved horizontal velocities were high at the beginning of the flood tide and even higher at the end of the ebb tide with velocities nearing 0 m/s at high tide. ADV 1 was the only instrument that measured higher ebb tide velocities than flood tide velocities, which does not support that the Salmon River Estuary is flood dominant. However, this observation was only for one location within the inner estuary and could not be used to define the estuary as a whole.

Mean suspended sediment concentrations were low at the beginning of the flood tide, high at the end of the ebb tide and fluctuated in concentration around high tide. At 10 minutes before high tide, the suspended sediment concentration for all four tides reached a peak of 18.7 g/L, which exceeds the threshold for fluid mud. Mean turbulent kinetic energy provides an indication of turbulence, or eddies, within the water column that keep sediment suspended. The curves of turbulent kinetic energy, in Figure 4.6, showed a similar pattern to that of resolved horizontal velocity, but this is because both variables were derived from the measured u-, v- and w-components of velocity. Mean shear velocity provides an indication of how fast water must flow against the river bed in order to entrain sediment. An increase in shear velocity would result in more

resuspension of material. The curves of shear velocity, in Figure 4.6, were similar to that of turbulent kinetic energy. However, it is important to note the difference in scale between the plots of mean resolved horizontal velocity and mean shear velocity. Although their patterns were similar, mean shear velocities were, on average, 0.3 m/s slower than mean resolved horizontal velocities. This is because of the friction applied to the flowing water by the rough surface of the river bed. Overall, the patterns for all variables in Figure 4.6 were relatively consistent for all four tides, with any deviations at the very beginning and end of tides.

The following ISCO results helped characterize the river system and supported that the Salmon River Estuary is dynamic and exhibits different trends at different locations throughout the study area. Figure 4.7 illustrated the distribution of suspended sediment concentration over all four tides for ISCO 1 and ISCO 2. For the entirety of the ISCO deployments, both nozzles from ISCO 1 and ISCO 2 remained underwater, even at low tide. Hence, why Figure 4.7(b) showed concentrations for almost 4 hours after high tide, at which point water levels should be close to or at their lowest.

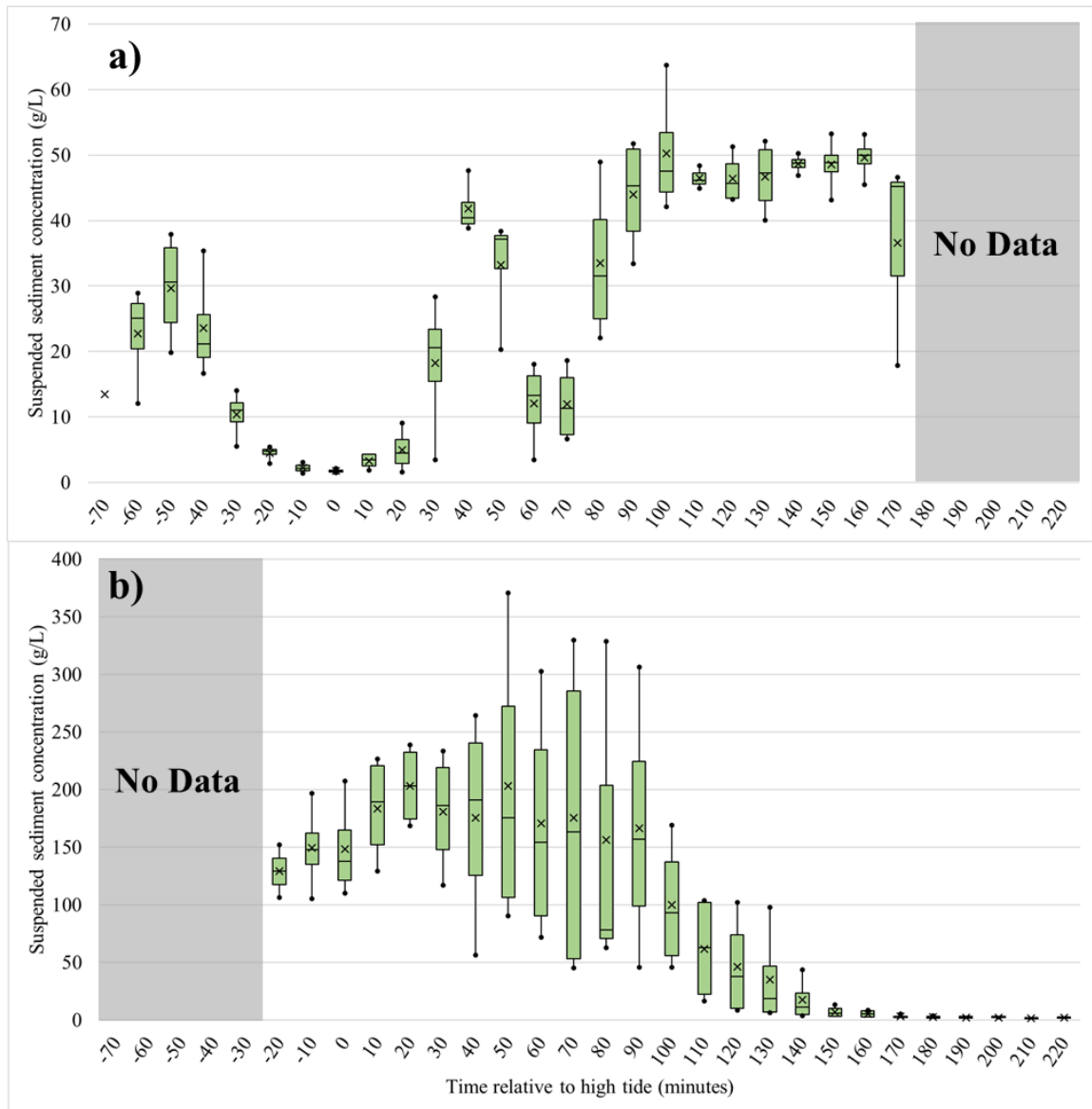


Figure 4.7. Box and whisker plot of suspended sediment concentration over all four tides at the locations of ISCO 1 (a) and ISCO 2 (b). The boxes represent the interquartile range, the horizontal lines within the boxes represent the median concentrations of the datasets for a given time, the 'x' markers represent mean concentrations and the dots at the ends of the bottom and top whiskers represent the minimum and maximum concentrations of the datasets for a given time, respectively. The grey boxes indicate that no data were collected for that period of time. Note the difference in scale between the two y-axes.

At ISCO 1, suspended sediment concentrations fluctuated throughout each tide from 1.43 g/L to 63.7 g/L, with most sample concentrations above the fluid mud

threshold of 10 g/L (Wang, 2010; Faas, 1991). From 50 minutes before high tide to 40 minutes after high tide, the curve is u-shaped, which is what one would expect to see, especially with velocity/speed measurements at a nearby instrument (ADCP 1 in Figure 4.2 through Figure 4.5) with a similar u-shaped curve. From 50 minutes after high tide to the end of the sampling period, there was a sharp increase in suspended sediment concentration, which then plateaued at about 48 g/L. This was most likely due to the high flow velocities at the end of the ebb tide. ISCO 2 was located further upstream (in the North River) than ISCO 1 and showed a different trend as well as much higher suspended sediment concentrations. Unfortunately, ISCO 2 did not collect much data before high tide as the instrument was programmed to start at a time well after the tidal bore had passed by. At ISCO 2, suspended sediment concentrations at high tide were an average of 148 g/L for all four tides, which is generally very high, and reached a maximum of 370 g/L shortly after (this value was sampled during Tide 2). Afterwards, suspended sediment concentration gradually decreased until the curve plateaued at almost 0 g/L, which was likely a reflection of freshwater fluvial discharge.

What is important to recognize, based on all these field results, is that the inner Salmon River Estuary, at least within the study area, was very dynamic, powerful and exhibited different trends throughout a tidal cycle at different locations. There is also the argument that seasonal conditions are the dominant influence on sedimentation in this portion of the Salmon River Estuary. As discussed earlier for Figure 4.1(c), there was more sediment deposition than erosion from 2013 (spring) to 2018 (summer). This implied that during the summer of 2018, river bed elevations were generally higher than they were in the spring of 2013. This can be further supported by the field observations,

made in the summer of 2018, of estimated sediment deposition rates of 4 cm per tide in the North River. It was clear that there was a great amount of sediment deposition higher up in the Salmon River Estuary during the summer months.

4.2. Model Results

4.2.1. Response of the Model to Changes in Bathymetric Parameters

The first set of model results focused on the response of the model to changes in two parameters: the DEM and the bottom friction coefficient. Identifying how the model outputs changed based on changing these two parameters was the main goal. The results provided an indication of model sensitivity and how that could impact its application as a tool in future managed realignment projects. Throughout this section, the models were calibrated using measured water levels. Water levels at the tidal boundary were adjusted iteratively until there was a close enough match between the peak values of the measured and modelled water levels. The true comparison was done with the velocity plots, which were not adjusted nor used to calibrate the model.

Figure 4.8 through Figure 4.10 showed model results before and after changing only the DEM, with a constant bottom friction coefficient of 0.002. Figure 4.8 illustrated measured and modelled water levels and magnitude of depth averaged velocities for all four tides at the location of ADCP 1.

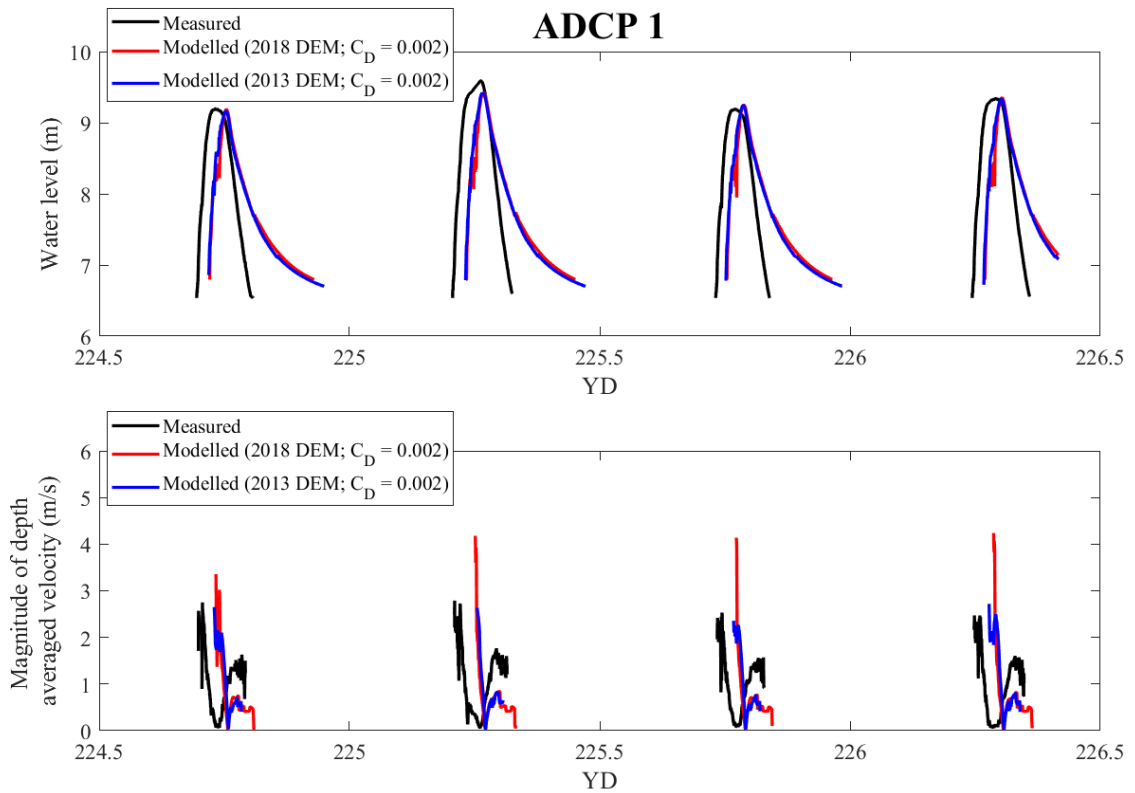


Figure 4.8. Measured (black line) and modelled water levels (in CGVD28) and magnitude of depth averaged velocities at the location of ADCP 1. The two models used a bottom friction coefficient (C_D) of 0.002. The red line represents the model results simulated using the 2018 DEM and the blue line represents the model results simulated using the 2013 DEM.

The top panel showed the comparison of measured water levels with two model results: one simulated using the 2013 DEM (blue line) and one simulated using the 2018 DEM (red line). The two model results for water level matched very well, especially at peak water levels, and there was no difference in phase or amplitude between the two modelled results. This indicated that a change in bathymetry from the 2018 DEM to the 2013 DEM did not change water levels. However, there was a notable difference between the modelled results and the measured results (black line) for water level. Measured results for each of the four tides showed almost perfect symmetry about an imaginary vertical

axis at high tide. The two modelled results did not show the same symmetry. The modelled water level curves had a similar slope for the flood tide and similar peak water levels at high tide, but a very different and changing slope for the ebb tide. Measured water levels for the ebb tide were the mirror image of the preceding flood tide, but the modelled water levels for the ebb tide showed a decrease in water level over a longer period of time, creating the appearance of a tail at the end of each tide. The slope also appeared logarithmic or exponential as opposed to the relatively linear trend of decreasing water levels in the measured results. This indicated that the model simulated a much longer ebb tide. The other notable difference between the measured and modelled results was the phase shift along the time axis. The model simulated the tides a maximum of 32 minutes later than the measured tides occurred. It was speculated that the reason for this lies with the value chosen for the bottom friction coefficient. The bottom friction coefficient selected for these two model runs ($C_D = 0.002$) was most likely higher than it should have been to create an accurate, representative model. In other words, the “river bed” in the model had greater roughness and more friction than in reality. This would theoretically cause the simulated tide to occur after the measured tide, which was illustrated in Figure 4.8. Lastly, the phase shift between the measured and modelled results for Tide 1 (32 minutes) was larger than for Tide 4 (17 minutes). This implied that the longer the model runs for, the smaller the phase shift. This may be attributed to selecting an inadequate amount of time for model spin-up. In summary, this shift may be present for one of two reasons: either the bottom friction coefficient was incorrect, or there was not enough model spin-up time before the last four tides.

In the bottom panel of Figure 4.8, the velocity curves illustrated the same phase shift between the modelled and measured results. Again, like with the water levels, the two modelled velocity curves were relatively the same. The only differences were that the 2018 DEM model run simulated greater velocities at the beginning of the flood tide than the 2013 DEM model run and that the tail end of the 2013 DEM modelled velocity curves were cut off earlier than those represented in the 2018 DEM model run. In terms of the shape of the velocity curves, the modelled results were comparable to the measured results, however, the 2013 DEM modelled velocity results were a better match with the measured results than the 2018 DEM modelled velocity results because the velocities at the beginning of the flood tide were much closer in magnitude. Another deviation from the shape of the measured velocities was that both modelled velocity results were consistently 1 m/s lower, on average, near the end of the ebb tide. Lastly, both modelled velocity curves, for all four tides, were narrower than the measured velocity curves. This indicated that the model simulated each tidal cycle over a shorter period of time than what occurred, based on the field measurements.

Figure 4.9 illustrated measured and modelled water levels and magnitude of velocities for all four tides at the location of ADV 1 + OBS 1. These results were extracted from the same model run that produced the results shown in Figure 4.8.

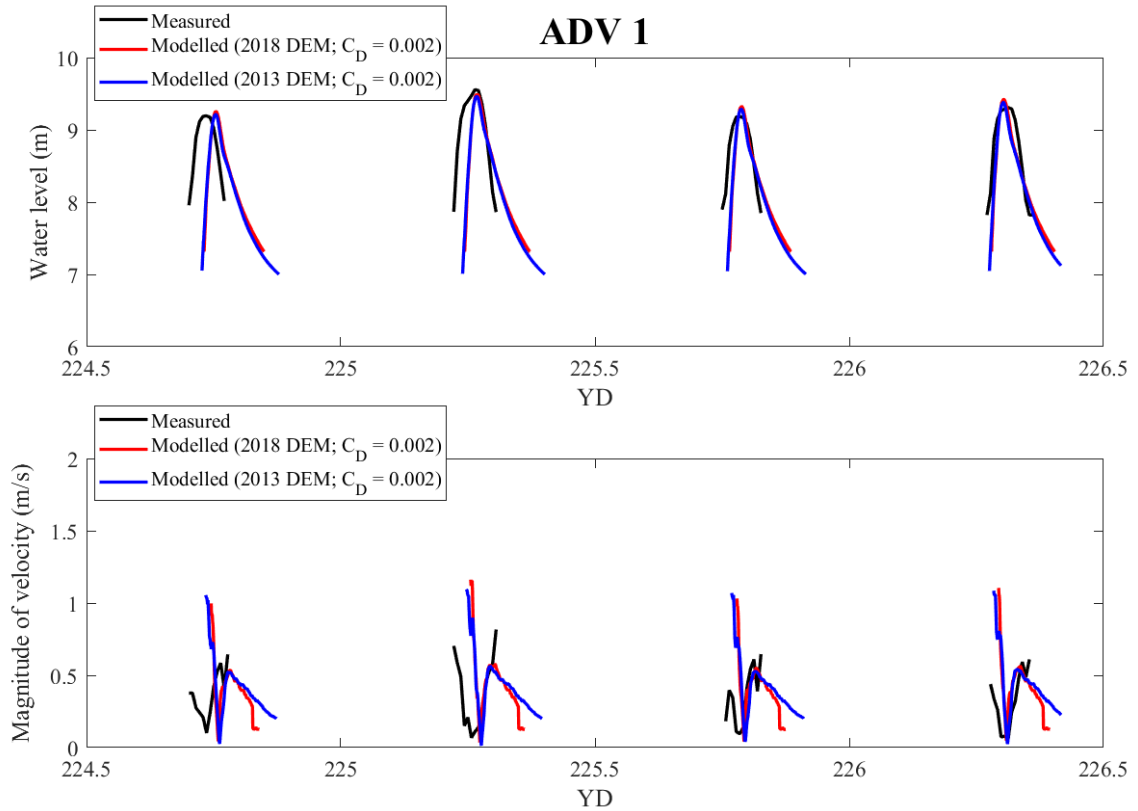


Figure 4.9. Measured (black line) and modelled water levels (in CGVD28) and magnitude of velocities at the location of ADV 1 + OBS 1. The two models used a bottom friction coefficient (C_D) of 0.002. The red line represents the model results simulated using the 2018 DEM and the blue line represents the model results simulated using the 2013 DEM.

The measured and modelled results for water levels at ADV 1 + OBS 1 (Figure 4.9) were very similar to those at the location of ADCP 1 (Figure 4.8); the curves were similar in shape, the phase shift still existed and the comparison between measured and modelled results were the same, with one exception. At ADV 1 + OBS 1, the measured water level curves began and ended at 7.8 m (CGVD28), but the 2018 and 2013 DEM water level curves began and ended at 7.3 m and 7 m, respectively. However, at the location of ADCP 1 (Figure 4.8), the measured and modelled water level curves began and ended at relatively similar elevations: 6.7 m on average. This meant that the bed elevation did not

change significantly from 2013 to 2018 at ADCP 1. On the other hand, the bed elevation at ADV 1 + OBS 1 was most likely higher in 2018 than it was in 2013, if one compares the black curve (measured) with the blue curve (modelled with the 2013 DEM). Figure 4.1(c) illustrated increased elevations at this location and supported this observation. The red water level curve (modelled with the 2018 DEM) was expected to begin and end, for each tide, at the same bed elevation as the measured water level curve, but this was not the case. It is important to note that the data in between each tide represented measured and modelled water levels and velocities at low tide. Within this period of time, measured and modelled water levels dropped below the elevation of the instruments' pressure sensors. In these plots, this manifested as straight lines at the pressure sensor elevations for each water level curve. These straight lines did not represent the actual water levels at these instrument locations because the water level continued to drop in elevation even after it reached the pressure sensors. This is why the data was removed in between each high tide curve.

For the most part, the curves of measured and modelled magnitude of velocities in Figure 4.9 were similar in comparison, like in Figure 4.8. However, there was one new observation to be addressed for the velocities measured and modelled at ADV 1 + OBS 1: the difference in magnitude of velocities between the measured and two modelled results at the beginning of the flood tides. Measured velocities were not as high as what the model simulated. Measured flood tide velocities were also lower than measured ebb tide velocities for each of the four tides at ADV 1 + OBS 1. The opposite was measured at ADCP 1.

Figure 4.10 illustrated measured and modelled water levels for all four tides at the location of ADV 2 + OBS 2. Only water levels are shown because all velocity data retrieved from ADV 2 and OBS 2 were poor in quality and discarded. The measured water level data for Tide 1 were also discarded because high flow velocities significantly tilted the instrument and forced the instrument head into the mud (Figure 4.11). These results were extracted from the same model run that produced the results shown in Figure 4.8 and Figure 4.9, and the observations and analyses remain the same. Like in Figure 4.8, the water level curves for each tide began and ended at a similar elevation: 7.6 m on average.

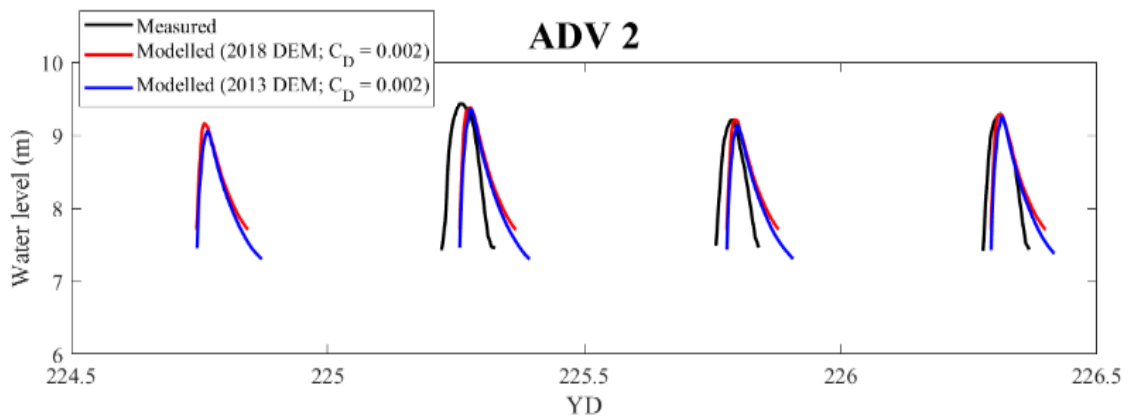


Figure 4.10. Measured (black line) and modelled water levels (in CGVD28) at the location of ADV 2 + OBS 2. The two models used a bottom friction coefficient (C_D) of 0.002. The red line represents the model results simulated using the 2018 DEM and the blue line represents the model results simulated using the 2013 DEM.



Figure 4.11. ADV 2, and the attached OBS 2, tilted in the upstream direction in the Salmon River at low tide after Tide 1.

The next set of results (Figure 4.12 through Figure 4.14) illustrated the response of the model to small changes in bottom roughness. The bottom friction coefficient of the model was changed from 0.002 to 0.001, resulting in a smoother river bed. However, before these model results could be properly compared to the measured results, the model had to be calibrated again. Initial results showed an increase in modelled water levels by an average of 30 cm at high tide and during the flood tide, but showed a decrease in modelled water levels by an average of 25 cm during the ebb tide compared to the previous model results. This change was observed for all four tides. Modelled velocities increased compared to the previous model results as well, but by how much depended on location. At ADCP 1, modelled velocities increased somewhere between 1.5 m/s and 3.2 m/s at the beginning of the flood tides and increased by an average of 0.63 m/s at the peak of the ebb tides. At ADV 1 + OBS 1, modelled velocities increased by an average of 0.51 m/s, but only at the peak of the ebb tides. Other than these changes, the two sets of

modelled velocities were very similar. Increased water levels with subsequent increases in velocity made sense because larger volumes of water flow faster than smaller volumes of water in an equally sized channel. Lastly, the change in bottom roughness resulted in a phase shift, for all four tides at all three instrument locations, where the peaks of the modelled water level curves were simulated 15 minutes earlier than the modelled water level peaks with a rougher bed. This finding made sense because water will propagate through the entire model grid faster with a smoother river bed (less friction restricting flow), causing the peak of high tide to occur sooner. These measured and modelled results at three instrument locations (ADCP 1, ADV 1 + OBS 1 and ADV 2 + OBS 2) are located in Appendix H. The water levels at the tidal boundary were then adjusted for subsequent models until the modelled water levels matched well with the measured water levels.

Figure 4.12 through Figure 4.14 showed model results before and after changing the bottom friction coefficient (post-recalibration). Figure 4.12 illustrated measured and modelled water levels and magnitude of depth averaged velocities for all four tides at the location of ADCP 1. The only parameter changed was the bottom friction coefficient and the DEM remained the same for both model runs.

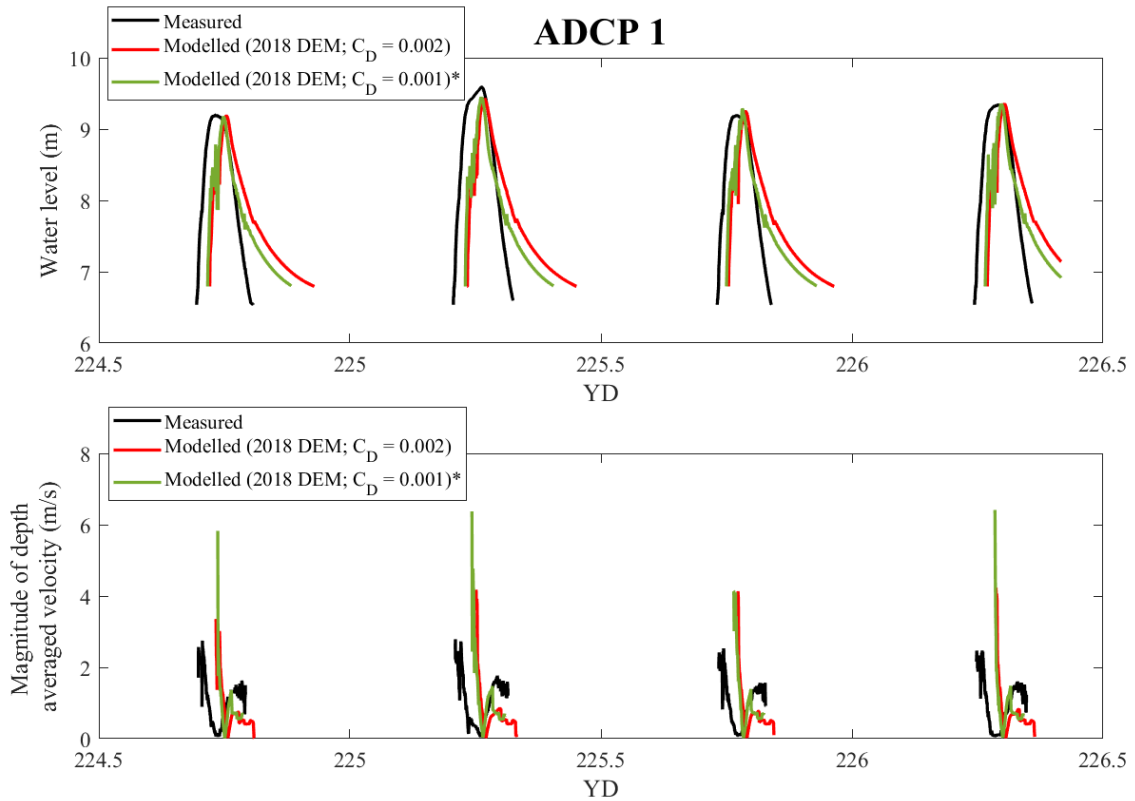


Figure 4.12. Measured (black line) and modelled water levels (in CGVD28) and magnitude of depth averaged velocities at the location of ADCP 1. The two models used the 2018 DEM. bottom friction coefficient (C_D) of 0.002. The red line represents the model results simulated using a bottom friction coefficient (C_D) of 0.002 and the green line represents the model results simulated using a bottom friction coefficient (C_D) of 0.001. The asterisk (*) indicates that the model results were generated after adjusting water levels at the tidal boundary to match measured water levels.

Observations and analysis of the measured vs. modelled water levels in Figure 4.12 were the same as for Figure 4.8 (same location), except for a small phase shift and a change in water levels between the two modelled results. The model with a bottom friction coefficient of 0.001 simulated water levels that were lower than those simulated with a bottom friction coefficient of 0.002, but only on the ebb tide, similarly to the results in Appendix H. Observations and analysis of the measured vs. modelled velocities in Figure 4.12 were the same as for the first figure (results at the location of ADCP 1) in Appendix

H, except both velocity simulations for Tide 3 were similar at the beginning of the flood tide.

Figure 4.13 illustrated measured and modelled water levels and magnitude of velocities for all four tides at the location of ADV 1 + OBS 1. These results were extracted from the same model run that produced the results shown in Figure 4.12.

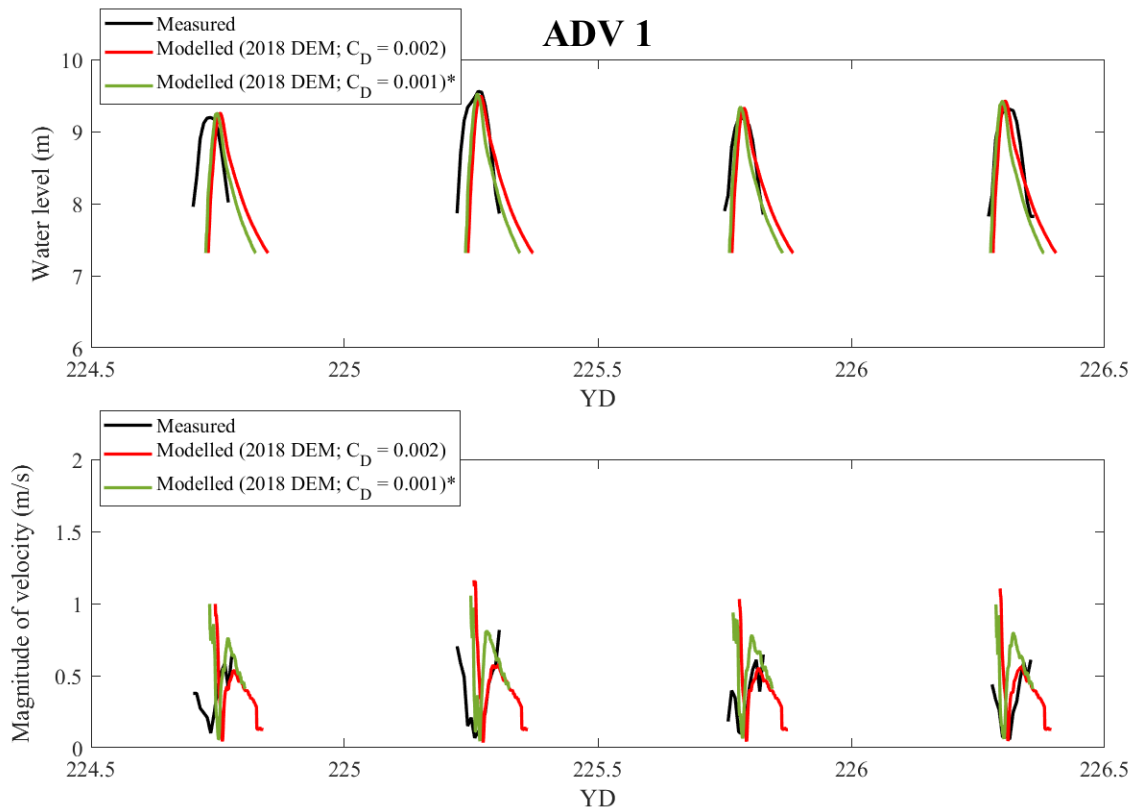


Figure 4.13. Measured (black line) and modelled water levels (in CGVD28) and magnitude of velocities at the location of ADV 1 + OBS 1. The two models used the 2018 DEM. The red line represents the model results simulated using a bottom friction coefficient (C_D) of 0.002 and the green line represents the model results simulated using a bottom friction coefficient (C_D) of 0.001. The asterisk (*) indicates that the model results were generated after adjusting water levels at the tidal boundary to match measured water levels.

For Figure 4.13, observations and analysis of measured and modelled water levels were the same as for Figure 4.12. Observations and analysis of measured and modelled velocities in Figure 4.13 were the same as for the second figure (results at the location of ADV 1 + OBS 1) in Appendix H.

Lastly, Figure 4.18 illustrated measured and modelled water levels for all four tides at the location of ADV 2 + OBS 2. These results were extracted from the same model run that produced the results shown in Figure 4.12 and Figure 4.13, and the observations and analyses remained the same.

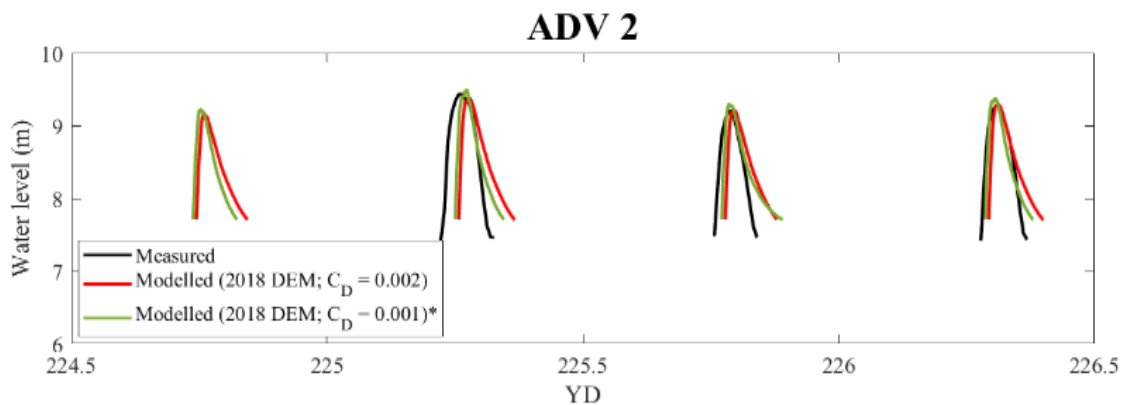


Figure 4.14. Measured (black line) and modelled water levels (in CGVD28) at the location of ADV 2 + OBS 2. The two models used the 2018 DEM. The red line represents the model results simulated using a bottom friction coefficient (C_D) of 0.002 and the green line represents the model results simulated using a bottom friction coefficient (C_D) of 0.001. The asterisk (*) indicates that the model results were generated after adjusting water levels at the tidal boundary to match measured water levels.

It can be concluded that Delft3D was successful at simulating hydrodynamic conditions similar to those measured in the field. Model results also showed that small, realistic changes in bathymetry and bottom roughness resulted in relatively minor changes in hydrodynamic conditions. The three most notable changes were an increase in

water levels following a decrease in bottom roughness, a decrease in phase shift caused by a decrease in bottom roughness and differences in velocity between the two model results at the beginning of the flood tides and throughout the ebb tides. The 2018 DEM and a bottom friction coefficient of 0.002 were used in the remaining model runs because the 2013 DEM was outdated and the change to a bottom friction coefficient of 0.001 resulted in a 30-cm increase in water levels (on average) and a large increase in velocities at the beginning of the flood tide (up to 3.2 m/s).

Further analysis was done for one of the model runs discussed above with the intention of gaining further insight into the model's ability to reproduce conditions that were observed in the field. Figure 4.15 is a map of modelled magnitude of depth averaged velocities in the Salmon River at the beginning of the flood tide for Tide 2. This model run used the 2018 DEM (no breaches) and the default bottom friction coefficient.

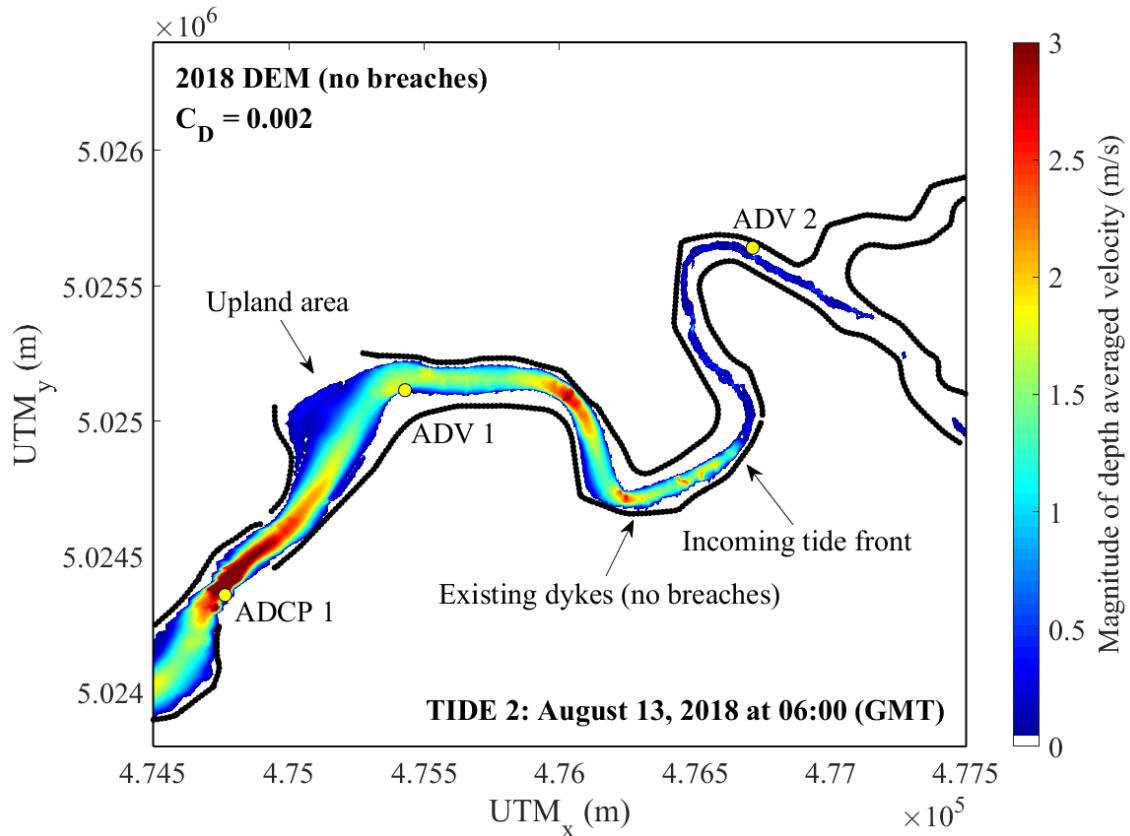


Figure 4.15. Modelled magnitude of depth averaged velocities at the beginning of the flood tide for Tide 2. Model results were simulated using the 2018 DEM and a bottom friction coefficient of 0.002. The black line represents the existing dyke infrastructure with no breaches.

All models were programmed to output maps of the results at 30-minute intervals, with one of the intervals (shown in Figure 4.15) capturing the incoming tide front. Although Delft3D did not simulate the tidal bore moving up the river, the clear increase in velocity at the leading edge of the incoming tide may be an indication of the approximate position of the tidal bore at that point in time. Another important finding was the locations of high velocities relative to other parts of the river. For example, Figure 4.15 showed higher velocities at the meander bends in the river, such as the first two bends upstream of ADV 1 + OBS 1. Figure 4.15 also showed the highest velocities within the study area at the

location of ADCP 1. The reason for this was that the Salmon River was narrower at this location, and when water of a constant volume flows through a constricted section of the channel it increases in speed. This particular model result was supported by field observations at the general location of ADCP 1 and ISCO 1. Figure 4.16 showed pictures of the calm state of the river and the turbulent state of the river at the channel constriction before and after the tidal bore had passed through, respectively.

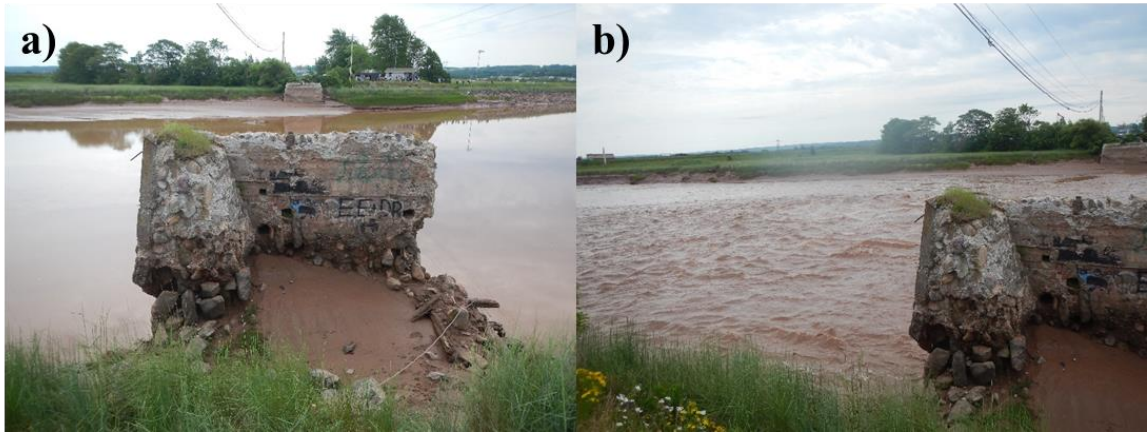


Figure 4.16. *The Salmon River near ADCP 1 and ISCO 1 before (a) and after (b) the tidal bore passed through. In the photos, upstream is left and downstream is right.*

Figure 4.17 showed another map of modelled magnitude of depth averaged velocities in the Salmon River, but for Tide 1 during the flood tide. The model parameters used were the same as in Figure 4.15.

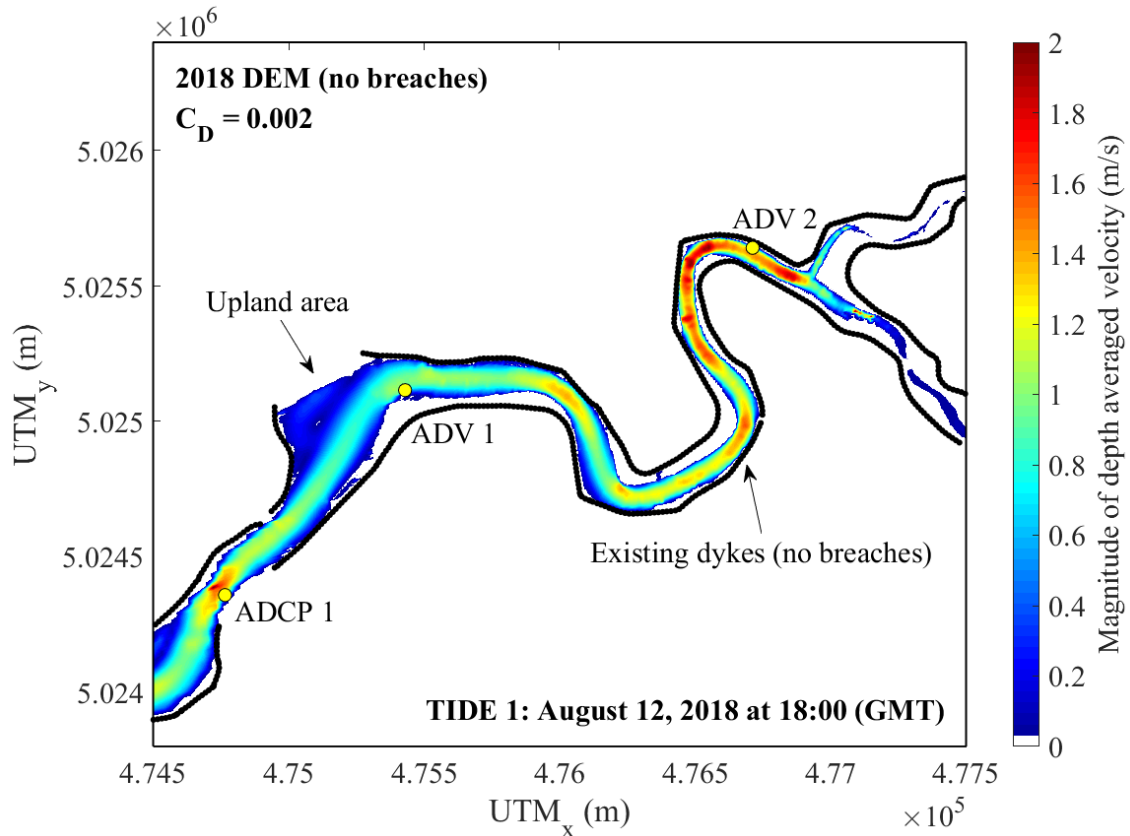


Figure 4.17. Modelled magnitude of depth averaged velocities during the flood tide of Tide 1. Model results were simulated using the 2018 DEM and a bottom friction coefficient of 0.002. The black line represents the existing dyke infrastructure with no breaches.

Figure 4.17 illustrated Delft3D's ability to simulate higher velocities at meander bends and areas of channel constriction. Not only did it show higher velocities in those locations, but in the middle of the channel as well, as opposed to the outer edges of the channel. This was shown along the whole river and was due to friction along the river's edge acting against the flow of water. Figure 4.17 also showed relatively high velocities at the location of ADV 2 + OBS 2. Field observations at ADV 2 + OBS 2 supported the model's simulation of high velocities because the currents at this location during Tide 1 were high enough to tilt the instrument in the direction of flow (Figure 4.11).

4.2.2. Impact of Increasing Water Levels on Modelled Flood Extent within the Restoration Site

The second set of model results focused on modelling with the existing dykes breached according to the managed realignment design (Figure 2.2). The findings provided insight into whether a hydrodynamic model, i.e., Delft3D, is a reliable and applicable tool for future managed realignment projects, and more specifically, what the possible flood scenarios were for this specific project site.

Figure 4.18 through Figure 4.22 illustrated maximum flood extent within the restoration site at high tide during Tide 2, the largest of the four recorded tides. The only difference between each model simulation was the water levels at the tidal boundary, resulting in different maximum flood extents. The 2018 DEM (with dykes breached, according to the restoration design by CBWES in Figure 2.2, and aboiteaux removed) and a bottom friction coefficient of 0.002 were used for all five models. The first simulation of flooding within the restoration site used the same water levels at the tidal boundary that were used to obtain the model results in Figure 4.8 through Figure 4.10 and Figure 4.12 through Figure 4.14 and resulted in a maximum tide height (in CGVD28) of 9.6 m at high tide during Tide 2. Water levels at the tidal boundary were then manually increased by 5 cm for each successive model. The last of the five models in this sequence simulated a maximum tide height of 9.8 m.

Figure 4.18 illustrated the maximum flood extent within the restoration site by plotting water depth at high tide during Tide 2 with a maximum tide height of 9.6 m (in CGVD28). The black lines are the existing dykes and the open spaces between them (four in total) on the northern side of the two rivers represent the portions of the dyke that have

been removed (breaches). The red lines drawn within the restoration site represent the locations of the two new (proposed) dykes, as illustrated in the final managed realignment design (Figure 2.2). It is important to note that, along with newly constructed borrow pits and excavated channels within the restoration site, the proposed dykes did not exist in the 2018 DEM. They are only shown in the following figures to remind the reader of their locations and to assist in the analysis of the model results by visualizing where they are with respect to the furthest floodwater extent.

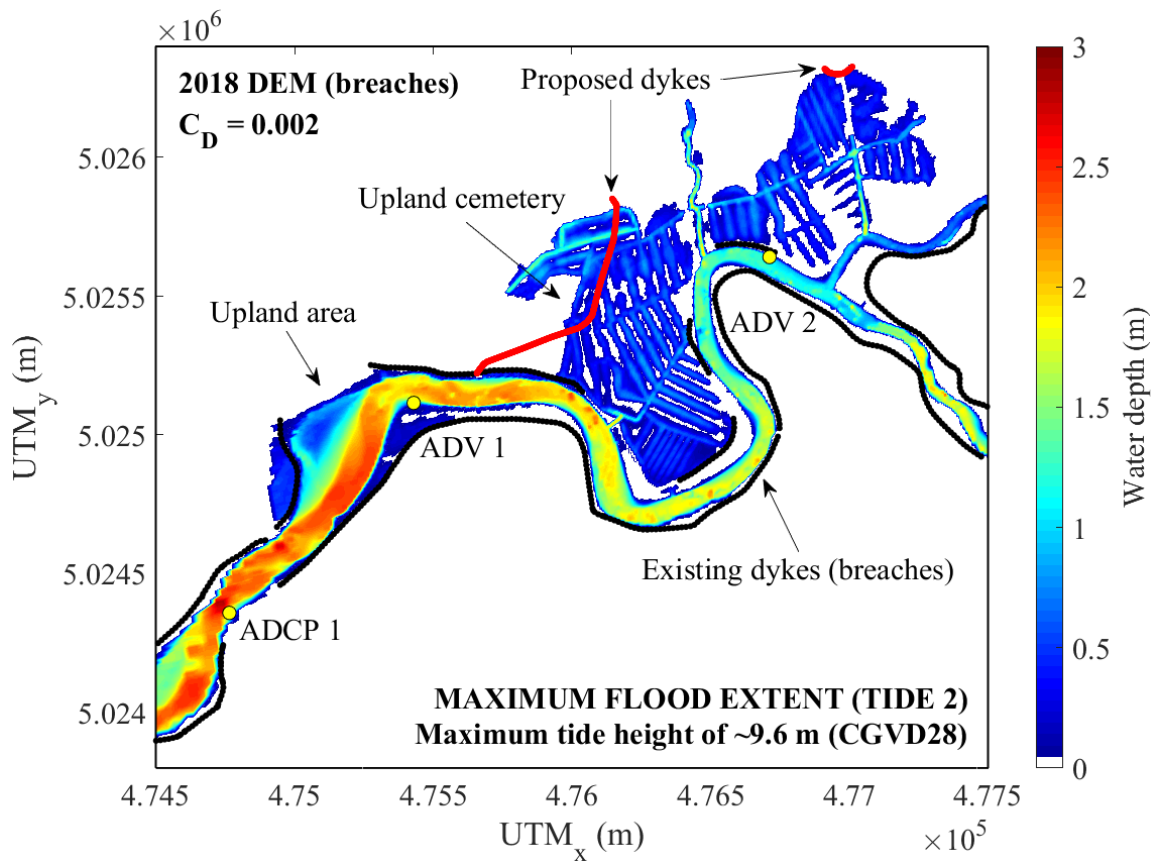


Figure 4.18. Modelled water depths with a maximum tide height of 9.6 m (in CGVD28) at the approximate time of high tide during Tide 2.

According to the model results in Figure 4.18, the tidal water that flowed upstream in the Salmon River Estuary on the morning of August 13, 2018, would have flooded the restoration site if the dykes had been breached at the time of Tide 2. The model simulated water flowing into the restoration site at three out of the four breach sites through old excavated channels that exist at the locations of the removed aboteaux. The floodwater then spread throughout the restoration site by flowing along the old agricultural ditches (visible in Figure 4.18) and McCurdy Brook, which flows in a north-south direction and is located just downstream of where ADV 2 + OBS 2 was deployed. The most critical finding was that the floodwater remained within the boundaries of the designated restoration site, except for at one location: around the northern boundary of the upland cemetery. It was a critical finding because the model predicted flooding at depths of around 1 m on the gravel road north of the cemetery, which was behind one of the proposed dykes. This reinforced the decision to build a dyke at that location in order to protect the cemetery, and its roads, from future flooding and potential erosion.

Figure 4.19, Figure 4.20, Figure 4.21 and Figure 4.22 below illustrated the maximum flood extent within the restoration site with a maximum tide height of 9.65 m, 9.7 m, 9.75 m and 9.8 m, respectively. All parameters in each model, other than the initial water levels at the tidal boundary, were the same.

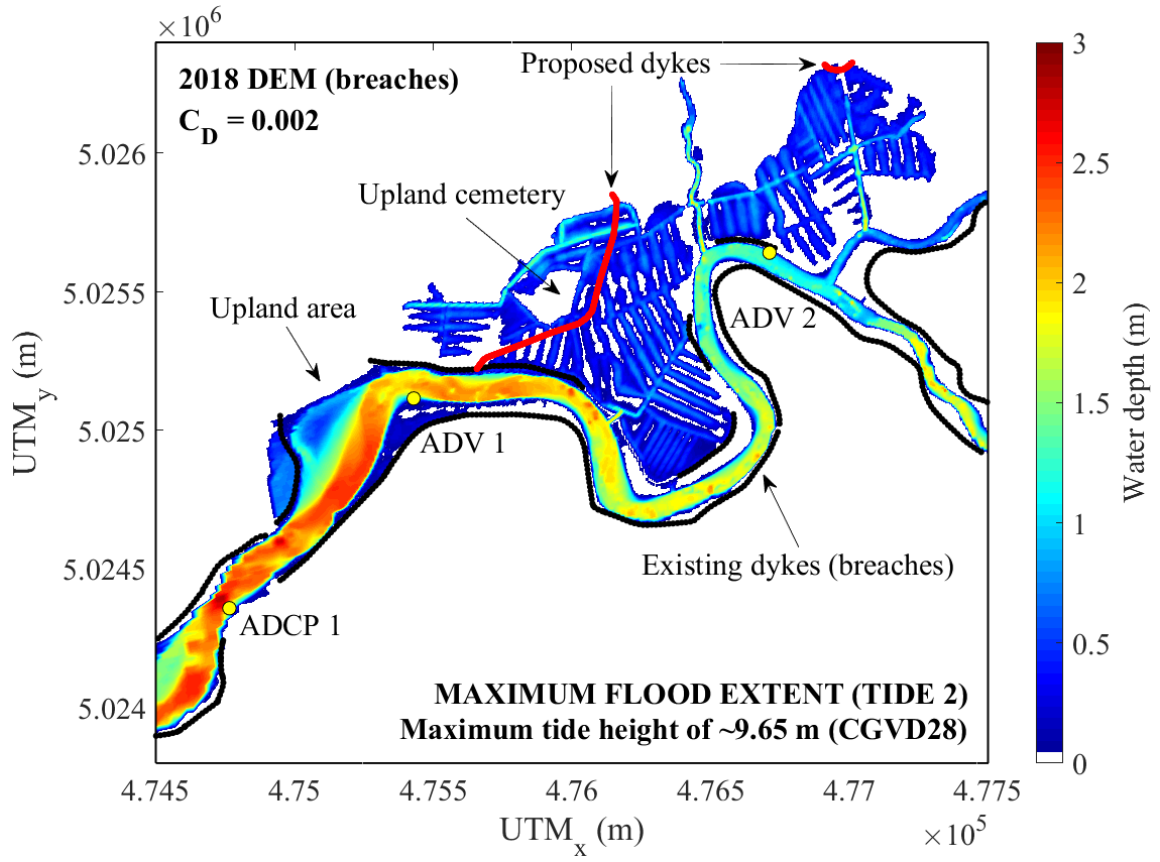


Figure 4.19. Modelled water depths with a maximum tide height of 9.65 m (in CGVD28) at the approximate time of high tide during Tide 2.

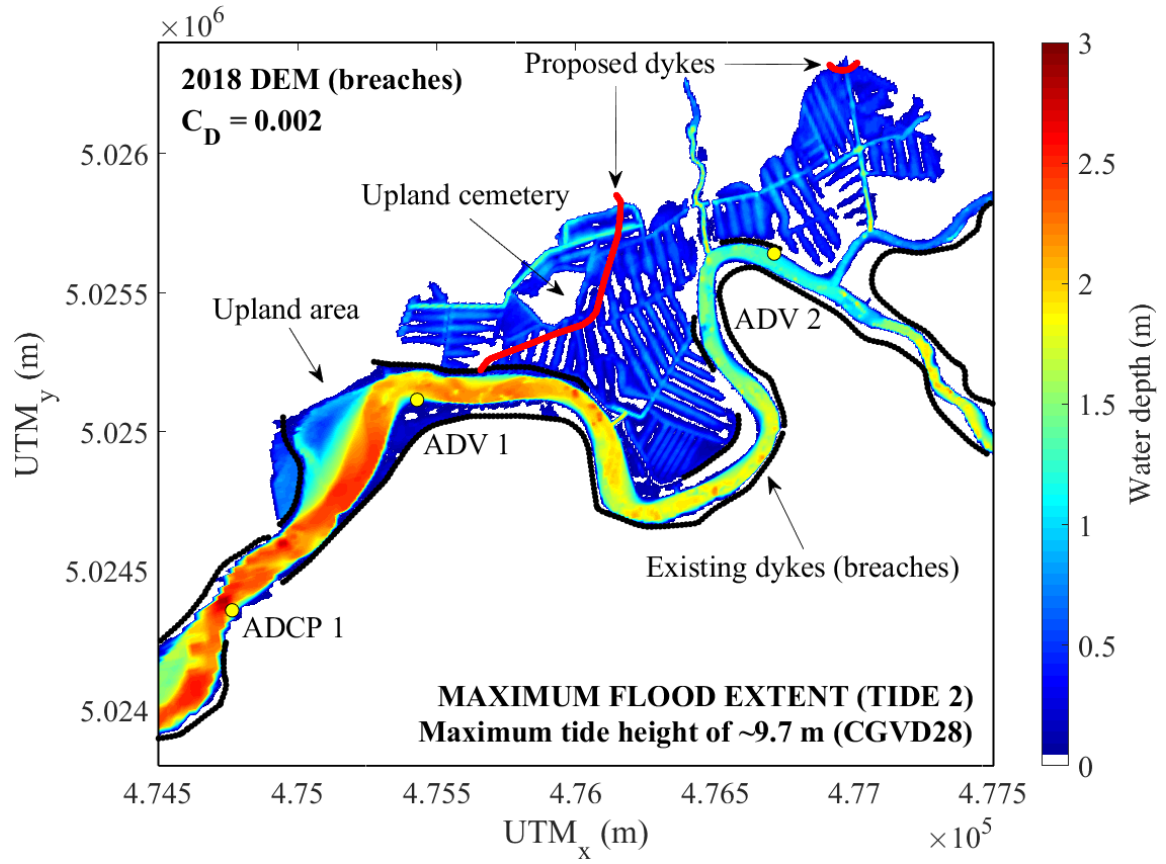


Figure 4.20. Modelled water depths with a maximum tide height of 9.7 m (in CGVD28) at the approximate time of high tide during Tide 2.

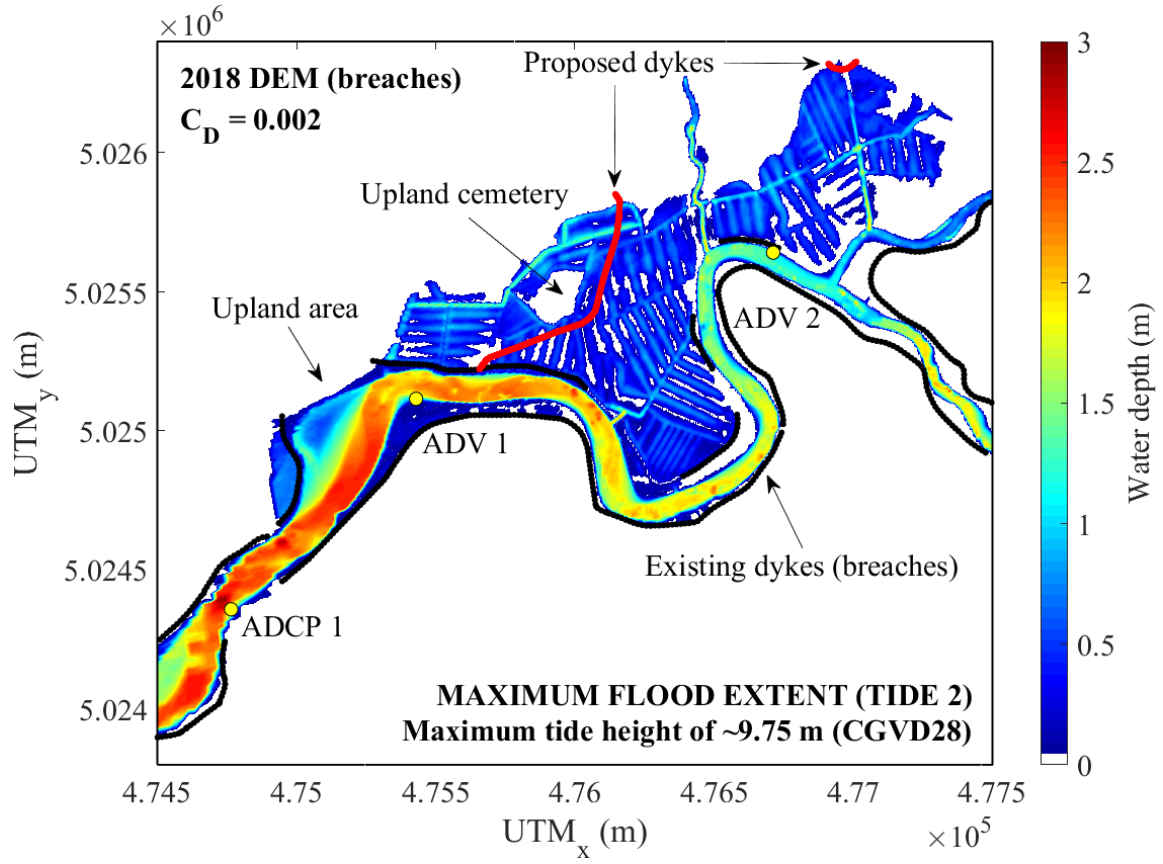


Figure 4.21. Modelled water depths with a maximum tide height of 9.75 m (in CGVD28) at the approximate time of high tide during Tide 2.

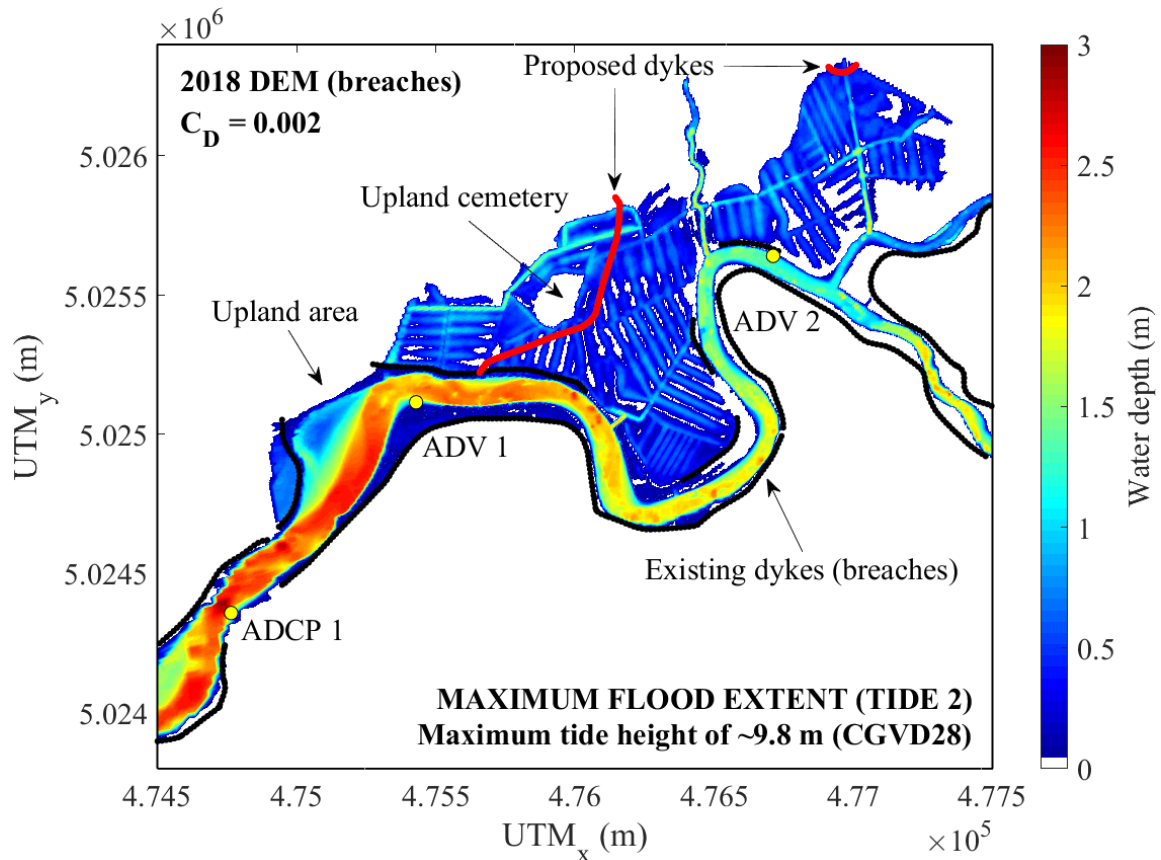


Figure 4.22. Modelled water depths with a maximum tide height of 9.8 m (in CGVD28) at the approximate time of high tide during Tide 2.

The general trend illustrated in Figure 4.18 through Figure 4.22 was that flooding and maximum flood extent increased with increasing water levels, which was expected. As water levels increased, water depths in the agricultural ditches increased and started filling in the white spaces (areas not flooded) in between. There was even some flooding after the first 5-cm increment (Figure 4.19) behind the proposed dyke northeast of ADV 2, which will also be the location of a newly constructed aboiteau to allow for freshwater drainage at low tide. Again, the most significant finding was the extensive flooding around the cemetery behind the proposed dykes, west of ADV 2. After only the first 5-cm water level increment (Figure 4.19), floodwater completely surrounded the cemetery and

occupied the gravel roads nearby, blocking access to the cemetery. Figure 4.22 was the worst-case scenario simulated for this research, which showed a large decrease in white space within the boundaries of the maximum flood extent. The total water level increase between Figure 4.18 and Figure 4.22 is 20 cm, which may represent a water level increase from a storm surge, sea level rise or even higher spring tides than those studied for this research.

The results shown in Figure 4.18 through Figure 4.22 strongly supported the application of a hydrodynamic model, such as Delft3D, throughout the stages of a managed realignment project, especially prior to new inland dyke construction and breaching of the existing dyke infrastructure. Delft3D was able to predict possible flood scenarios and would be beneficial to use even prior to designing where the new dykes should be located. In the case of the Onslow-North River restoration site, the preliminary models simulated in 2017 provided enough information to anticipate where flooding may occur, and therefore, assisted in the design of the managed realignment of dykes. Fortunately, the locations of the two proposed dykes in the design, which have already been constructed at the site, are suitable and the need for them is supported by the results presented here.

4.2.3. Spatial Distribution of Modelled Currents at the Restoration Site

Predictions of maximum flood extent for different water levels are critical for planning managed realignment, but to predict how the restoration site will develop over time, one must also analyze the currents simulated within the restoration site over a tidal cycle.

Figure 4.23 through Figure 4.26 illustrated the modelled flood extent of tidal water within

the restoration site throughout the duration of Tide 2, along with modelled water currents. They showed results 40 minutes before high tide, 10 minutes before high tide, 20 minutes after high tide and 140 minutes after high tide, and were simulated using the 2018 DEM and a bottom friction coefficient of 0.002. The purpose of this was to identify the spatial distribution of moving water in the rivers and the restoration site to predict the movement and potential deposition of sediment. It is important to note that sediment transport was not modelled as part of this research, but the modelled velocities can help predict possible sediment transport patterns.

The maximum limit of the colour bars in Figure 4.23(a) and (b) were chosen to be 3 m and 2 m/s, respectively, to see a stronger contrast between water depths and velocities within the restoration site as they were much lower than those in the river channels. Some of the simulated depths and velocities exceeded 3 m and 2 m/s (primarily in the river channels), respectively, but the main focus was on the restoration site.

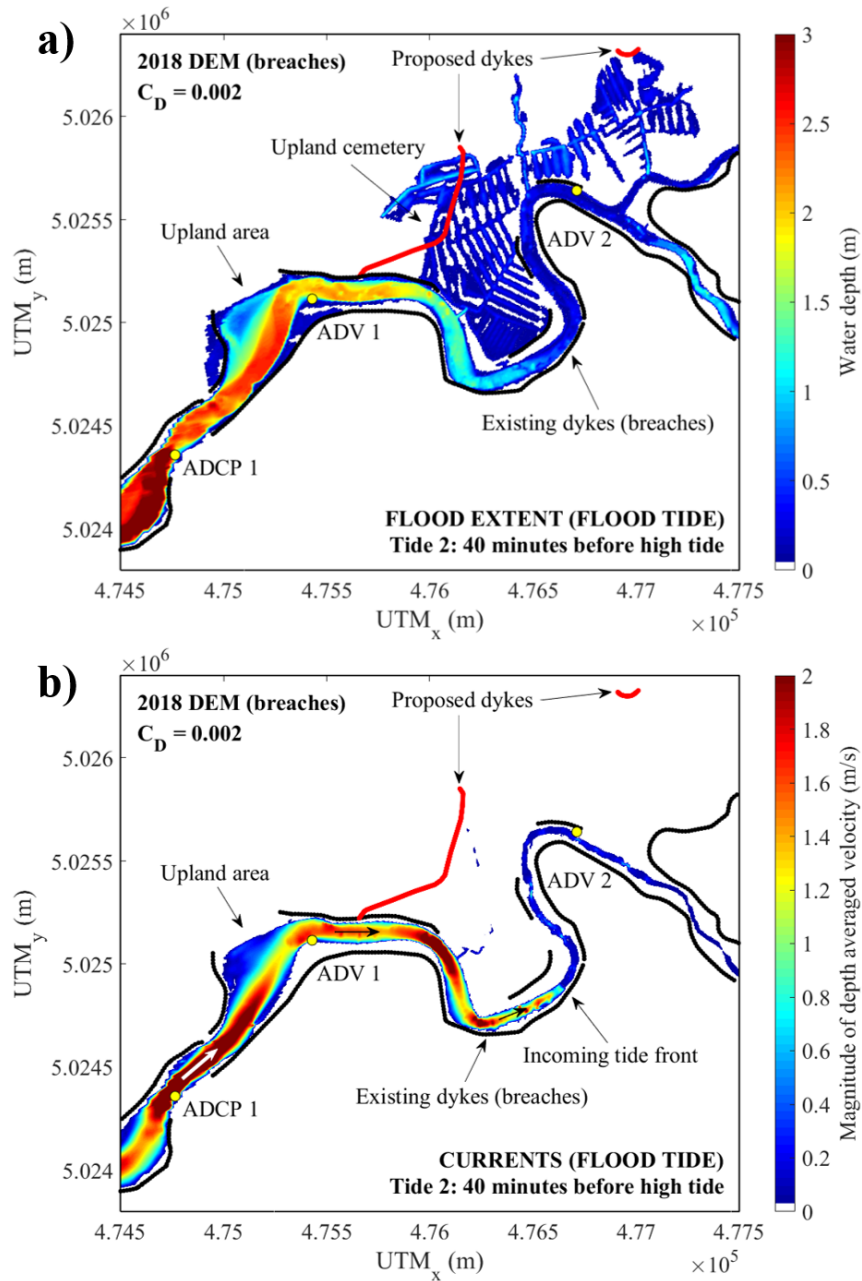


Figure 4.23. Modelled water depths (a) and magnitude of depth averaged velocities (b) with a maximum tide height of 9.6 m (in CGVD28). Model results are for Tide 2 and are shown 40 minutes before high tide. Arrows show the direction of flow.

Figure 4.23(a) showed the simulated flood extent 40 minutes before high tide for Tide 2 and Figure 4.23(b) showed the simulated velocities for the same model time step. At 40 minutes before high tide, the incoming tide front was visible because of the steep

velocity gradient in the Salmon River shown in Figure 4.23(b). The tidal water following the incoming tide front was moving fast, with modelled velocities exceeding 2 m/s, especially around the meander bends and the channel constriction at the location of ADCP 1. The arrows in the channels indicated an upstream flow direction. At this time, there was almost no movement of water within the restoration site, yet Figure 4.23(a) showed quite a bit of flooding. This is because the slow-moving or stagnant floodwater within the restoration site came from previous tides, indicating that water drained slowly from the restoration site in between tides, that there are pools of floodwater within the restoration site that never drained, or a combination of both.

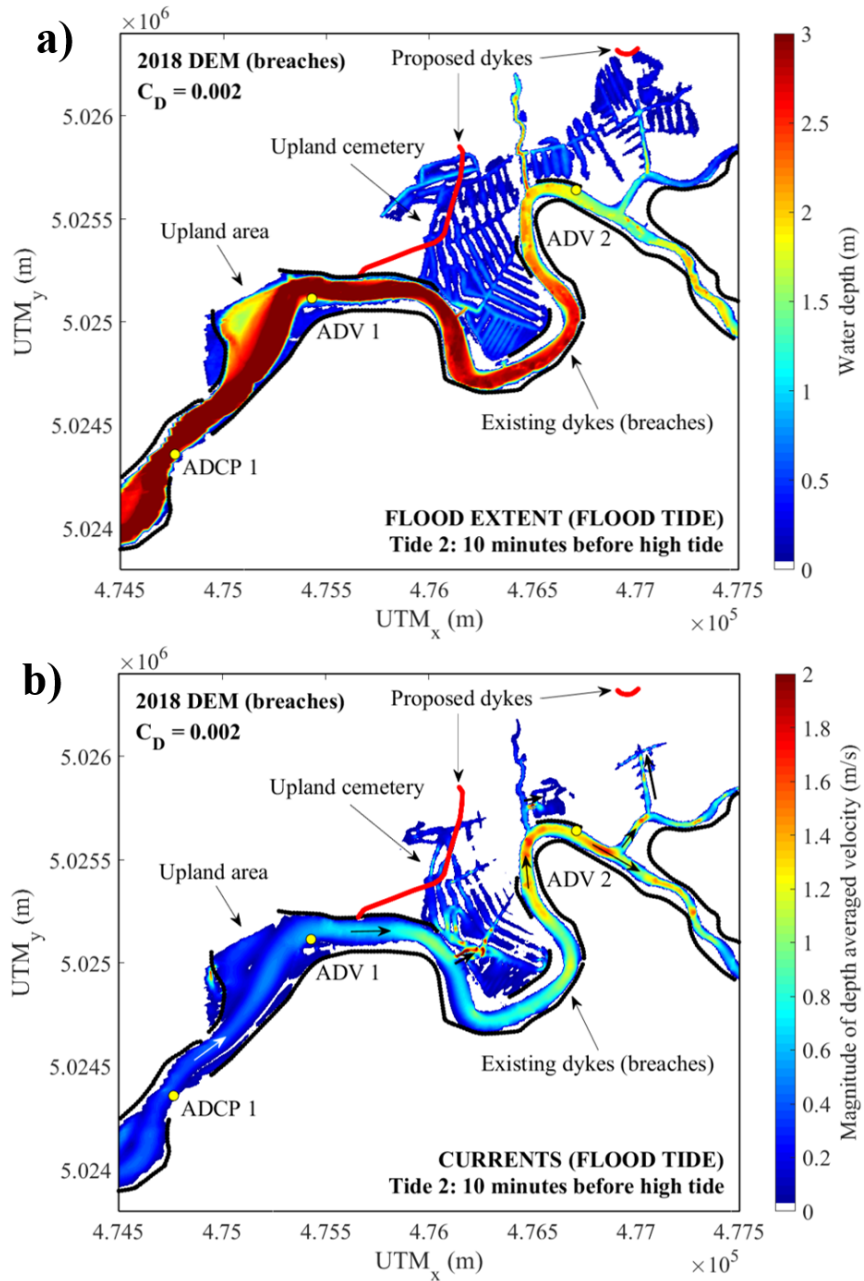


Figure 4.24. Modelled water depths (a) and magnitude of depth averaged velocities (b) with a maximum tide height of 9.6 m (in CGVD28). Model results are for Tide 2 and are shown 10 minutes before high tide. Arrows show the direction of flow.

In Figure 4.24(a), 10 minutes before high tide, the flood extent within the restoration site did not expand much from what it was 30 minutes prior, but water depth did increase, especially in McCurdy Brook and the two other channels leading into the

restoration site at the first and fourth dyke breaches (from left to right). The majority of the Salmon River exhibited modelled water depths that exceeded 3 m, and at this point in time, the water line was at an elevation where tidal water could quickly pour into the restoration site, as illustrated in Figure 4.24(b). A large portion of the floodwater already within the restoration site was stagnant, which was most notable in the northeast by the small proposed dyke, but velocities at and near the breach locations were high (exceeding 1.6 m/s in some ditches) 10 minutes before high tide compared to velocities simulated for the other 30-minute time step intervals. Lastly, because it was nearing high tide, velocities in the rivers decreased.

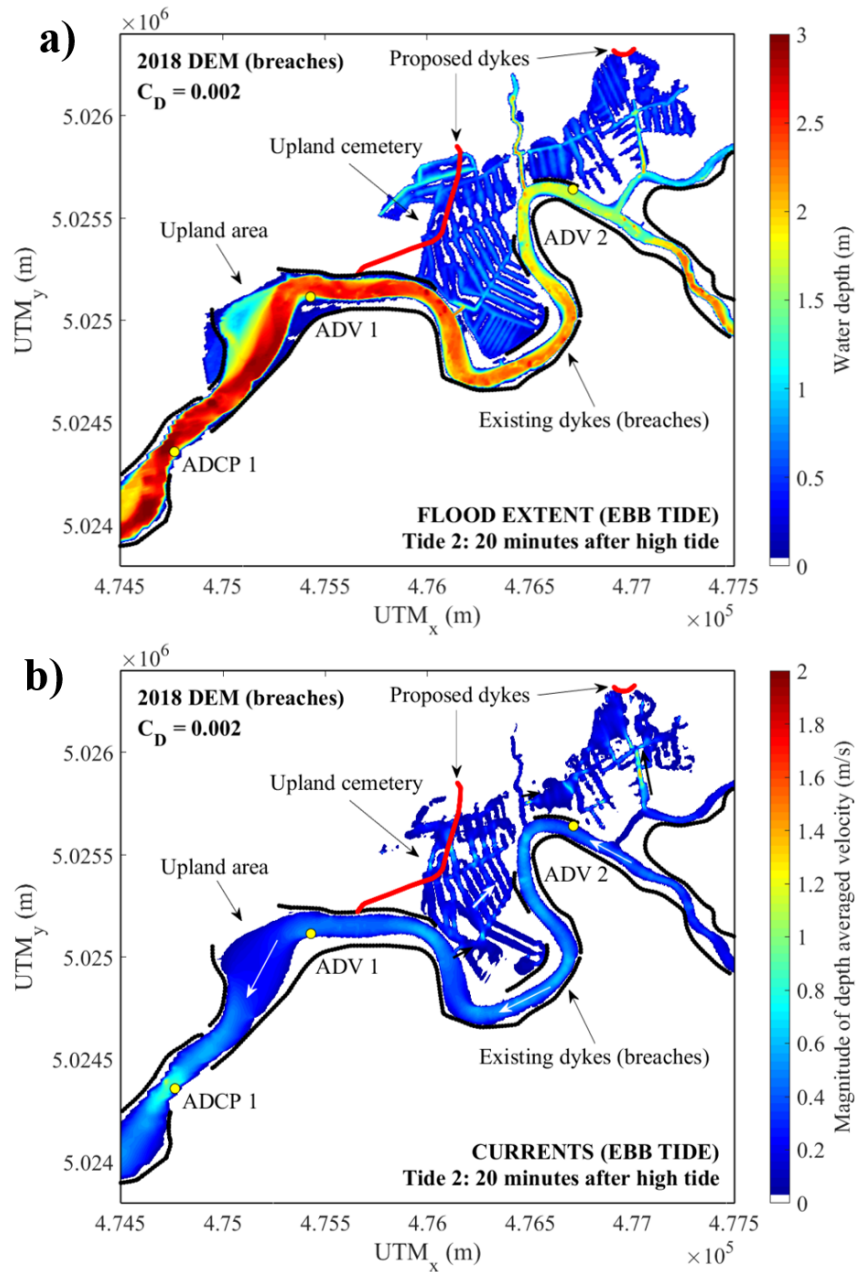


Figure 4.25. Modelled water depths (a) and magnitude of depth averaged velocities (b) with a maximum tide height of 9.6 m (in CGVD28). Model results are for Tide 2 and are shown 20 minutes after high tide. Arrows show the direction of flow.

In Figure 4.25(b), 20 minutes after high tide, more water within the restoration site was moving, but at a much slower speed in most areas (< 0.8 m/s). The most interesting finding was that even though this result was simulated for 20 minutes after high tide, the

water within the restoration site had not yet reached its maximum flood extent for Tide 2. Although the water in the two rivers was flowing downstream towards the Bay of Fundy, the water line was still high enough for water to flow through the dyke breaches into the restoration site. Flow direction was depicted by arrows in Figure 4.25(b).

Results for the next 30-minute model time step, 50 minutes after high tide, are found in Appendix I and showed the maximum flood extent for Tide 2. Model results at 80 minutes and 110 minutes after high tide are also found in Appendix I. The difference in results between these three model time steps were minimal. Over the course of 90 minutes, water depths in the two river channels decreased as the tide ebbed and floodwater slowly drained from the restoration site, with minimal change in flood extent.

Figure 4.30 showed the model results for the last 30-minute time step interval chosen for analysis. Flood extent and currents were simulated 140 minutes (> 2 hours) after high tide for Tide 2.

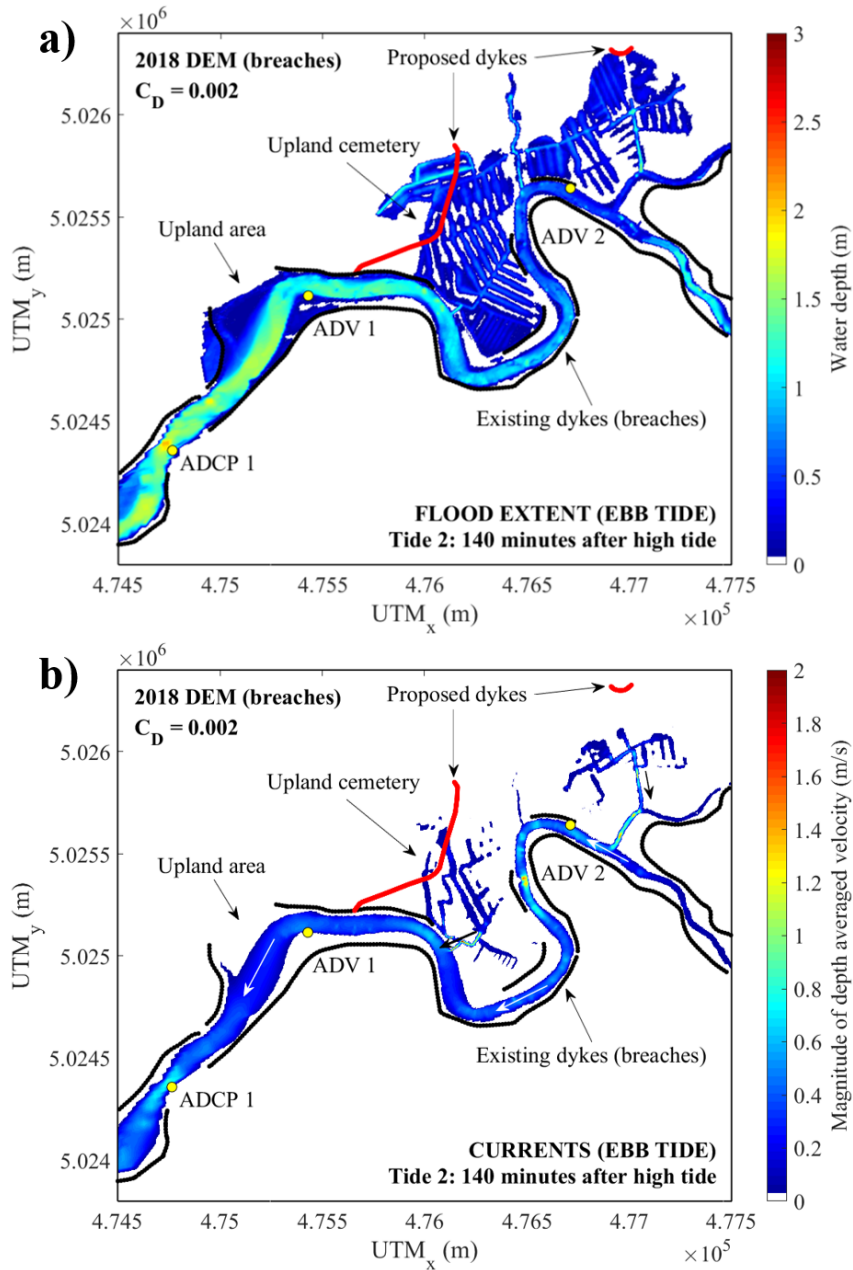


Figure 4.26. Modelled water depths (a) and magnitude of depth averaged velocities (b) with a maximum tide height of 9.6 m (in CGVD28). Model results are for Tide 2 and are shown 140 minutes after high tide. Arrows show the direction of flow.

In Figure 4.26(a), 140 minutes after high tide, the modelled flood extent remained nearly the same as in Figure 4.25(a), but water depths throughout the restoration site decreased, most notably in McCurdy Brook and the larger agricultural ditches. The amount of water

movement within the restoration site had also decreased, however, water was still slowly draining approximately 2 hours after high tide, as shown by the velocity map and flow direction arrows in Figure 4.26(b).

In summary, model results of velocity sometimes showed little to no movement of floodwater within the restoration site, but it did not mean there was little to no floodwater occupying the restoration site. In between tides, floodwater that did not drain back into the two rivers remained stagnant in the agricultural ditches within the restoration site. Not until the next tide did that floodwater start to circulate again in response to the energy of new floodwater flowing through the dyke breaches into the restoration site (illustrated in Figure 4.24). This indicates that the restoration site has poor hydrologic connectivity in areas with stagnant floodwater. It was also discovered that even after high tide, when the direction of flow in the rivers changed, water was still flowing from the river channels into the restoration site, as long as the water line was high enough to overtop that surface along the river's edge at the breach locations. Additionally, floodwater within the restoration site drained slowly after high tide; slow enough that there was still a large amount of water within the restoration site right up until the tidal bore passed by on the next tide. Lastly, model results suggested the potential for sediment transport in and out of the restoration site based on the high modelled velocities of water flowing in and out of the restoration site.

4.2.4. Flood Statistics for the Restoration Site

This section revisits the maps of maximum flood extent in Figure 4.18 through Figure 4.22, but includes calculations of flood volume, flood area, average water depth and

maximum water depth in the areas behind the breached dykes for each maximum tide height scenario (Figure 4.27, Figure 4.28 and those in Appendix J). It is important to note that these calculations were not limited to the boundaries of the restoration site because flooding did occur in the model behind both proposed dykes (not included in the 2018 DEM), which was outside of the restoration site illustrated in Figure 2.2. The model results within the main channels of the Salmon River and North River were not included in these calculations.

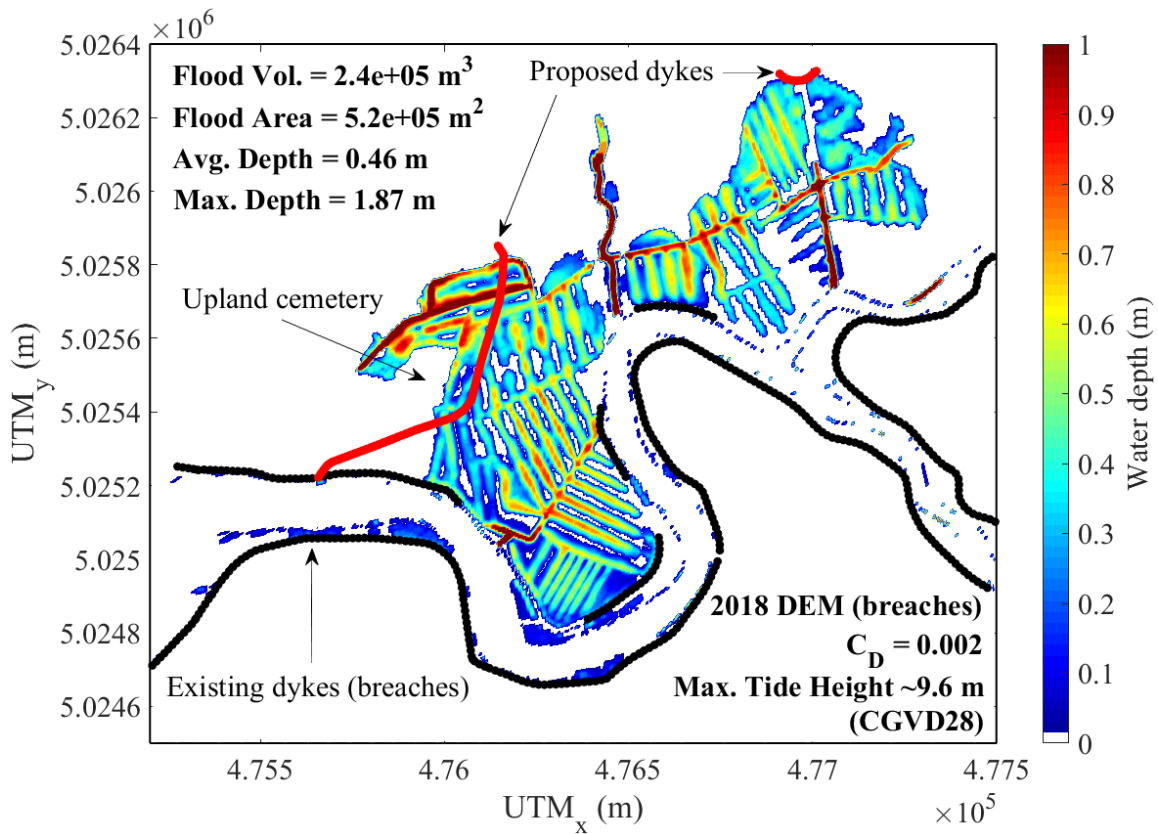


Figure 4.27. Modelled water depths with calculated flood volume, flood area, average water depth and maximum water depth values within the restoration site at the approximate time of high tide for Tide 2. Maximum tide height at high tide was 9.6 m (in CGVD28).

Figure 4.27 showed identical results to those in Figure 4.18 except it showed no water in the main river channels and the maximum water depth for the range of the colour bar was 1 m instead of 3 m (to show a better contrast between water depth values). For this scenario, with a maximum tide height of 9.6 m, the flood volume, flood area, average water depth and maximum water depth based on model simulations were $2.4 \times 10^5 \text{ m}^3$, $5.2 \times 10^5 \text{ m}^2$, 0.46 m and 1.87 m, respectively. A flood area of $5.2 \times 10^5 \text{ m}^2$ is equal to 52 hectares, and the restoration site is 92 hectares, therefore, tidal water could potentially inundate 56.5% of the restoration site on a tide similar to Tide 2. However, the calculated flood area included the floodwater outside of the boundaries of the restoration site (i.e., behind the proposed dykes), so this percent flood cover is most likely different than what it would be if the proposed dykes were included in the 2018 DEM. The problem with producing a more representative percent flood cover without updating the 2018 DEM and re-running the model is that the areas in which the floodwater would be diverted by the proposed dykes (the larger one in particular) are unknown. Appendix J contains the model results for the next three 5-cm water level increments (9.65 m, 9.7 m and 9.75 m).

Figure 4.28 illustrated the maximum flood extent by plotting water depth within the restoration site at high tide during Tide 2 with a maximum tide height of 9.8 m (in CGVD28). Calculated values of flood volume, flood area, average water depth and maximum water depth within the restoration site, and behind the proposed dykes, were included.

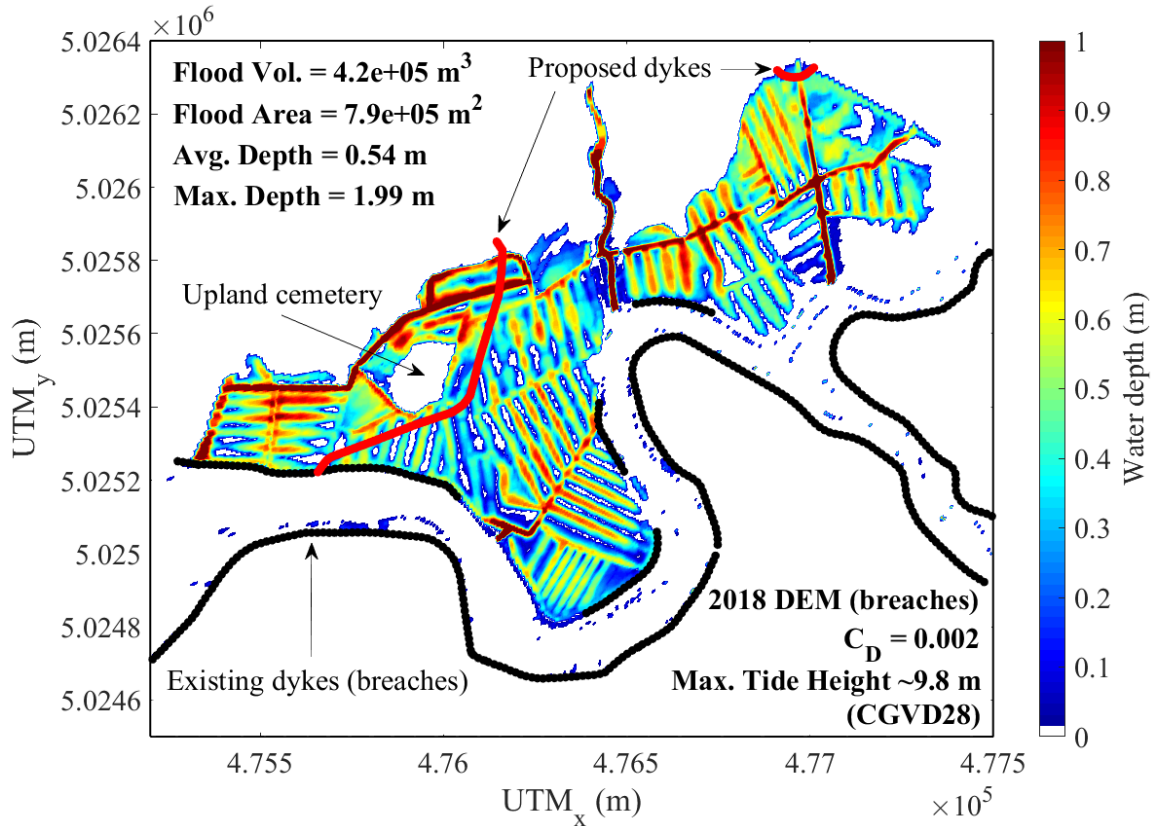


Figure 4.28. Modelled water depths with calculated flood volume, flood area, average water depth and maximum water depth values within the restoration site at the approximate time of high tide for Tide 2. Maximum tide height at high tide was 9.8 m (in CGVD28).

Figure 4.28 illustrated identical results to those in Figure 4.22, except it showed no water in the main river channels and the maximum water depth for the range of the colour bar was 1 m instead of 3 m. For this scenario, with a maximum tide height of 9.8 m, the flood volume, flood area, average water depth and maximum water depth based on model simulations were $4.2 \times 10^5 \text{ m}^3$, $7.9 \times 10^5 \text{ m}^2$, 0.54 m and 1.99 m, respectively. A flood area of $7.9 \times 10^5 \text{ m}^2$ is equal to 79 hectares, and the restoration site is 92 hectares, therefore, tidal water could potentially inundate 85.9% of the restoration site during a tide with water levels 20 cm higher, at high tide, than Tide 2. Again, this model simulated

flooding behind the proposed dykes outside of the boundaries of the restoration site, therefore, a more representative percent flood cover within the boundaries of the restoration site for this scenario can be predicted only by updating the 2018 DEM (raising the surface elevation where the proposed dykes are located in the managed realignment design) and re-running the model.

At this location within the Salmon River Estuary, Delft3D models predicted that a 20-cm increase in water levels at the tidal boundary would result in an increase in flood area by almost 30%. A summary of these findings can be found in Figure 4.29. These findings are useful for continued management of this project, are something to keep in mind when monitoring the site after the existing dykes have been breached and can be used as a reference for future managed realignment sites within the Salmon River Estuary.

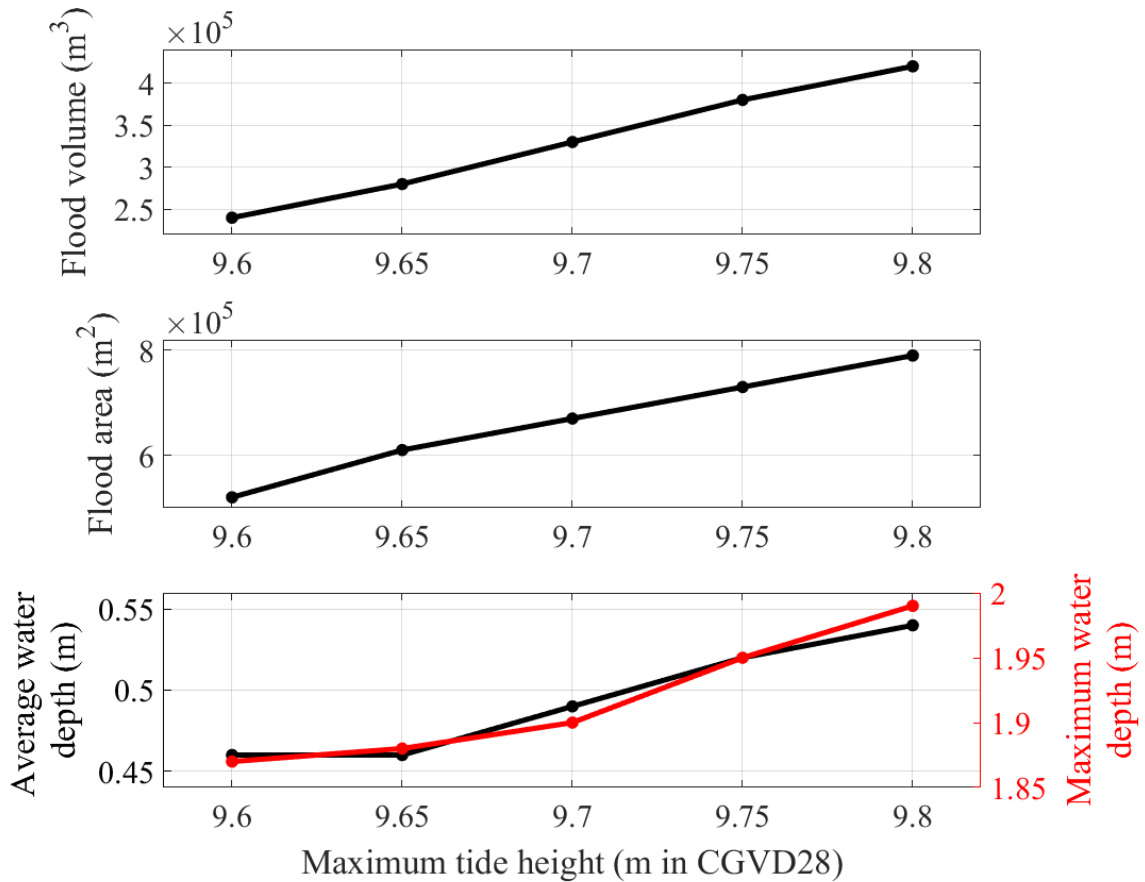


Figure 4.29. Flood volume, flood area, average water depth and maximum water depth at the managed realignment site for each 5-cm increment in maximum tide height. A bottom friction coefficient of 0.002 was selected for these models, the 2018 DEM was used and the results shown are those simulated for Tide 2 at the approximate time of high tide. Maximum tide height is in CGVD28. Note the difference in scale for the two axes in the bottom panel.

The general pattern shown in Figure 4.29, for all three panels, was that all four calculated variables increased with an increase in maximum tide height. A closer look at the slopes in the line plots provided insight into how tidal water propagated through and filled the restoration site. Changes in flood volume for each 5-cm water level increment were relatively consistent, but the flood area, average water depth and maximum water depth lines can be divided into two sections based on two different line slopes. The first section

is from a maximum tide height of 9.6 m to 9.65 m and the second section is from a maximum tide height of 9.65 m to 9.8 m. In the second section of the lines for flood area and the two water depth variables, the slopes were relatively consistent and similar to one another. However, in the first section, the flood area slope differed slightly from the two water depth slopes. The greatest increase in flood area, for all five models, occurred after the first 5-cm water level increment, yet the two water depth variables did not change much, if at all. This indicated that when tidal water entered the restoration site, it spread out first, and then, when it could not spread any further, water depths began to increase as more water was added to the system (via increases in water levels at the tidal boundary). The threshold at which this phenomenon occurred at this restoration site existed somewhere between a maximum tide height of 9.6 m and 9.65 m.

4.2.5. Water Levels Before and After Breaching the Dykes

This last section investigates whether managed dyke realignment at the Onslow-North River restoration site will mitigate/reduce flooding in Truro, according to model results. Figure 4.30 showed modelled water levels (in CGVD28) at five different locations in the Salmon River for the scenario with no breaches and the scenario with breaches to identify the difference the breaches made in water levels in the main river channel. The five locations were labelled Point A to Point E and are illustrated in Figure 4.31 along with the average change in water level over the four simulated tides for each location. Water level changes in the North River were not plotted or analyzed because the model grid covering this narrow river was much coarser upstream of the restoration site and did not resolve the river channel very well.

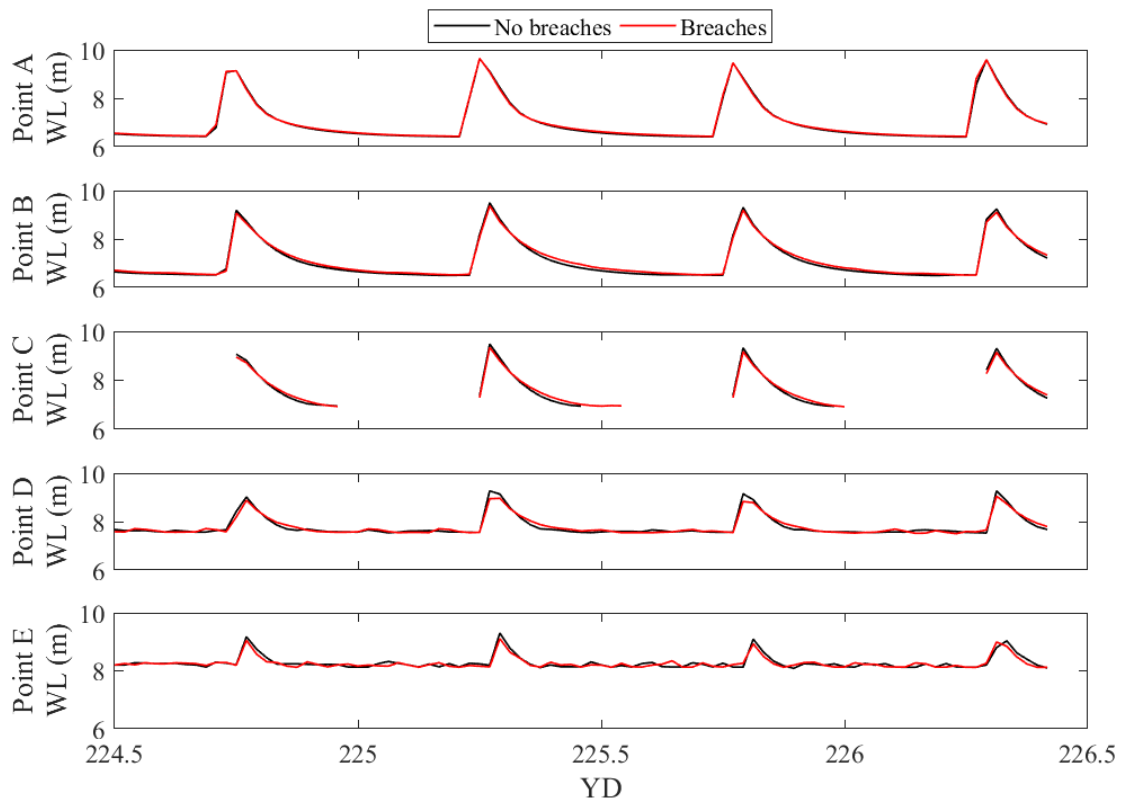


Figure 4.30. Modelled water levels (in CGVD28) at five different locations throughout the Salmon River over four spring tides. The black line represents the results of the no-breach scenario and the red line represents the results of the breach scenario. The two variations of the 2018 DEM were used for these simulations and a bottom friction coefficient of 0.002 was used for both model runs.

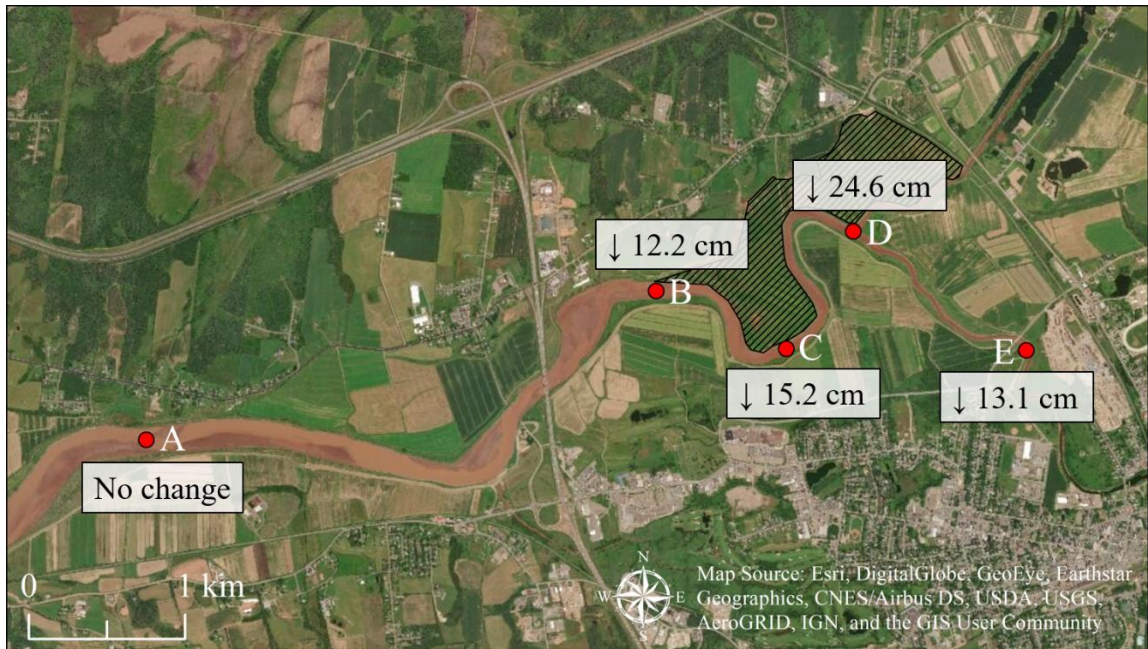


Figure 4.31. Approximate locations of points selected to compare water levels simulated for the non-breach scenario and the breach scenario. Average changes in water level over all four simulated tides are also included. The hatched area is the restoration site.

Overall, water levels decreased at four of the five locations after the dykes were breached. The only location in the river channel where modelled water level did not change was Point A, which was located 6.5 km downstream of the restoration site. This made sense because changes in any variable would only occur at locations adjacent to or upstream of the dyke breaches. Results at Points B, C, D and E showed a decrease in water level. The smallest decrease in water level was modelled at Point E (4.5 cm) and the largest decrease in water level was modelled at Point D (31.9 cm). The findings from Figure 4.30 and Figure 4.31 suggested that water levels would decrease throughout the main river channels once the dykes have been breached, but only at and upstream of the restoration site. With lower water levels there is a decreased risk of flooding, therefore,

managed dyke realignment at this restoration site in the inner Salmon River Estuary may reduce the amount and/or frequency of flooding in the town of Truro, Nova Scotia.

The detailed model results described in this chapter clearly illustrated and quantified the hydrodynamics of flooding at the Onslow-North River restoration site for the future scenario with breached dykes. On a larger scale, these datasets and this approach could be used to justify the decision to implement additional managed realignment of dykes within the inner Salmon River Estuary adjacent to Truro to further reduce the flood risk. They can also be used to support other coastal communities in their efforts to develop climate change adaptation strategies.

Chapter 5 – Discussion

The purpose of this research was to better understand the dynamics of the Salmon River Estuary, to set up and calibrate a hydrodynamic model that can reproduce tidal river conditions (i.e., water levels and velocities) and to investigate the potential impact of managed dyke realignment on flooding at the restoration site in Truro. Field measurements were collected and the model was used to examine the response of the system to small, realistic changes in bathymetric parameters (i.e., the bathymetry and the bottom friction coefficient) and to predict future flood scenarios at the restoration site. These scenarios corresponded to the prediction of flood extent and spatial distribution of velocities, in and near the restoration site, after changing the model bathymetry by breaching the dyke and exposing a portion of the floodplain to tidal and river water. Lastly, the model was used to determine the change in water levels, within the main river channel, after breaching the dykes in the model bathymetry. The model provided detailed results that permit a discussion of management implications and considerations for future realignment projects.

5.1. Delft3D was successful at simulating hydrodynamic conditions in the Salmon River Estuary and simulated minor differences from making realistic changes in bathymetry and bottom roughness

The model results led to key findings that indicated Delft3D was successfully applied and was able to reproduce the hydrodynamics in the Salmon River Estuary. Modifying bathymetry and bottom roughness, within realistic ranges, simulated a maximum phase difference of 15 minutes between the two modelled results and resulted in similar water

level and velocity profiles. This implied that the digital elevation model (DEM) used to define the bathymetric input in the Delft3D model does not need to be constantly updated over time and that the default bottom friction coefficient results in simulations that matched well with observations. The two sets of modelled water levels and velocities also exhibited differences after changing these two parameters. Water levels increased by an average of 30 cm at high tide after decreasing bottom roughness. At the beginning of the flood tides, velocities increased by an average of 2.07 m/s, but only at ADCP 1. At the time velocities peaked during the ebb tides, velocities increased by an average of 0.62 m/s and by an average of 0.51 m/s at ADCP 1 and ADV 1 + OBS 1, respectively. The model did occasionally simulate velocities that increased by up to 3.2 m/s, but only at the very beginning of the flood tides at ADCP 1. Otherwise, the modelled velocities were similar. In general, changing the DEM from the 2018 DEM (no breaches) to the 2014 DEM resulted in lower velocities at the beginning of the flood tides that better matched the measured velocities, particularly at the location of ADCP 1. Changing the bottom friction coefficient from 0.002 to 0.001 resulted in higher peak water levels and higher peak velocities on the ebb tides throughout the study area, higher velocities at the beginning of the flood tides at ADCP 1 and a phase shift illustrating the earlier arrival of the tides in the study area.

It is important to note that although the change in bottom roughness was relatively small and the majority of elevation changes between the 2013 DEM and 2018 DEM were minor (except along the channel banks), there were areas within the river channel that showed large changes in elevation (> 1 m) between the 2013 DEM and 2018 DEM. Even so, the bulk changes in water levels and velocities were minimal after changing the DEM.

Although the results of this research apply to a specific site in a macrotidal estuary, the outcomes are applicable to other sites around the world. For example, the Severn Estuary in the UK has a large tidal range (approaching 14 m during spring tides), similar to the Salmon River Estuary (Xia et al., 2010). The difference between the Salmon River Estuary and the Severn Estuary is that the latter has been studied extensively and is well-understood (Xia et al., 2010).

In terms of managed realignment, hydrodynamic models have been successfully applied to predict the response of an estuary to managed realignment and to investigate the model's response to small, realistic changes in model parameters. For example, a study by Kiesel et al. (2020) used Delft3D-FLOW to analyze the effects of six different designs at a managed realignment site in the UK on high water level attenuation. They tested a range of values representing bottom roughness (Manning's n coefficient for saltmarshes, $n = 0.035-0.09$) and determined the model was not sensitive to these variations, similarly to the findings of the present research. In addition, model validation with field measurements confirmed that simulated water depths were accurate and that a maximum phase shift of 20 minutes existed for changes in the drag coefficient (Kiesel et al., 2020), a value that is very similar to the finding in the present research. In another study, Symonds et al. (2016) confirmed that Delft3D, and two other models (Mike21-FM and Delft3D-FM), were successful at accurately predicting hydrodynamic conditions in complex estuarine regions.

It is important to comment on the differences between a hydrodynamic model and a standard GIS bathtub model in estimating flooding. Bathtub models are useful for providing quick, general ideas of the flood extent at a restoration site, however, a

hydrodynamic model that includes physics-based computations of fluid processes provides significantly more insight into the flooding response of an estuarine system. Additionally, hydrodynamic models simulate flow velocities for every flooded cell in the model domain, can be used to simulate flooding and drying and has the potential to simulate sediment transport and changes in morphology. Although bathtub models can provide near-instantaneous results to make management decisions, hydrodynamic models should be applied for a detailed understanding of hydrodynamic processes and can include other phenomena (e.g., sediment transport patterns, sedimentation and erosion and spatial patterns of vegetation). Overall, hydrodynamic models can provide detailed insight as indicated by the successful simulating of tidal conditions in complex estuarine systems, such as the Salmon River Estuary in the present research.

5.2. Detailed hydrodynamic modelling of a macrotidal estuarine system requires detailed field measurements to validate and increase confidence in model results

Hydrodynamic models are useful tools that can provide insight into the behaviour of tidal estuaries, however, detailed field measurements are required for validation. In the case of the managed realignment project in Truro, field observations significantly added to the confidence in the model results. This is very important since the results could have a strong influence on how managed realignment will proceed and will help prepare for possible future outcomes.

Field measurements collected for this research supported the assumption that the inner Salmon River Estuary is dynamic (in terms of bed morphology) and powerful (in terms of currents). At one location, measured suspended sediment concentrations were

upwards of 350 g/L (i.e., fluid mud) and changes in river bed elevation between 2013 and 2018 were found to be greater than 1 m at different locations throughout the study area. In terms of currents, measured velocities in the main river channel reached up to 3 m/s and a high amount of turbulence was observed. The Severn Estuary, the Taf Estuary and the Parret Estuary in the UK are similar to the Salmon River Estuary in that they have large tidal ranges (characterized as macrotidal) and can exhibit complex hydrodynamics with morphology that changes rapidly over very small timescales (Xia et al., 2010; Pontee, 2015; Bennett et al., 2020). For example, measured currents in the Severn Estuary, the Taf Estuary and the Parret Estuary can reach up to 1.8 m/s, 2.2 m/s and upwards of 1.5 m/s, respectively (Xia et al., 2010; Bennett et al., 2020; Pontee, 2015). In terms of suspended sediment concentrations, the Severn Estuary, for example, frequently exceeds 20 g/L (fluid mud) near the bed (Kirby et al., 2004). Modelling estuarine systems such as these is complex and, therefore, must be validated with field measurements.

In this research, the model was less detailed in its selection of parameters and modules as the default option was selected for many of the parameters and neither vegetation nor sediment transport modules were used. However, it was detailed in that the model grid was of high resolution (6 m at the restoration site and 25 m near the boundaries of the model domain) and the high-resolution DEM (1 m in the study area and 5 m throughout the rest of the extended DEM) was updated to represent the morphology of the estuary in the study area at the time field measurements were collected. Regardless, the methods employed resulted in a hydrodynamic model that reproduced the hydrodynamics very well within the study area. Each of the four modelled tides were simulated within 32 minutes of the measured tides, modelled water levels and velocities

illustrated similar profiles to the measured results and modelled peak water levels were within 17.5 cm of measured peak water levels (at high tide) for all four tides. In the Severn Estuary, there exists an extensive repository of field measurements that can and have been used to validate hydrodynamic models (Xia et al., 2010). A study by Xia et al. (2010) validated a hydrodynamic model with field data and used the model to investigate the impacts of a tidal barrage across the estuary. They were able to predict a future scenario using a hydrodynamic model, in which they were confident in because they had field measurements to compare it to, and used the results to make a management decision.

Understanding of and the ability to predict the long-term evolution of a managed realignment site, world-wide, is limited because there is deficient field-based knowledge (French, 2006; Rotman et al., 2008; Esteves and Thomas, 2014; Ni et al., 2014). When hydrodynamic modelling is applied to estuarine systems with limited or no field data to compare to, there is a possibility for large errors, especially in the prediction of optimal breach locations and widths in managed realignment projects (Esteves and Williams, 2017; Friess et al., 2014). One of the lessons learned from this research, which relates to the issues mentioned above in other studies, was that the use of field data in conjunction with hydrodynamic modelling is critical. Therefore, the methods employed for this research can be applied to other complex, macrotidal estuaries around the world to increase confidence in the models being used and to reduce the amount of error in model results.

5.3. Delft3D predicted extensive flooding within the restoration site during high spring tides with simulated currents that suggest the potential for net sediment deposition

One of the main goals of this managed realignment project was to successfully restore tidal wetland habitat at a restoration site in Truro, which depends on two things. The first is seed availability of tidal wetland species in nearby tidal wetlands and, more importantly, the ability of tidal wetland species to reach and colonize the restoration site (Erfanzadeh et al., 2010; Spencer & Harvey, 2012; Wolters et al., 2005; Wolters et al., 2008). The second key requirement for a successful tidal wetland restoration is a sufficient supply of sediment within the restoration site so vegetation can properly establish (Spencer & Harvey, 2012). The sediment layer needs to be deep enough for seeds to embed themselves and grow, but not too deep as excess sedimentation can bury and suffocate the plants. Sedimentation rates that are too high may create an overly soft and unconsolidated surface, preventing the seeds from settling long enough to germinate. Therefore, there must be tidal water flowing in and out of the restoration site over the course of each tidal cycle and currents that keep sedimentation rates within the restoration site at a level that optimize vegetation colonization.

Although sediment transport was not modelled for this research, modelled velocities and water levels reflected conditions conducive to particle settling. The measured results of suspended sediment concentration, calculated from the water samples, confirmed the presence of fluid mud, resulting in high flocculation and the potential for rapid settling as velocities decreased within the study area. For example, water velocities flowing into the restoration site reached up to 2 m/s at the location of the

first breach and 1.4 m/s at the location of the fourth breach (from left to right along the river). At the approximate time of high tide, velocities decreased at these locations. However, once the flow direction in the rivers changed and the floodwater began to drain from the restoration site, velocities at these two locations increased again and were consistently between 0.7 m/s and 1.8 m/s until at least 2 hours after high tide. This spatial and temporal pattern of flow velocity would most likely result in net sediment deposition within the restoration site after a tide similar to Tide 2.

According to the model results presented in this thesis, tidal water inundated a large portion of the restoration site at high tide when water levels were highest. Flooding of the restoration site occurred for all four tides and drained slowly in between tides, indicating that there will always be floodwater within the restoration site, at least during spring tides, and that each tide will bring in a new supply of tidal water. This replenishment of tidal water will help circulate nutrients throughout the restoration site and potentially carry seeds that could germinate in the settled sediment. Modelled velocity results were also promising in that they suggested the potential for net sediment deposition within the restoration site after each tide, at least for the four spring tides in question. Results showed higher velocities of water flowing into the restoration site than flowing out of the restoration site. Since river bed elevations can change so drastically, in either direction, in the Salmon River Estuary near the restoration site, it is expected that there will be tides at different times of the year that erode more sediment from the restoration site on the ebb tide than they deposit on the flood tide, resulting in net sediment erosion or loss. If there was net sediment deposition for every tide of the year, newly deposited seeds or already established vegetation may get buried and die out

(Spencer & Harvey, 2012) and sediment may build up in unwanted locations (i.e., in front of the aboiteau in the proposed northeastern dyke).

In conclusion, Delft3D was able to predict the hydrodynamics within the river and at the restoration site over the course of a tide with model results that made sense based on current, but limited, knowledge of the Salmon River Estuary.

5.4. Modelled water levels in the main river channel decreased in the scenario with dykes breached at the restoration site

This last discussion point, and perhaps the most important one to address, focuses on whether managed realignment at this location in the Salmon River Estuary will reduce flooding in Truro. The key findings of this research were that water levels were a function of where a managed realignment site is within an estuary and that changes in water levels after the barriers are breached were different downstream of the restoration site than they are upstream of the restoration site. Model results showed a decrease in water levels adjacent to and upstream of the restoration site after implementation of managed realignment. This contradicts what Pontee (2015) and French (2006) found in their studies regarding subsequent increases in water level. However, their findings are for managed realignment sites near the mouth of the estuaries. Townend and Pethick (2002) conducted a similar study in a different estuary and found that managed realignment sites in the outer estuary tend to increase water levels in the estuary, and managed realignment sites in the inner estuary tend to decrease water levels. The findings of this research aligned with the results of the study by Townend and Pethick (2002) and supported that changes in water level were a function of the location of the managed

realignment site within an estuary. This outcome is ideal as flood reduction was one of the main goals of implementing managed realignment at this particular location.

The UK Environment Agency has developed flood risk management strategies for a number of estuaries, and as a result of the Townend and Pethick (2002) modelling study supporting the Humber Estuary Flood Risk Management Strategy, they have started developing strategy plans and programs for other estuaries in the UK (e.g., the Thames Estuary) with the importance of managed realignment location within the estuary in mind (Pontee, 2015; Halcrow and HR Wallingford, 2006). However, a recent study by Bennett et al. (2020) showed no change in water levels throughout the estuary being studied (i.e., the Taf Estuary) after managed realignment. Although the findings from this research for the Salmon River Estuary supported one of the findings from the Humber Estuary study, other studies have concluded different things, indicating that more research is needed to truly understand the response of different estuaries to managed realignment.

5.5. Model Limitations and Recommendations for Future Work

As with any type of research, there will always be limitations to the methods being employed, lessons learned and recommendations to help improve results in future works. This research was no exception. The following will list some model limitations and present some recommendations for future students or professionals that choose to build upon this work.

In terms of the methods used for modelling in this thesis, there were two different categories of limitations: (1) limitations based on the type of method employed and (2) limitations based on the exclusion of important components from the methods. In the case

of this research, the first category refers to the method chosen for model calibration, which was to adjust predicted water levels (via the free, online WebTide model) iteratively until the modelled water level results matched well enough with the measured water level results. This method was chosen because there was no factor or value that would accurately convert WebTide-modelled water levels in mean sea level (MSL) to CGVD28 for this area and because there were no permanent tide gauges in the upper Bay of Fundy to extract real observations from. This choice was limiting because the conversion (via iterative water level adjustments) may not have been entirely accurate or correct, which may have influenced model results.

The second category refers to what was not included in the hydrodynamic model, such as a vegetation module, sediment transport and the simulation of fluid mud, which was detected in the estuary. The decision to exclude these components was limiting in that it created a model that was not as detailed as those in similar studies (Mulligan et al., 2013; Ashall et al., 2016; Bennett et al., 2020), which used either a vegetation module, a sediment transport module, or a combination of both. Ashall et al. (2016) used a vegetation module for his research in the Cornwallis Estuary, Bay of Fundy, and quantified the influence of vegetation on modelled flow velocities. Vegetation decreases flow velocities on a marsh platform as a result of drag force, and this was confirmed by Ashall et al. (2016) using a hydrodynamic model. The use of a sediment transport module coupled with the hydrodynamic module (FLOW) in Delft3D is critical because sediment in water heavily influences hydrodynamics, and in the Salmon River and North River near the restoration site, measured suspended sediment concentrations were extremely variable and reached upwards of 350 g/L at the upstream location. Incorporating sediment

transport would assist in understanding this system even more and possibly result in more accurate model predictions. Incorporating fluid mud into the sediment transport module is important as well, although complicated. Therefore, it is recommended to focus on the basic sediment transport module with fluid mud simulations as an option.

Another limitation to consider, and one that falls in both categories listed above, is the level of detail in the model grid. The model grid created and used for this thesis research was 2D, Cartesian rectangular structured grid with the highest resolution at the restoration site of 6 m. Three aspects of this grid can be improved for future modelling, with the first being the dimension of the grid. A 2D model is commonly used (Pontee, 2015; Bennett et al., 2020) and sufficient for the purpose of this thesis, however, changing the grid to 3D would eliminate depth averaged velocities and simulate more detailed velocity profiles throughout the water column. This would allow for a better comparison to the sample volume (i.e., single point) velocities measured with the ADVs and the velocity profiles measured with the ADCPs. The model grid could also be structured differently. The model grid used for this research was rectangular, which does not contour to the river channel, whereas a curvilinear grid would contour to the river channel and may produce a more accurate simulation. An individual grid cell in a curvilinear grid would transfer its simulation results to the next grid cell more smoothly as it contours the edges of the river channel because the grid cell elevations within the channel would not include a portion of the higher-elevated marsh platforms, or even dykes. However, this would depend on how fine the grid resolution is, which is the final aspect of the model grid that could be improved. For this thesis research, a high-resolution grid was created, but only at the location of the restoration site. The grid

resolution was lowest (25 m) at the outer boundaries of the model domain. For future works, the existing grid resolution could be refined even more. The best recommendation would be to refine the entire grid to a resolution of 6 m, but this would require a lot of computing power and would increase the run time of the model. A more feasible option would be to increase the resolution of the grid to 6 m within the full study area, or at least within the river channels and restoration site. This would help in computing a more resolved river channel and may produce better model results in the North River. When selecting a grid resolution, one must also consider the resolution of the input DEM. The DEM resolution in the study area of this research was 1 m, meaning one could justify refining the grid resolution to 1 m for the study area.

Lastly, there are some recommendations for field measurements if one decides to continue this line of research. The first would be to collect field data more frequently and over longer periods of time. Based on the highly dynamic nature of the inner Salmon River Estuary, field deployments at least once a season for at least one year would be recommended, especially during spring tides and the highest tide of the year, if possible. Conducting field measurements over a short period of time does provide a very detailed and accurate representation of hydrodynamics within an estuary, but the data may only reflect a natural fluctuation (e.g., temporary stormy conditions, causing greater flooding, discharge and sediment delivery) as opposed to a long-term trend (Woodroffe, 2003). In terms of frequency of data collection, conditions can change rapidly (e.g., within minutes), seasonally due to changes in weather and subsequent changes in discharge, sedimentation/erosion rates, etc., annually due to climate change and over decades due to changes in land use (Crawford, 2006). Hence, the need for long-term and frequent

monitoring of conditions in the Salmon River Estuary to better understand its behaviour and to more accurately predict flooding outcomes. Another recommendation would be to deploy more than six instruments throughout the study area, if possible. Additional sampling stations would be most beneficial at the tidal boundary and at random locations throughout the estuary upstream from the tidal boundary. The purpose of these additional measurements is to calibrate the model with observed data instead of data from another model. It would make the calibration more accurate and would most likely produce more accurate results. However, data used for calibration should not be used to validate the model. One should have a different dataset of measurements for validating the model. Also, deploying the instruments at the same locations chosen for this research is recommended to allow for a direct comparison. To assess how river conditions change over time, measuring at the same locations is important. The last recommendation is to check the quality of data collected by the ADCPs after the first tide if multiple tides are to be sampled per deployment. If the data does not appear to be of good quality after the first tide, the instrument settings can be changed to hopefully obtain better results from subsequent tides.

Although there exist many limitations and recommendations, those discussed above are the most important for producing better, more reliable results.

Chapter 6 – Conclusion

One of the greatest challenges in the world today, and for centuries to come, is dealing with a changing climate. Two of many consequences of the world's rapidly warming climate is sea level rise and an increase in the frequency and intensity of storm events. The areas that are most at risk to sea level rise and storm surges are low-lying coastal zones. Coastal communities within these zones are already experiencing the impacts of these changes at an increasingly high rate, making it even more challenging to adapt. Truro, Nova Scotia, is one example of a coastal community that has a history of flooding and will continue to flood with increasing severity due to climate change.

This research addressed the issue of flooding in Truro and investigated the potential positive impacts of intentionally realigning a section of dyke and restoring 92 hectares of the natural floodplain of the Salmon River Estuary using a hydrodynamic model (i.e., Delft3D) as part of the project design process. In summary, the model results indicated that Delft3D was successful at simulating river conditions near the restoration site, as compared to field measurements. Model results for the managed realignment scenario (with dykes breached in the DEM) predicted a successful managed realignment and subsequent restoration of tidal wetland habitat based on modelled flood extents and currents. Different modelled flood extents were derived from increasing water levels at the tidal boundary of the model grid by increments of 5 cm, which can represent larger tides, a storm surge or future sea level rise. Delft3D also predicted that water levels in the main river channels would decrease once the dykes have been breached, contributing to a reduction in flooding of areas upstream of the restoration site. Delft3D provided quantitative information related to flood scenarios in the Salmon River Estuary and

provided evidence that the managed realignment design selected for this site was appropriate. These findings supported the use of a hydrodynamic model, such as Delft3D, to assist in planning for future managed realignment projects, whether it is at another location within the Salmon River Estuary or somewhere else in the world.

Future work that expands upon this research should include updating the bathymetry of the Salmon River and North River again, collecting new field data (perhaps making more measurements, deploying instruments at new locations, deploying more instruments and deploying more frequently over the course of a year to capture seasonal trends), the use of a more detailed hydrodynamic model (i.e., the inclusion of a vegetation module, sediment transport, a better model grid, etc.) and a comparison between the model results in this thesis to measured results and surveys of the study area after managed realignment is implemented. It would also be beneficial to investigate more realistic future flood scenarios using sea level rise predictions for Truro, Nova Scotia.

References

- Allen, J. R. L. (2000). Morphodynamics of Holocene salt marshes: a review sketch from the Atlantic and Southern North Sea coasts of Europe. *Quaternary Science Reviews*, 19(12), 1155-1231. doi:10.1016/S0277-3791(99)00034-7
- Almeida, D., Neto, C. S. & Costa, J. C. (2017). Active or passive recovery? Discussing implications of vegetation diversity in unmanaged salt marshes. *Estuarine, Coastal and Shelf Science*, 191, 201-208. doi:10.1016/j.ecss.2017.04.018
- Amos, C. L. (1977). Effects of tidal power structures on sediment transport and loading in the Bay of Fundy-Gulf of Maine system. In: G. R. Daborn (Ed.), *Fundy Tidal Power and the Environment* (pp. 233-276). Wolfville, Nova Scotia: The Acadia University Institute.
- Ashall, L. M., Mulligan, R. P., van Proosdij, D., & Poirier, E. (2016). Application and validation of a three-dimensional hydrodynamic model of a macrotidal salt marsh. *Coastal Engineering*, 114, 35-46. doi:10.1016/j.coastaleng.2016.04.005
- Bennett, W. G., van Veelen, T. J., Fairchild, T. P., Griffin, J. N. & Karunarathna, H. (2020). Computational modelling of the impacts of saltmarsh management interventions on hydrodynamics of a small macro-tidal estuary. *Journal of Marine Science and Engineering*, 8(373), 1-30. doi:10.3390/jmse8050373
- Boone, L. K., Ollerhead, J., Barbeau, M. A., Beck, A. D., Sanderson, B. G. & McLellan, N. R. (2017). Returning the tide to dikelands in a macrotidal and ice-influenced environment: Challenges and lessons learned. In: C. W. Finkl & C. Makowski (Eds.), *Coastal wetlands: Alteration and remediation* (pp. 705-749). Retrieved from Springer database. doi:10.1007/978-3-319-56179-0

- Borchert, S. M., Osland, M. J., Enwright, N. M. & Griffith, K. T. (2018). Coastal wetland adaptation to sea level rise: Quantifying potential for landward migration and coastal squeeze. *Journal of Applied Ecology*, 55(6), 2876-2887.
<https://doi.org/10.1111/1365-2664.13169>
- Bowron, T. M., Neatt, N., Graham, J. & van Proosdij, D. (2015a). *Post-Restoration Monitoring (Year 5) of the Cogmagun River Salt Marsh Restoration Project*. CBWES. DOI:10.13140/RG.2.2.31264.99840
- Bowron, T. M., Neatt, N., Graham, J. & van Proosdij, D. (2015b). *Post-Restoration Monitoring (Year 5) of the St. Croix River High Salt Marsh & Tidal Wetland Restoration Project*. CBWES. doi:10.13140/RG.2.2.11132.33921
- Bowron, T. M., Neatt, N., van Proosdij, D. & Lundholm, J. (2012). Salt Marsh Tidal Restoration in Canada's Maritime Provinces. In: C. T. Roman & D. M. Burdick (Eds.), *Tidal Marsh Restoration*. (pp. 191-209). Island Press, Washington, DC.
https://doi.org/10.5822/978-1-61091-229-7_13
- CBCL Limited. (2017). *Flood Risk Study*. Retrieved from <https://www.truro.ca/adm/708-truro-flood-risk-study/file.html>
- Chen, Z., Curran, P. J. & Hansom, J. D. (1992). Derivative reflectance spectroscopy to estimate suspended sediment concentration. *Remote Sensing of Environment*, 40, 67-77.
- Cheong, S., Silliman, B., Wong, P. P., van Wesenbeeck, B., Kim, C. & Guannel, G. (2013). Coastal adaptation with ecological engineering. *Nature Climate Change*, 3, 787-791. <https://doi.org/10.1038/nclimate1854>
- Clunies, G. J., Mulligan, R. P., Mallinson, D. J. & Walsh, J. P. (2017). Modeling

hydrodynamics of large lagoons: Insights from the Albemarle-Pamlico Estuarine System. *Estuarine, Coastal and Shelf Science*, 189, 90-103.

<https://doi.org/10.1016/j.ecss.2017.03.012>

Costa, P. J. M. (2016). Sediment Transport. In: M. J. Kennish (Ed.), *Encyclopedia of Estuaries. Encyclopedia of Earth Sciences Series*. Springer, Dordrecht.

Cranford, P. J., Gordon, D. C., & Jarvis, C. M. (1989). Measurement of cordgrass, *Spartina alterniflora*, production in a macrotidal estuary, Bay of Fundy. *Estuaries*, 12(1), 27-34. doi:10.2307/1351447

Crawford, C. (2006). *Indicators for the condition of estuaries and coastal waters*.

Tasmanian Aquaculture and Fisheries Institute. <https://eprints.utas.edu.au/6642/>

Crewe, B. (2004). *Characterization of sediment in the Salmon River estuary*. [Master's thesis, Dalhousie University and Nova Scotia Agricultural College].

Dalrymple, R. W. (2006). Incised valleys in space and time: An introduction to the volume and an examination of the controls on valley formation and filling. In: R. W. Dalrymple, D. A. Leckie & R. W. Tillman (Eds.), *Incised valleys in space and time* (pp. 5-12). SEPM Special Publications No. 85. Society for Sedimentary Geology, Tulsa.

Dalrymple, R. W. & Choi, K. (2007). Morphologic and facies trends through the fluvial-marine transition in tide-dominated depositional systems: A schematic framework for environmental and sequence-stratigraphic interpretation. *Earth-Science Reviews*, 81(3-4), 135-174. <https://doi.org/10.1016/j.earscirev.2006.10.002>

Dalrymple, R. W., Knight, R. J., Zaitlin, B. A. & Middleton, G. V. (1990). Dynamics and

- facies model of a macrotidal sand bar complex, Cobequid Bay-Salmon River Estuary (Bay of Fundy). *Sedimentology*, 35. 577-612.
- Dalrymple, R. W., Mackay, D. A., Ichaso, A. A. & Choi, K. S. (2012). Processes, Morphodynamics, and Facies of Tide-Dominated Estuaries. In: R. Davis Jr. & R. W. Dalrymple (Eds.). *Principles of Tidal Sedimentology*. Springer, Dordrecht.
- Dalrymple, R. W., Zaitlin, B. A. & Boyd, R. (1992). Estuarine facies models; conceptual basis and stratigraphic implications. *Journal of Sedimentary Research*, 62(6), 1130-1146. <https://doi.org/10.1306/D4267A69-2B26-11D7-8648000102C1865D>
- Davidson-Arnott, R. G. D., van Proosdij, D., Ollerhead, J. & Schostak, L. (2002). Hydrodynamics and sedimentation in salt marshes: Examples from a macrotidal marsh, Bay of Fundy. *Geomorphology*, 48(1-3), 209-231. [https://doi.org/10.1016/S0169-555X\(02\)00182-4](https://doi.org/10.1016/S0169-555X(02)00182-4)
- Desplanque, C. & Mossman, D. J. (2001). Bay of Fundy Tides. *Geoscience Canada*, 28(1). Retrieved from <https://journals.lib.unb.ca/index.php/GC/article/view/4065>
- Desplanque, C. & Mossman, D. J. (2004). Tides and their seminal impact on the geology, geography, history, and socio-economics of the Bay of Fundy, eastern Canada. *Atlantic Geology*, 40(1), 3-35.
- Doxaran, D., Froidefond, J. M., Castaing, P. & Babin, M. (2009). Dynamics of the turbidity maximum zone in a macrotidal estuary (the Gironde, France): Observations from field and MODIS satellite data. *Estuarine, Coastal and Shelf Science*, 81(3), 321-332. <https://doi.org/10.1016/j.ecss.2008.11.013>
- Dronkers, J. (1986). Tidal asymmetry and estuarine morphology. *Netherlands Journal of Sea Research*, 20(2-3), 117-131. [https://doi.org/10.1016/0077-7579\(86\)90036-0](https://doi.org/10.1016/0077-7579(86)90036-0)

- Dupont, F., Hannah, C. G. & Greenberg, D. (2005). Modelling the sea level in the upper Bay of Fundy. *Atmosphere-Ocean*, 43(1), 33-47.
<https://doi.org/10.3137/ao.430103>
- Environment Canada. (2018). Daily Discharge Data for NORTH RIVER AT NORTH RIVER (01DH004) [Table]. Available from
https://wateroffice.ec.gc.ca/mainmenu/historical_data_index_e.html
- Erfanzadeh, R., Garbutt, A., Pétition, J., Maelfait, J. & Hoffmann, M. (2010). Factors affecting the success of early salt-marsh colonizers: Seed availability rather than site suitability and dispersal traits. *Plant Ecology*, 206(2), 335-347. Springer.
- Erwin, K. L. (2009). Wetlands and global climate change: the role of wetland restoration in a changing world. *Wetlands, Ecology and Management*, 17(1), 71-84.
doi:10.1007/s11273-008-9119-1
- Esteves, L. S. & Thomas, K. (2014). Managed realignment in practice in the UK: Results from two independent surveys. *Journal of Coastal Research*, SI(70), 407-413.
- Esteves, L. S. & Williams, J. J. (2017). Managed realignment in Europe: A synthesis of methods, achievements and challenges. In: Bilkovic, D. M., Mitchell, M. M., Toft, J. D. & La Peyre, M. K. (eds.), *Living Shorelines: The Science and Management of Nature-based Coastal Protection* (pp. 157-180). CRC Press/Taylor & Francis Group.
- Esteves, L. S. (2014). *Managed realignment: A viable long-term coastal management strategy?* Available from <https://link.springer.com/book/10.1007%2F978-94-017-9029-1>
- Faas, R. W. (1991). Rheological boundaries of mud: Where are the limits? *Geo-Marine*

Letters, 11, 143-146. <https://doi.org/10.1007/BF02431000>

- Fisheries and Oceans Canada. (2018). 7 days Tidal Predictions (Burntcoat Head #270) [Online table]. Retrieved from <https://www.tides.gc.ca/eng/station?sid=270>
- French, P. W. (2006). Managed realignment – The developing story of a comparatively new approach to soft engineering. *Estuarine Coastal and Shelf Science*, 67, 409-423. doi:10.1016/j.ecss.2005.11.035
- Friedrichs, C. T. & Perry, J. E. (2001). Tidal salt marsh morphodynamics: A synthesis. *Journal of Coastal Research*, SI(27), 7-37.
- Friess, D. A., Möller, I., Spencer, T., Smith, G. M., Thomson, A. G., & Hill, R. A. (2014). Coastal saltmarsh managed realignment drives rapid breach inlet and external creek evolution, Freiston Shore (UK). *Geomorphology*, 208, 22-33. doi:10.1016/j.geomorph.2013.11.010
- Fugate, D. C. & Friedrichs, C. T. (2002). Determining concentration and fall velocity of estuarine particle populations using ADV, OBS and LISST. *Continental Shelf Research*, 22(11), 1867-1886. doi:10.1016/S0278-4343(02)00043-2
- Garbutt, R. A., Reading, C. J., Wolters, M., Gray, A. J., & Rothery, P. (2006). Monitoring the development of intertidal habitats on former agricultural land after the managed realignment of coastal defenses at Tollesbury, Essex, UK. *Marine Pollution Bulletin*, 53(1-4), 155-164. doi:10.1016/j.marpolbul.2005.09.015
- Garcia, M. H. (2008). Sediment transport and morphodynamics. *Sedimentation engineering: Processes, measurements, modeling, and practice*, 110, 21-164.
- Garrett, C. (1972). Tidal resonance in the Bay of Fundy and Gulf of Maine. *Nature*, 238, 441-443. doi:10.1038/238441a0

- Greenberg, D. A., Blanchard, W., Smith, B. & Barrow, E. (2012). Climate change, mean sea level and high tides in the Bay of Fundy. *Atmosphere-Ocean*, 50(3), 261-276. doi:10.1080/07055900.2012.668670
- Guo, L., Brand, M., Sanders, B. F., Fofoula-Georgiou, E. & Stein, E. D. (2018). Tidal asymmetry and residual sediment transport in a short tidal basin under sea level rise. *Advances in Water Resources*, 121, 1-8. <https://doi.org/10.1016/j.advwatres.2018.07.012>
- Halcrow and HR Wallingford. (2006). *Thames Estuary 2100. Early Conceptual Options: Responses Affecting Water Levels: Initial Tests*. ECO Report R1. Report produced by Halcrow Group Ltd. and HR Wallingford Ltd. for the Environment Agency. September 2006, 141 pp.
- Hanson, A. & Calkins, L. (1996). *Wetlands of the Maritime Provinces: Revised documentation for the wetlands inventory*. Environment Canada, Canadian Wildlife Service, Atlantic Region.
- Harman, B. P., Heyenga, S., Taylor, B. M. & Fletcher, C. S. (2015). Global lessons for adapting coastal communities to protect against storm surge inundation. *Journal of Coastal Research*, 31(4), 790-801. <https://doi.org/10.2112/JCOASTRES-D-13-00095.1>
- Hu, K., Chen, Q., Wang, H., Hartig, E. K., & Orton, P. M. (2018). Numerical modeling of salt marsh morphological change induced by Hurricane Sandy. *Coastal Engineering*, 132, 63-81. doi:10.1016/j.coastaleng.2017.11.001
- Hughes, S. A. (1993). *Physical models and laboratory techniques in coastal engineering*

(Vol. 7 of Advanced Series on Ocean Engineering, 568 pp.). Singapore: World Scientific.

Hume, T. M. (2005). Tidal Prism. In: M. L. Schwartz (Ed.), *Encyclopedia of Coastal Science. Encyclopedia of Earth Science Series*. Springer, Dordrecht.

https://doi.org/10.1007/1-4020-3880-1_320

Intergovernmental Panel on Climate Change. (1990). Summary for Policymakers. In *Climate Change: The IPCC Response Strategies (1990). Contribution of Working Group III to the First Assessment Report of the Intergovernmental Panel on Climate Change*. (pp. 1-330). Retrieved from

http://www.ipcc.ch/ipccreports/far/wg_III/ipcc_far_wg_III_full_report.pdf

Intergovernmental Panel on Climate Change. (2014). Synthesis Report. In Core Writing Team, R.K. Pachauri and L.A. Meyer (Eds.), *Climate Change 2014: Synthesis Report. Contribution of Working Groups I, II and III to the Fifth Assessment Report of the Intergovernmental Panel on Climate Change*. (pp. 1-151). Geneva, Switzerland: Cambridge University Press. Retrieved from [http://ar5-](http://ar5-syr.ipcc.ch/ipcc/ipcc/resources/pdf/IPCC_SynthesisReport.pdf)

[syr.ipcc.ch/ipcc/ipcc/resources/pdf/IPCC_SynthesisReport.pdf](http://ar5-syr.ipcc.ch/ipcc/ipcc/resources/pdf/IPCC_SynthesisReport.pdf)

Kiesel, J., Schuerch, M., Christie, E. K., Möller, I., Spencer, T. & Vafeidis, A. T. (2020). Effective design of managed realignment schemes can reduce coastal flood risks. *Estuarine, Coastal and Shelf Science*, 242, 1-13.

Kidd, I. M. (2016). *Strategies for Sustainable Morphological Remediation of the Tamar River Estuary and other Similarly Degraded Estuaries*. [PhD thesis, University of Tasmania]. University of Tasmania Open Access Repository.

Kirby, R., Henderson, P. A., Warwick, R. M. (2004). The Severn, UK: Why is the

- estuary different? *Journal of Marine Science and Environment*, No C2, 1-17.
- Leonard, L. A. & Croft, A. L. (2006). The effect of standing biomass on flow velocity and turbulence in *Spartina alterniflora* canopies. *Estuarine, Coastal and Shelf Science*, 69(3), 325-336. doi:10.1016/j.ecss.2006.05.004
- Leonard, L. A. & Luther, M. E. (1995). Flow hydrodynamics in tidal marsh canopies. *Limnology and Oceanography*, 40(8), 1474-1484.
- Lesser, G.R., Roelvink, J. A., van Kester, J. A. T. M. & Stelling, G.S. (2004). Development and validation of a three-dimensional morphological model. *Coastal Engineering*, 51, 883-915. doi:10.1016/j.coastaleng.2004.07.014
- Lynch, D. K. (1982). Tidal bores. *Scientific American*, 247(4), 146-157.
- Marvin, J. T. & Wilson, A. T. (2016). One dimensional, two dimensional and three dimensional hydrodynamic modeling of a dyked coastal river in the Bay of Fundy. *Journal of Water Management Modeling*, 25(C404), 1-13.
doi:10.14796/JWM M.C404
- Matheson, G. (2020). *Enhancing Dykeland Resiliency in a Hypertidal Estuary*. [Master's thesis, Saint Mary's University]. Saint Mary's University Online Repository.
- Moffatt & Nichol Engineers. (2005). *Hydrodynamic Modelling Tools and Techniques*. Retrieved from http://www.southbayrestoration.org/pdf_files/Modeling_Report-Full-Jan2005.pdf
- Möller, I., Spencer, T., French, J. R., Leggett, D. J., & Dixon, M. (1999). Wave transformation over salt marshes: A field and numerical modelling study from Norfolk, England. *Estuarine, Coastal and Shelf Science*, 49(3), 411-426.
doi:10.1006/ecss.1999.0509

- Morris, J. T., Sundareshwar, P. V., Nietch C. T., Kjerfve, B., & Cahoon, D. R. (2002). Responses of coastal wetlands to rising sea level. *Ecology*, 83(10), 2869-2877. doi:10.1890/0012-9658(2002)083[2869:ROCWTR]2.0.CO2
- Morris, R. L., Konlechner, T. M., Ghisalberti, M. & Swearer, S. E. (2018). From grey to green: Efficacy of eco-engineering solutions for nature-based coastal defence. *Global Change Biology*, 24(5), 1827-1842. <https://doi.org/10.1111/gcb.14063>
- Mulligan, R. P., Smith, P. C., Hill, P. S., Tao, J. & van Proosdij, D. (2013). Effects of tidal power generation on hydrodynamics and sediment processes in the upper Bay of Fundy. *Proceedings of the 4th Speciality Conference on Coastal, Estuary and Offshore Engineering*. Montreal, QC.
- Narayan, S., Beck, M. W., Reguero, B. G., Losada, I. J., van Wesenbeeck, B., ... Burks-Copes, K. A. (2016). The effectiveness, costs and coastal protection benefits of natural and nature-based defenses. *PLoS ONE* 11(5): e0154735. doi:10.1371/journal.pone.0154735
- Neatt, N., Bowron, T. M., Graham, J. & van Proosdij, D. (2013). *Post-Restoration Monitoring (Year 7) of the Walton River Salt Marsh Restoration Project*. CBWES. doi:10.13140/RG.2.2.32103.85923
- Neumeier, U. (2007). Velocity and turbulence variations at the edge of saltmarshes. *Continental Shelf Research*, 27(8), 1046-1059. doi:10.1016/j.csr.2005.07.009
- Neumeier, U. & Amos, C. L. (2006). The influence of vegetation on turbulence and flow velocities in European salt-marshes. *Sedimentology*, 53(2), 259-277. doi:10.1111/j.1365-3091.2006.00772.x
- Ni, W., Wang, Y. P., Symonds, A. M. & Collins, M. B. (2014). Intertidal flat

- development in response to controlled embankment retreat: Freiston Shore, The Wash, UK. *Marine Geology*, 355, 260-273.
- Nichols, M. M. (1988). Consequences of dredging. In: B. Kjerfve (Ed.), *Hydrodynamics of Estuaries: Volume II Estuarine Case Studies*. CRC Revivals.
- Pontee, N. I. (2015). Impact of managed realignment design on estuarine water levels. *Proceedings of the Institution of Civil Engineers – Maritime Engineering*, 168(2), 48-61. <https://doi.org/10.1680/jmaen.13.00016>
- Propato, M., Clough, J. S. & Polaczyk, A. (2018). Evaluating the costs and benefits of marsh-management strategies while accounting for uncertain sea-level rise and ecosystem response. *PLoS One*, 13(8), e0200368.
doi:10.1371/journal.pone.0200368
- Pugh, D. & Woodworth, P. (2014). *Sea-Level Science: Understanding Tides, Surges, Tsunamis and Mean Sea-Level Changes*. Cambridge University Press.
- Rahman, H. M. T., Sherren, K. & van Proosdij, D. (2019). Institutional innovation for nature-based coastal adaptation: Lessons from salt marsh restoration in Nova Scotia, Canada. *Sustainability*, 11(23), 1-26. <https://doi.org/10.3390/su11236735>
- Rotman, R., Naylor, L., McDonnell, R. & MacNiocaill, C. (2008). Sediment transport on the Freiston Shore managed realignment site: An investigation using environmental magnetism. *Geomorphology*, 100(3-4), 241-255.
- Ruckelshaus, M. H., Guannel, G., Arkema, K., Verutes, G., Griffin, R. & Guerry, A. (2016). Evaluating the benefits of green infrastructure for coastal areas: Location, location, location. *Coastal Management*, 44(5), 504-516.
doi:10.1080/08920753.2016.1208882

- Seenath, A., Wilson, M., & Miller, K. (2016). Hydrodynamic versus GIS modelling for coastal flood vulnerability assessment: Which is better for guiding coastal management? *Ocean & Coastal Management*, *120*, 99-109.
doi:10.1016/j.ocecoaman.2015.11.019
- Shaw, J., Amos, C. L., Greenberg, D. A., O'Reilly, C. T., Parrott, D. R. & Patton, E. (2010). Catastrophic tidal expansion in the Bay of Fundy, Canada. *Canadian Journal of Earth Sciences*, *47*(8), 1079-1091. <https://doi.org/10.1139/E10-046>
- Sherren, K., Bowron, T., Graham, J. M., Rahman, H. M. T. & van Proosdij, D. (2019). Coastal infrastructure realignment and salt marsh restoration in Nova Scotia, Canada. Chapter 5 in *Responding to Rising Seas: OECD Country Approaches to Tackling Coastal Risks*, 111-135. OECD Publishing: Paris, France.
- Sierra-Correa, P. C. & Kintz, J. R. C. (2015). Ecosystem-based adaptation for improving coastal planning for sea-level rise: A systematic review for mangrove coasts. *Marine Policy*, *51*, 385-393. <https://doi.org/10.1016/j.marpol.2014.09.013>
- Singh, K., Walters, B. B., & Ollerhead, J. (2007). Climate change, sea-level rise and the case for salt marsh restoration in the Bay of Fundy, Canada. *Environments Journal*, *35*(2), 71-84.
- SonTek. (2012a). *HydroSurveyor System: Frequently Asked Questions Guide*. Retrieved from <https://www.sontek.com/media/pdfs/hydrosurveyor-faqs.pdf>
- SonTek. (2012b). *SonTek HydroSurveyor™* [Brochure]. Retrieved from [https://www.sontek.com/media/pdfs/hydrosurveyor-brochure-\(reduced\).pdf](https://www.sontek.com/media/pdfs/hydrosurveyor-brochure-(reduced).pdf)
- Spalding, M. D., Ruffo, S., Lacambra, C., Meliane, I., Hale, L. Z., Shepard, C. C. & Beck

- M. W. (2014). The role of ecosystems in coastal protection: Adapting to climate change and coastal hazards. *Ocean & Coastal Management*, 90, 50-57.
<http://dx.doi.org/10.1016/j.ocecoaman.2013.09.007>
- Spencer, K. L. & Harvey, G. L. (2012). Understanding system disturbance and ecosystem services in restored saltmarshes: Integrating physical and biogeochemical processes. *Estuarine, Coastal and Shelf Science*, 106, 23-32.
[doi:10.1016/j.ecss.2012.04.020](https://doi.org/10.1016/j.ecss.2012.04.020)
- Stevens, J. (2019). Massive Muddy Tides in the Bay of Fundy [Satellite image]. *NASA Earth Observatory*. <https://earthobservatory.nasa.gov/images/145784/massive-muddy-tides-in-the-bay-of-fundy>
- Symonds, A. M., Vijverberg, T., Post S., van der Spek, B., Henrotte, J. & Sokolewicz, M. (2016). Comparison between Mike 21 FM, Delft3D and Delft3D FM flow models of Western Port Bay, Australia. *Proceedings of 35th Conference on Coastal Engineering*. Antalya, Turkey.
- Temmerman, S., Meire, P., Bouma, T. J., Herman, P. M. J., Ysebaert, T. & De Vriend, H. J. (2013). Ecosystem-based coastal defense in the face of global change. *Nature*, 504, 79-83. <https://doi.org/10.1038/nature12859>
- Todd, B. J., Shaw, J., Li, M. Z., Kostylev, V. E., & Wu, Y. (2014). Distribution of subtidal sedimentary bedforms in a macrotidal setting: The Bay of Fundy, Atlantic Canada. *Continental Shelf Research*, 83(15), 64-85.
<https://doi.org/10.1016/j.csr.2013.11.017>
- Townend, I. & Pethick, J. (2002). Estuarine flooding and managed retreat. *Philosophical*

Transactions of the Royal Society of London, 360, 1477-1495.

doi:10.1098/rsta.2002.1011

Urick, R. J. (2005). The absorption of sound in suspensions of irregular particles. *The Journal of the Acoustical Society of America*, 20(3), 283-289.

van Proosdij, D., Davidson-Arnott, R. G. D., & Ollerhead, J. (2006). Controls on spatial patterns of sediment deposition across a macro-tidal salt marsh surface over single tidal cycles. *Estuarine, Coastal and Shelf Science*, 69(1), 64-86.

doi:10.1016/j.ecss.2006.04.022

van Proosdij, D., Matheson, G., & Ross, C. (2018). Influence of dykeland engineering and management strategies on the intertidal geomorphodynamics of a fetch-limited, temperate, hypertidal estuary. *AGUFM*, 2018, EP13A-08.

van Wesenbeeck, B. K., de Boer, W., Narayan, S., van der Star, W. R. L., & de Vries, M. B. (2017). Coastal and riverine ecosystems as adaptive flood defenses under a changing climate. *Mitigation and Adaptation Strategies for Global Change*, 22, 1087-1094. doi:10.1007/s11027-016-9714-z

Vandenbruwaene, W., Maris, T., Cox, T. J. S., Cahoon, D. R., Meire, P. & Temmerman, S. (2011). Sedimentation and response to sea-level rise of a restored marsh with reduced tidal exchange: Comparison with a natural tidal marsh. *Geomorphology*, 130(3-4), 115-126. <https://doi.org/10.1016/j.geomorph.2011.03.004>

Vuik, V., Jonkman, S. N., Borsje, B. W., & Suzuki, T. (2016). Nature-based flood protection: The efficiency of vegetated foreshores for reducing wave loads on coastal dikes. *Coastal Engineering*, 116, 42-56.

doi:10.1016/j.coastaleng.2016.06.001

- Wang, L. (2010). *Tide Driven Dynamics of Subaqueous Fluid Mud Layers in Turbidity Maximum Zones of German Estuaries* [Doctoral dissertation, University of Bremen].
- Wang, P. (2012). Principles of Sediment Transport Applicable in Tidal Environments. In: R. Davis Jr. & R. W. Dalrymple (Eds.). *Principles of Tidal Sedimentology*. Springer, Dordrecht.
- Watts, C. W., Tolhurst, T. J., Black, K. S., & Whitmore, A. P. (2003). In situ measurements of erosion shear stress and geotechnical shear strength of the intertidal sediments of the experimental managed realignment scheme at Tollesbury, Essex, UK. *Estuarine, Coastal and Shelf Science*, 58(3), 611-620.
doi:10.1016/S0272-7714(03)00139-2
- Weissenberger, S. & Chouinard, O. (2015). *Adaptation to Climate Change and Sea Level Rise: The Case Study of Coastal Communities in New Brunswick, Canada*. Available from <https://doi-org.library.smu.ca/10.1007/978-94-017-9888-4>
- Wells, J. T. (1995). Geomorphology and Sedimentology of Estuaries. In: G. M. E. Perillo (Ed.). *Developments in Sedimentology*, 53.
- Williams, P. B. & Orr, M. K. (2002). Physical evolution of restored breached levee salt marshes in the San Francisco Bay estuary. *Restoration Ecology*, 10(3), 527-542.
doi:10.1046/j. 1526-100X.2002.02031.x
- Wolanski, E. & Elliott, M. (2015). *Estuarine Ecohydrology: An Introduction* (2nd edition). Elsevier Science. <https://doi.org/10.1016/C2013-0-13014-0>
- Wolters, M., Garbutt, A. & Bakker, J. P. (2005). Salt-marsh restoration: Evaluating the

success of de-embankments in north-west Europe. *Biological Conservation*, 123, 249-268. doi:10.1016/j.biocon.2004.11.013

Wolters, M., Garbutt, A. & Bakker, R. M., Bakker, J. P. & Carey, P. D. (2008).

Restoration of salt-marsh vegetation in relation to site suitability, species pool and dispersal traits. *Journal of Applied Ecology*, 45, 904-912. doi:10.1111/j.1365-2664.2008.01453.x

Wong, P.P., I.J. Losada, J.-P. Gattuso, J. Hinkel, A. Khattabi, K.L. McInnes, Y. Saito,

and A. Sallenger, 2014: Coastal systems and low-lying areas. In: *Climate Change 2014: Impacts, Adaptation, and Vulnerability. Part A: Global and Sectoral*

Aspects. Contribution of Working Group II to the Fifth Assessment Report of the Intergovernmental Panel on Climate Change [Field, C.B., V.R. Barros, D.J.

Dokken, K.J. Mach, M.D. Mastrandrea, T.E. Bilir, M. Chatterjee, K.L. Ebi, Y.O.

Estrada, R.C. Genova, B. Girma, E.S. Kissel, A.N. Levy, S. MacCracken, P.R.

Mastrandrea, and L.L. White (eds.)]. Cambridge University Press, Cambridge,

United Kingdom and New York, NY, USA, pp. 361-409.

Woodroffe, C. D. (2003). *Coasts: Form, Process and Evolution*. Cambridge University Press. doi:10.1017/CBO9781316036518

Woolnough, S. J., Allen, J. R. L., & Wood, W. L. (1995). An exploratory numerical

model of sediment deposition over tidal salt marshes. *Estuarine, Coastal and*

Shelf Science, 41(5), 515-543. doi:10.1016/0272-7714(95)90025-X

Wu, Y., Chaffey, J., Greenberg, D. A., Colbo, K. & Smith, P. C. (2011). Tidally-

influenced sediment transport patterns in the upper Bay of Fundy: A numerical

study. *Continental Shelf Research*, 31(19), 2041-2053.

Xia, J., Falconer, R. A. & Lin, B. (2010). Hydrodynamic impact of a tidal barrage in the Severn Estuary, UK. *Renewable Energy*, 35(7), 1455-1468.

<https://doi.org/10.1016/j.renene.2009.12.009>

Appendices

Appendix A

Delft3D is a 3-dimensional (3D) hydrodynamic model that was implemented in 2-dimensions (2D, depth-averaged) in the present research. This approach considers horizontal fluid motions in the x,y plane and neglects vertical motions. Two key equations are needed to describe the flow: the horizontal momentum equation derived from the Reynolds-averaged Navier-Stokes equations and the depth-averaged continuity equation. The 3D equations are described in detail in Lesser et al. (2004) and the 2D equations are briefly summarized here. The horizontal components of momentum, in the x - and y -directions, are given by:

$$\frac{\partial U}{\partial t} + U \frac{\partial U}{\partial x} + v \frac{\partial U}{\partial y} - fV = -\frac{1}{\rho_0} P_x + F_x + M_x + v_H \left(\frac{\partial^2 u}{\partial x^2} \right) \quad (1a)$$

$$\frac{\partial V}{\partial t} + U \frac{\partial V}{\partial x} + V \frac{\partial V}{\partial y} - fU = -\frac{1}{\rho_0} P_y + F_y + M_y + v_H \left(\frac{\partial^2 u}{\partial y^2} \right) \quad (1b)$$

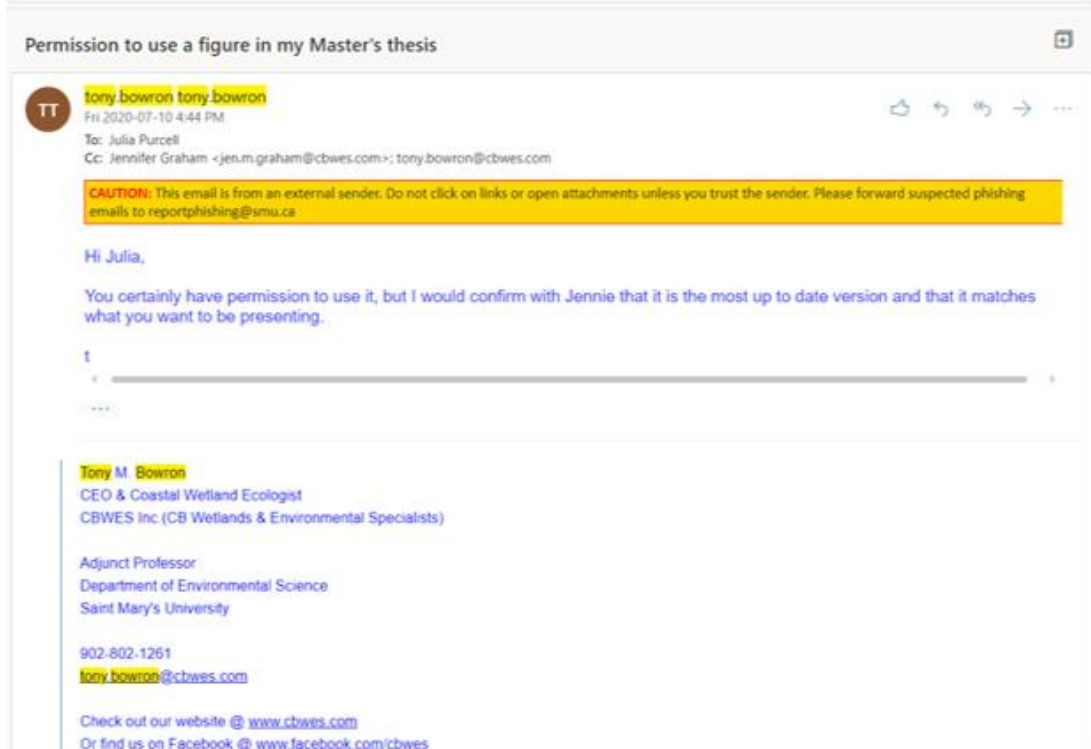
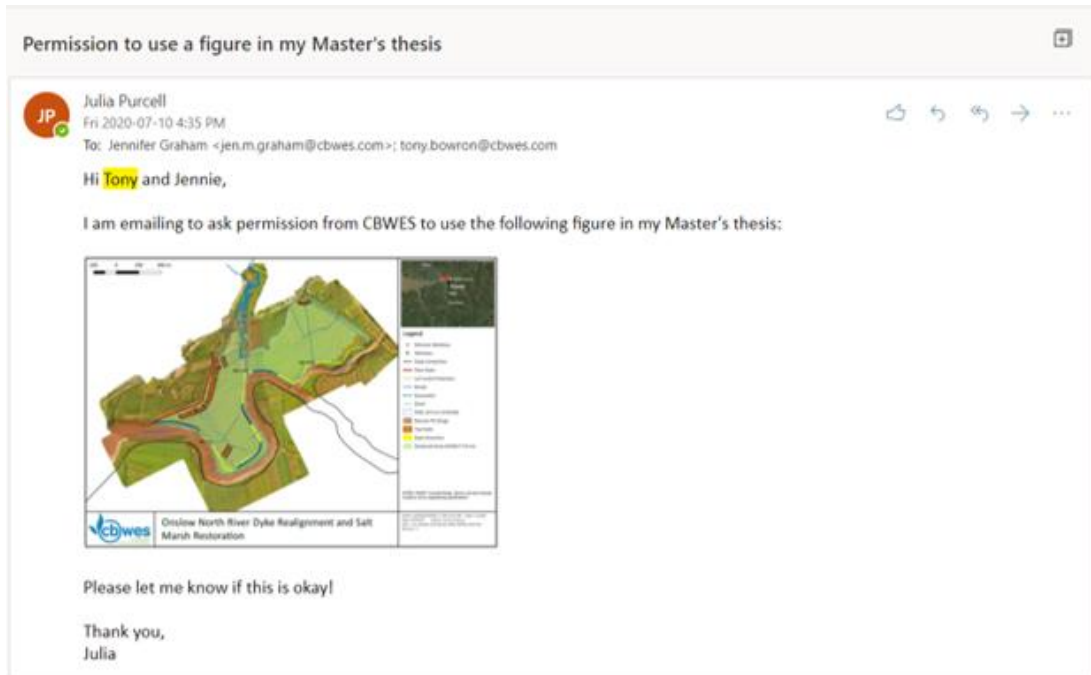
where U and V are Generalized Lagrangian Mean velocity components (u and v are Eulerian velocity components), t is time, f is the Coriolis coefficient, ρ_0 is the reference density of water, P is the horizontal pressure given by the Boussinesq approximation, F is Reynolds stress, M represents the force contributions due to external sources or sinks of momentum and v_H is the horizontal eddy viscosity (Lesser et al., 2004; McCombs et al., 2014). The depth-averaged continuity equation is expressed by:

$$\frac{\partial \zeta}{\partial t} + \frac{\partial(hU)}{\partial x} + \frac{\partial(hV)}{\partial y} = 0 \quad (2)$$

where ζ is the water surface elevation above reference datum and h is water depth (McCombs et al., 2014).

Appendix B

Permission via email from CBWES to include Figure 2.2 in this thesis document:




Permission via email from TransCoastal Adaptations to include Figure 1.1 in this thesis document:

Permission to use diagram created by TransCoastal as a figure in my thesis

JP Julia Purcell
Tue 2020-11-10 2:19 PM
To: Caytlyn McFadden

Hi Caytlyn,

I am emailing to ask for permission to use the following diagram in my thesis document:



Danika suggested I used this as a figure for my MR section, but I need documented permission (via email) from TransCoastal.

Thank you,
Julia

Permission to use diagram created by TransCoastal as a figure in my thesis

CM Caytlyn McFadden
Tue 2020-11-10 2:39 PM
To: Julia Purcell

Hi Julia,

Absolutely, sounds like it will be a great addition to your thesis. Feel free to use and reference TransCoastal. Sounds like your thesis is coming along well, good luck with the home stretch!

Caytlyn

...

Thank you! Thank you so much! Thanks a lot!

Are the suggestions above helpful? Yes No

Reply Forward

Appendix C

ADV 1 + OBS 1 and ADV 2 + OBS 2 deployment settings in Vector.

ADV Vector standard software parameters

Sampling rate: 16 Hz

Burst interval (s): 600

Number of samples per burst: 4800

Assumed duration (days): 4

Select "Use Advanced Settings"

ADV Vector advanced software parameters

Analog input 1: FAST

Select "Output power"

*Everything else left as default settings.

ADCP 1 deployment settings in AquaPro.

ADCP AquaPro standard software parameters

Frequency: 2 MHz

Profile interval (s): 10

Number of cells: 20

Cell size (m): 0.2

Assumed duration (days): 4

Select "Use Advanced Settings"

ADCP AquaPro advanced software parameters

Average interval (s): 10

Blanking Distance (m): 0.2

Compass upd. Rate (s): 10

Measurement load (%): 100

Measured Salinity (ppt): 30

Assumed duration (days): 4

*Everything else left as default settings.

ADCP 2 deployment settings in AquaPro.

ADCP AquaPro standard software parameters

Frequency: 1 MHz

Profile interval (s): 10

Number of cells: 10
Cell size (m): 0.5
Assumed duration (days): 4
Select "Use Advanced Settings"

ADCP AquaPro advanced software parameters
Average interval (s): 10
Blanking Distance (m): 0.4
Compass upd. Rate (s): 10
Measurement load (%): 87
Measured Salinity (ppt): 30
Assumed duration (days): 4

*Everything else left as default settings

ISCO 1 program settings.

Sample start times: Tide 1 = 13:40, Tide 2 = 02:00, Tide 3 = 14:30, Tide 4 = 02:55
Tube length = 20.5 meters
Sampling interval = 10 minutes
Sampling volume = 250 mL

ISCO 2 program settings.

Sample start times: Tide 1 = 14:25, Tide 2 = 02:45, Tide 3 = 15:15, Tide 4 = 03:40
Tube length = 20.1 meters
Sampling interval = 10 minutes
Sampling volume = 250 mL

Appendix D

The rows in this sample ADV file represent each data point and the columns represent the following:

Column 1	Burst counter	
Column 2	Ensemble counter	(1-65536)
Column 3	Velocity (Beam1 X East)	(m/s)
Column 4	Velocity (Beam2 Y North)	(m/s)
Column 5	Velocity (Beam3 Z Up)	(m/s)
Column 6	Amplitude (Beam1)	(counts)
Column 7	Amplitude (Beam2)	(counts)
Column 8	Amplitude (Beam3)	(counts)
Column 9	SNR (Beam1)	(dB)
Column 10	SNR (Beam2)	(dB)
Column 11	SNR (Beam3)	(dB)
Column 12	Correlation (Beam1)	(%)
Column 13	Correlation (Beam2)	(%)
Column 14	Correlation (Beam3)	(%)
Column 15	Pressure	(dbar)
Column 16	Analog input 1	
Column 17	Analog input 2	
Column 18	Checksum	(1=failed)

ADV_V101_1 - Notepad

File Edit Format View Help

1	1	0.2373	-0.1600	-0.1515	40	43	42	-0.4	0.4	0.0	12	10	12	0.115	199	0	0
1	2	0.1846	-0.5761	-0.0008	40	42	43	-0.4	0.0	0.4	1	16	7	0.117	200	0	0
1	3	0.4178	-0.8512	0.0669	41	43	41	0.0	0.4	-0.4	5	8	5	0.117	199	0	0
1	4	0.4525	-0.5069	0.0116	41	42	42	0.0	0.0	0.0	6	7	5	0.119	200	0	0
1	5	0.5479	0.0706	-0.0893	39	42	42	-0.9	0.0	0.0	14	9	19	0.116	200	0	0
1	6	0.0070	-0.1907	-0.0669	41	42	42	0.0	0.0	0.0	9	12	8	0.115	200	0	0
1	7	0.1969	0.3831	0.0722	41	42	42	0.0	0.0	0.0	12	4	9	0.119	199	0	0
1	8	-0.4225	-0.2478	-0.0009	41	40	43	0.0	-0.9	0.4	3	13	19	0.116	200	0	0
1	9	-0.3833	-0.8472	0.0359	41	42	43	0.0	0.0	0.4	5	16	16	0.119	200	0	0
1	10	0.7042	-0.1124	0.0694	40	42	42	-0.4	0.0	0.0	18	2	4	0.118	200	0	0
1	11	0.2169	0.8126	-0.0720	40	43	42	-0.4	0.4	0.0	9	7	10	0.118	199	0	0
1	12	0.8394	0.7785	0.0626	41	42	43	0.0	0.0	0.4	7	10	14	0.119	200	0	0
1	13	-0.1865	-0.5362	-0.0373	41	41	42	0.0	-0.4	0.0	4	12	20	0.116	199	0	0
1	14	0.4520	0.3238	0.0141	42	41	42	0.4	-0.4	0.0	1	7	8	0.118	200	0	0
1	15	-0.0687	0.5628	0.0165	40	43	43	-0.4	0.4	0.4	9	8	12	0.118	200	0	0
1	16	-0.7972	0.4170	0.0973	40	42	41	-0.4	0.0	-0.4	8	12	21	0.117	200	0	0
1	17	-0.1616	0.2826	0.0048	39	41	42	-0.9	-0.4	0.0	1	9	15	0.114	199	0	0
1	18	-0.3128	-0.3862	0.0597	40	41	42	-0.4	-0.4	0.0	7	8	11	0.120	199	0	0
1	19	-0.4899	0.0729	0.0888	41	42	41	0.0	0.0	-0.4	8	6	6	0.116	200	0	0
1	20	-0.3727	-0.9146	-0.0052	40	41	42	-0.4	-0.4	0.0	7	8	3	0.119	200	0	0
1	21	0.0471	-0.0100	-0.0591	41	42	43	0.0	0.0	0.4	7	4	16	0.119	200	0	0
1	22	-0.3014	0.7454	-0.0229	40	42	42	-0.4	0.0	0.0	6	7	11	0.119	199	0	0
1	23	-0.4488	-0.6208	-0.0412	42	42	43	0.4	0.0	0.4	4	6	9	0.117	200	0	0
1	24	-0.3911	-0.3656	-0.1565	40	42	41	-0.4	0.0	-0.4	6	2	7	0.120	200	0	0
1	25	0.9478	-0.0045	-0.0403	40	42	43	-0.4	0.0	0.4	2	14	14	0.115	199	0	0
1	26	-0.3464	-0.5915	0.0329	39	42	42	-0.9	0.0	0.0	7	14	8	0.118	200	0	0
1	27	0.5285	-0.1698	0.0590	41	43	43	0.0	0.4	0.4	3	8	9	0.118	200	0	0
1	28	-0.3883	-0.0632	-0.0309	40	41	42	-0.4	-0.4	0.0	18	6	8	0.119	200	0	0
1	29	0.2252	-0.8294	0.0456	41	42	43	0.0	0.0	0.4	14	5	8	0.118	200	0	0
1	30	-0.4416	-0.2542	-0.0470	41	43	43	0.0	0.4	0.4	13	8	14	0.118	199	0	0
1	31	-0.3391	-0.3902	0.0680	42	42	43	0.4	0.0	0.4	5	20	9	0.119	200	0	0
1	32	-0.2018	0.1713	-0.1043	41	42	40	0.0	0.0	-0.9	16	4	8	0.117	200	0	0
1	33	-0.7654	0.5408	-0.0125	41	41	42	0.0	-0.4	0.0	5	5	9	0.120	199	0	0
1	34	0.2233	-0.7131	0.0060	40	41	43	-0.4	-0.4	0.4	21	4	3	0.117	199	0	0
1	35	0.3522	-1.0327	0.0462	41	43	43	0.0	0.4	0.4	12	4	6	0.119	199	0	0
1	36	0.4072	-0.0258	0.1047	41	42	42	0.0	0.0	0.0	9	14	1	0.119	199	0	0
1	37	0.2001	0.3057	0.1396	41	43	42	0.0	0.4	0.0	18	8	4	0.119	199	0	0
1	38	-0.4488	0.2006	0.0753	40	42	42	-0.4	0.0	0.0	14	6	14	0.120	200	0	0
1	39	-0.2447	-0.4100	0.0716	41	42	43	0.0	0.0	0.4	3	14	14	0.119	200	0	0

Windows (CRLF) Ln 1, Col 1 100%

Appendix E

```
% adv_postprocessing.m
% Julia Purcell, October 22, 2020

% It is important to note that this script only works with a .dat file that
% contains data for one full tide only. It will not calculate the variables
% you desire properly if data for more than one tide is included in the
% .dat file that you want to import. Run the script once for each
% individual tide!

% Another thing to note is that the only lines you need to change in this
% script each time you run it (if .dat files are different) are line 23
% (the name of the .dat file you are importing) and lines 367 and 368 (the
% equations you get from your OBS calibrations). There are two lines
% because there are two OBS instruments. Only use one line at a time,
% depending on your calibration equation.

% Importing ADV Data and Filtering
%
=====

% Import the .dat file which contains the raw ADV data - change file name as necessary.
rawdata = importdata('ADV_V101_2.dat');

filter1 = rawdata(:,9)<8; % Searches for any row that has a SNR (beam 1) value of less
than 8 dB.
rawdata(filter1,:) = []; % Removes the rows that apply to the condition above.

filter2 = rawdata(:,10)<8; % Searches for any row that has a SNR (beam 2) value of less
than 8 dB.
rawdata(filter2,:) = []; % Removes the rows that apply to the condition above.

filter3 = rawdata(:,11)<8; % Searches for any row that has a SNR (beam 3) value of less
than 8 dB.
rawdata(filter3,:) = []; % Removes the rows that apply to the condition above.

% Keeps all data-related columns from the rawdata variable (velocity in m/s).
advdata = [rawdata(:,1) rawdata(:,3:16)];

% Calculate Resolved Horizontal Velocity and Magnitude
%
=====
```

```

% XYZ velocities with their associated burst number.
vel = [advdata(:,1) advdata(:,2:4)];

% Resolved horizontal velocity.
RHV = [vel(:,1) sqrt((vel(:,2).^2)+(vel(:,3).^2))];

% Magnitude
mag = [vel(:,1) sqrt((vel(:,2).^2)+(vel(:,3).^2)+(vel(:,4).^2))];

% Calculate 5-Minute Means, Standard Errors, and Standard Deviations
%
=====

% Mean RHV calculation.
a = unique(RHV(:,1)); % Identifying all unique values in column 1 of 'RHV' (identifying
all rows with the same burst number).
meanRHV = zeros(length(a),2); % Creating a zero matrix with 2 columns and as many
rows as the length of the previous variable (this is a matrix "place holder").
meanRHV(:,1)=a; % Occupies the first column of 'meanRHV' with 'a' values, leaving
one column of zeros left to be filled in.
for idx=1:length(a) % For loop condition statement.
    meanRHV(idx,2)=mean(RHV(RHV(:,1)==a(idx),2)); % Calculating the mean of
'RHV' values for each burst and replacing the zeros in column 2 with those mean values.
end % Ending the loop.

% I have hidden the standard error/deviation calculations in the next line.
% Just click the plus sign to expand it.
% {
% Mean RHV Standard Deviation.
a = unique(RHV(:,1));
stdRHV = zeros(length(a),2);
stdRHV(:,1)=a;
for idx=1:length(a)
    stdRHV(idx,2)=std(RHV(RHV(:,1)==a(idx),2));
end

% Mean RHV Standard Error.
a = unique(RHV(:,1));
steRHV = zeros(length(a),2);
steRHV(:,1)=a;
for idx=1:length(a)

steRHV(idx,2)=std(RHV(RHV(:,1)==a(idx),2))/sqrt(length(RHV(RHV(:,1)==a(idx),2)));
end

```

```

steRHV = steRHV(:,2);
steRHV = transpose(steRHV);
% }

% Mean magnitude calculation.
a = unique(mag(:,1));
meanmag = zeros(length(a),2);
meanmag(:,1)=a;
for idx=1:length(a)
    meanmag(idx,2)=mean(mag(mag(:,1)==a(idx),2));
end

% Mean x velocity calculation.
a = unique(vel(:,1));
meanx = zeros(length(a),2);
meanx(:,1)=a;
for idx=1:length(a)
    meanx(idx,2)=mean(vel(vel(:,1)==a(idx),2));
end

% Mean y velocity calculation.
a = unique(vel(:,1));
meany = zeros(length(a),2);
meany(:,1)=a;
for idx=1:length(a)
    meany(idx,2)=mean(vel(vel(:,1)==a(idx),3));
end

% Mean z velocity calculation.
a = unique(vel(:,1));
meanz = zeros(length(a),2);
meanz(:,1)=a;
for idx=1:length(a)
    meanz(idx,2)=mean(vel(vel(:,1)==a(idx),4));
end

% Mean signal strength (beam 1) calculation.
a = unique(advdata(:,1));
sig1 = zeros(length(a),2);
sig1(:,1)=a;
for idx=1:length(a)
    sig1(idx,2)=mean(advdata(advdata(:,1)==a(idx),5));
end

% Mean signal strength (beam 2) calculation.
a = unique(advdata(:,1));

```



```

sig2 = zeros(length(a),2);
sig2(:,1)=a;
for idx=1:length(a)
    sig2(idx,2)=mean(advdata(advdata(:,1)==a(idx),6));
end

% Mean signal strength (beam 3) calculation.
a = unique(advdata(:,1));
sig3 = zeros(length(a),2);
sig3(:,1)=a;
for idx=1:length(a)
    sig3(idx,2)=mean(advdata(advdata(:,1)==a(idx),7));
end

% Mean SNR (beam 1) calculation.
a = unique(advdata(:,1));
SNR1 = zeros(length(a),2);
SNR1(:,1)=a;
for idx=1:length(a)
    SNR1(idx,2)=mean(advdata(advdata(:,1)==a(idx),8));
end

% Mean SNR (beam 2) calculation.
a = unique(advdata(:,1));
SNR2 = zeros(length(a),2);
SNR2(:,1)=a;
for idx=1:length(a)
    SNR2(idx,2)=mean(advdata(advdata(:,1)==a(idx),9));
end

% Mean SNR (beam 3) calculation.
a = unique(advdata(:,1));
SNR3 = zeros(length(a),2);
SNR3(:,1)=a;
for idx=1:length(a)
    SNR3(idx,2)=mean(advdata(advdata(:,1)==a(idx),10));
end

% Mean correlation (beam 1) calculation.
a = unique(advdata(:,1));
cor1 = zeros(length(a),2);
cor1(:,1)=a;
for idx=1:length(a)
    cor1(idx,2)=mean(advdata(advdata(:,1)==a(idx),11));
end

```

```

% Mean correlation (beam 2) calculation.
a = unique(advdata(:,1));
cor2 = zeros(length(a),2);
cor2(:,1)=a;
for idx=1:length(a)
    cor2(idx,2)=mean(advdata(advdata(:,1)==a(idx),12));
end

% Mean correlation (beam 3) calculation.
a = unique(advdata(:,1));
cor3 = zeros(length(a),2);
cor3(:,1)=a;
for idx=1:length(a)
    cor3(idx,2)=mean(advdata(advdata(:,1)==a(idx),13));
end

% Mean pressure calculation. Important for determining when high tide is and creating
the RHT variable!
a = unique(advdata(:,1));
pres = zeros(length(a),2);
pres(:,1)=a;
for idx=1:length(a)
    pres(idx,2)=mean(advdata(advdata(:,1)==a(idx),14));
end

% Mean OBS signal calculation.
a = unique(advdata(:,1));
obs = zeros(length(a),2);
obs(:,1)=a;
for idx=1:length(a)
    obs(idx,2)=mean(advdata(advdata(:,1)==a(idx),15));
end

% Matrix compiled of all 5-minute mean data from calculations above.
advmeandata = [meanRHV(:,1) meanx(:,2) meany(:,2) meanz(:,2) meanRHV(:,2)
sig1(:,2) sig2(:,2) sig3(:,2) SNR1(:,2) SNR2(:,2) SNR3(:,2) cor1(:,2) cor2(:,2) cor3(:,2)
pres(:,2) obs(:,2)];

% Calculate Turbulent Kinetic Energy (TKE)
%
=====

% Turbulence x-component.
a = [vel(:,1) vel(:,2)]; % Creating two columns with all bursts and all x-velocities.

```

```

turbx = zeros(length(a),3); % Creating a zero matrix with 3 columns and as many rows
as the length of the previous variable (this is a matrix "place holder").
turbx(:,1:2) = a; % Occupies the first two columns of 'turbx' with 'a' values, leaving one
column of zeros left to be filled in.
for idx=1:length(meanx) % Condition statement = For 'idx' values from 1 to length of
'meanx'...
    for ind=meanx(idx,1) % Condition statement = For 'ind' values that equal the row
number in 'meanx'...
        turbx(turbx(:,1)==ind,3) = meanx(meanx(:,1)==ind,2); % Calculating the average of
each burst and putting the values in column 3.
    end % Ends the nested for loop.
end % Ends the for loop.

turbx = [turbx(:,1) turbx(:,2)-turbx(:,3)]; % Calculation of turbulent x-component.
tdevx = [turbx(:,1) turbx(:,2).^2]; % Calculation of turbulent deviation (for stress
calculations).

% Turbulence y-component.
a = [vel(:,1) vel(:,3)];
turby = zeros(length(a),3);
turby(:,1:2) = a;
for idx=1:length(meany)
    for ind=meany(idx,1)
        turby(turby(:,1)==ind,3) = meany(meany(:,1)==ind,2);
    end
end

turby = [turby(:,1) turby(:,2)-turby(:,3)];
tdevy = [turby(:,1) turby(:,2).^2];

% Turbulence z-component.
a = [vel(:,1) vel(:,4)];
turbz = zeros(length(a),3);
turbz(:,1:2) = a;
for idx=1:length(meanz)
    for ind=meanz(idx,1)
        turbz(turbz(:,1)==ind,3) = meanz(meanz(:,1)==ind,2);
    end
end

turbz = [turbz(:,1) turbz(:,2)-turbz(:,3)];
tdevz = [turbz(:,1) turbz(:,2).^2];

% Compiling all turbulent calculations.
turball = [turbx turby(:,2) turbz(:,2)]; % Col 1 = burst #, Col 2 = turbulent x-component,
Col 3 = turbulent y-component, Col 4 = turbulent z-component.

```

```
tdevall = [tdevx tdevy(:,2) tdevz(:,2)]; % Col 1 = burst #, Col 2 = turbulent x deviation,
Col 3 = turbulent y deviation, Col 4 = turbulent z deviation.
```

```
% TKE calculations.
```

```
TKE = [tdevall(:,1) 0.5*1025*(tdevall(:,2)+tdevall(:,3)+tdevall(:,4))];
```

```
% Mean TKE.
```

```
a = unique(TKE(:,1));
```

```
meanTKE = zeros(length(a),2);
```

```
meanTKE(:,1)=a;
```

```
for idx=1:length(a)
```

```
    meanTKE(idx,2)=mean(TKE(TKE(:,1)==a(idx),2));
```

```
end
```

```
% TKE horizontal component.
```

```
horTKE = [tdevall(:,1) 0.5*1025*(tdevall(:,2)+tdevall(:,3))];
```

```
% Mean horizontal TKE.
```

```
a = unique(horTKE(:,1));
```

```
meanhorTKE = zeros(length(a),2);
```

```
meanhorTKE(:,1)=a;
```

```
for idx=1:length(a)
```

```
    meanhorTKE(idx,2)=mean(horTKE(horTKE(:,1)==a(idx),2));
```

```
end
```

```
% TKE vertical component.
```

```
verTKE = [tdevall(:,1) 0.5*1025*(tdevall(:,2))];
```

```
% Mean vertical TKE.
```

```
a = unique(verTKE(:,1));
```

```
meanverTKE = zeros(length(a),2);
```

```
meanverTKE(:,1)=a;
```

```
for idx=1:length(a)
```

```
    meanverTKE(idx,2)=mean(verTKE(verTKE(:,1)==a(idx),2));
```

```
end
```

```
% Calculate Reynolds' Stresses
```

```
%
```

```
=====
```

```
% Reynolds' stress and shear stress calculations are hidden in the next
```

```
% line. Click the plus sign to expand it.
```

```
% {
```

```
stress2D = [advdata(:,1) -1025*turbx(:,2).*turbz(:,2)]; % Calculating 2D stress.
```

```

% Mean 2D Stress Calculation
a = unique(stress2D(:,1));
meanstress2D = zeros(length(a),2);
meanstress2D(:,1)=a;
for idx=1:length(a)
    meanstress2D(idx,2)=mean(stress2D(stress2D(:,1)==a(idx),2));
end

stress3D = [advdata(:,1)
1025*sqrt((((turbx(:,2).*turbz(:,2)).^2)+((turby(:,2).*turbz(:,2)).^2)))]); % Calculating 3D
stress.

% Mean 3D Stress Calculation
a = unique(stress3D(:,1));
meanstress3D = zeros(length(a),2);
meanstress3D(:,1)=a;
for idx=1:length(a)
    meanstress3D(idx,2)=mean(stress3D(stress3D(:,1)==a(idx),2));
end

shear = [advdata(:,1) -1025*(turbx(:,2).*turby(:,2))]; % Calculating shear stress acting on
the bed.

% Mean Shear Stress Calculation
a = unique(shear(:,1));
meanshear = zeros(length(a),2);
meanshear(:,1)=a;
for idx=1:length(a)
    meanshear(idx,2)=mean(shear(shear(:,1)==a(idx),2));
end
% }

% Calculate Shear Velocity
%
=====

xy = [turbx(:,1) turbx(:,2).*turby(:,2)];

a = unique(verTKE(:,1));
meanxy = zeros(length(a),2);
meanxy(:,1)=a;
for idx=1:length(a)
    meanxy(idx,2)=mean(xy(xy(:,1)==a(idx),2)); % Average xy values in m2/s2.
end

```

```

meanxy(:,2) = abs(meanxy(:,2));
meanshearvel = sqrt(meanxy(:,2));

```

```

% Calculate Time Relative to High Tide (RHT)
%

```

```

=====
nrows = size(pres); % Determines the size of the 'pres' variable.
nrows = nrows(1,1); % Assigns 'nrows' variable to the number of rows.
[~,row] = max(pres(:,2)); % Finds the maximum depth value in column 1 and provides
the row it belongs to.

```

```

before = 0:-10:(row-1)*-10; % Time increments before high tide.
before = fliplr(before); % Flips matrix from left to right.
before = before'; % Transposes the matrix.
after = 10:10:(nrows-row)*10; % Time increments after high tide.
after = after'; % Transposes the matrix.

```

```

RHT = [before; after]; % Creation of RHT x-axis variable.

```

```

% Calculate Suspended Sediment Concentration (SSC)
%

```

```

=====
counts = advdata(:,15);
SSC = [advdata(:,1) (6e-14)*(counts.^3)+(6e-9)*(counts.^2)+0.0003*counts-0.0541]; %
Use this calibration equation for ADV (V1) - this equation will change per deployment
site.
%SSC = [advdata(:,1) (8e-14)*(counts.^3)-(8e-9)*(counts.^2)+0.0003*counts-0.0458]; %
Use this calibration equation for ADV (V2) - this equation will change per deployment
site.

```

```

% Mean SSC calculation.
a = unique(SSC(:,1));
meanSSC = zeros(length(a),2);
meanSSC(:,1)=a;
for idx=1:length(a)
    meanSSC(idx,2)=mean(SSC(SSC(:,1)==a(idx),2));
end

```

Appendix F

Delft3D run list.

- r100 = r020 from Ryan (original model parameters and observation points).
- r101 = copy of r100 with new observation points (2 ADVs, 2 ADCPs, 2 ISCOs, and 1 level logger). MDF file used is 'julia_thesis.mdf', not 'cbwes.mdf'.
- r102 = copy of r101 with new boundary conditions in terms of water level (first water level check).
- r103 = copy of r102 (test to make sure Delft3D was working).
- r104 = copy of r103 with changes to the boundary conditions in terms of water level (trying to make model output match with observed water levels) and additional "test" observation points.
- r105 = copy of r104 with new 'rivers.dis' file (discharges from Environment Canada).
- r106 = copy of r105 but only outputting results from last four tides with a shorter time interval (10 minutes).
- r107 = copy of r105 but with a new depth file that was created by assigning the maximum point of the DEM to each grid cell instead of averaging the points. The new depth file is called 'Grid_009fix3.dep'. I also added thin dams in the upper left part of the grid in hopes of preventing flooding over land as the tidal boundary extends over land. Update (19/02/2019): This run did not finish. See diagnostic file.
- r108 = copy of r107 but the thin dams have been removed. Update (20/02/2019): This run did not finish. See diagnostic file.
- r109 = copy of r105 but with a new depth file that was created using a new DEM with new dyke heights and widths burned into it and by assigning the maximum point of the DEM to each grid cell. The new depth file is called 'burneddykes_maxpoint.dep'. Update (22/02/2019): This run did not finish. See diagnostic file.
- r110 = copy of r105 but with a new depth file that was created using a new DEM with new dyke heights and widths burned into it and by assigning the closest point of the DEM to each grid cell. The new depth file is called 'burneddykes_closestpoint.dep'. Update (22/02/2019): This run did not finish. See diagnostic file.
- r111 = copy of r105 but with a new depth file that was created using a new DEM with new dyke heights and widths burned into it and by assigning the maximum point of the DEM to each grid cell. The new depth file is called 'burneddykes_maxpoint.dep'. I also altered the grid slightly for this run. The grid file is called 'Grid_009fix_julia.grd'. Update (22/02/2019): This run did not finish. See diagnostic file. This was probably because I changed the grid (removed some grid cells) where the open boundary was supposed to be.
- r112 = copy of r105 but with a new depth file that was created using a new DEM with new dyke heights and widths burned into it and by assigning the maximum point of the DEM to each grid cell. The new depth file is called 'burneddykes_maxpoint.dep'. The difference here is that I smoothed out portions

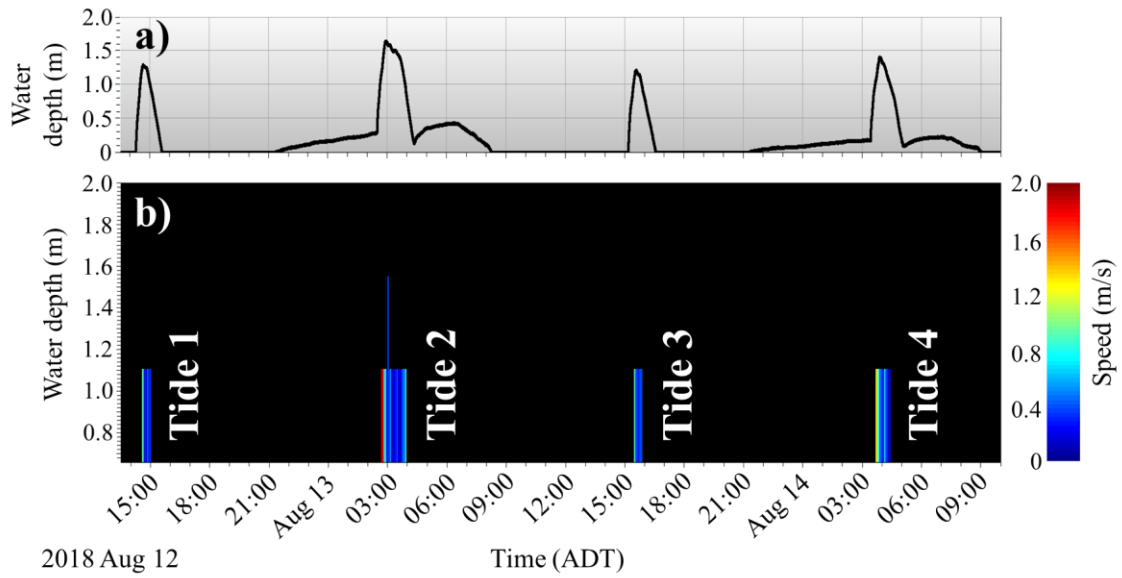
- of the depth file near the open boundary to make everything smoother and more fluid.
- r113 = copy of r112 but I multiplied all depth points in the depth file by -1, as per Ryan's instructions from two summers ago. This run was stopped prematurely by me because the rivers didn't look right. It may have been due to the averaging method I chose (maximum point).
- r114 = copy of r105 but with a new depth file that was created using a new DEM with new dyke heights and widths burned into it and by assigning an averaged DEM point value to each grid cell. The new depth file is called 'burnedykes_avg.dep'. I have also shortened the tidal boundary so that it does not extend over land in the north-west corner of the existing grid. Update (27/02/2019): The rivers looked back to normal, but the west side of the grid was flooding again, meaning the averaging method does not resolve the dykes well enough.
- r115 = copy of r114 but with a new depth file that was created using a new DEM with new dyke heights and widths burned into it. It also was interpolated using two different averaging methods: (1) max point averaging was used on the portion of the DEM west of Hwy102, and (2) regular averaging was used on the portion of the DEM east of Hwy102. This was done to assure that the rivers look okay and that the dykes are resolved enough.
- r116 = copy of r115 but with a new depth file (the new 2018 bathymetry) and a new rivers file that gives the Salmon River slightly greater discharge values. This is the first run attempt with the 2018 bathymetry DEM.
- r117 = copy of r116 but with adjusted water levels at the tidal boundary (aug2018.bct file) to help match my observed data better. I adjusted it by -0.2 meters.
- r118 = copy of r117 but with adjusted water levels at the tidal boundary (aug2018.bct file) to help match my observed data better. I adjusted it by +0.1 meters.
- r119 = copy of r118 but with a different depth file (the old 2013 bathymetry). This run will be compared to r118 for my thesis.
- r120 = copy of r118, but with a Chezy value of 92 instead of the default 65.
- r121 = copy of r120, but with adjusted water levels at the tidal boundary (aug2018.bct file) to help match my observed data better. I adjusted it by subtracting 0.43 meters from the previous WL values.
- r122 = copy of r119, but with a new depth file ('2018DEM_MaxPoint_Neg.dep) that now has LiDAR data from 2013 where the foreshore salt marshes are in the system (in order to bring it down to surface elevation instead of elevation of the top of vegetation). Chezy value is left at default of 65. Water levels remain unadjusted from r119.
- r123 = copy of r122, but with a new depth file ('2018DEM_MaxPoint_Avg_Neg.dep). The reason for this run is to test the rivers and how far they flow with different averaging techniques in QUICKIN. For this run, the depth file west of Hwy 102 was averaged using the maximum value and east of Hwy 102 was averaged using the average value.
- r124 = copy of r123, everything the same except for the interval of map results. I changed it from 60 minutes to 30 minutes so maps would be produced more frequently. The start time of map results was also changed to "12 08 2018 00 00 00". The end time stayed the same at "14 08 2018 10 00 00".

- r125 = copy of r125, but with new depth file ('2013DEM_MaxPoint_Avg_Neg.dep'). This run will be compared to r124 for my thesis.
- r126 = copy of r124, but with a Chezy value of 92 instead of the default 65.
- r127 = copy of r126, but with adjusted water levels at the tidal boundary (aug2018.bct file) to help match my observed data better. I adjusted it by subtracting 0.33 meters from the previous WL values.
- r128 = copy of r124, but with a history interval of 1 minute instead of the default (10 minutes).
- r129 = copy of r125, but with a history interval of 1 minute instead of the default (10 minutes).
- r130 = copy of r126, but with a history interval of 1 minute instead of the default (10 minutes).
- r131 = copy of r127, but with a history interval of 1 minute instead of the default (10 minutes).
- r132 = copy of r128, but changed the depth file to '2018DEM_Breached_MaxPoint_Neg.dep'. This is the first model run with the breach scenario.
- r133 = copy of r132, but with water levels increased by an increment of 0.05m, making the upper bounds of tidal heights approximately 9.65m.
- r134 = copy of r133, but with water levels increased by another increment of 0.05m, making the upper bounds of tidal heights approximately 9.7m.
- r135 = copy of r134, but with water levels increased by another increment of 0.05m, making the upper bounds of tidal heights approximately 9.75m.
- r136 = copy of r135, but with water levels increased by another increment of 0.05m, making the upper bounds of tidal heights approximately 9.8m.
- r137 = copy of r136, but with water levels increased by another increment of 0.05m, making the upper bounds of tidal heights approximately 9.85m.
- r138 = copy of r137, but with water levels increased by another increment of 0.05m, making the upper bounds of tidal heights approximately 9.9m.
- r139 = copy of r138, but with water levels increased by another increment of 0.05m, making the upper bounds of tidal heights approximately 9.95m.
- r140 = copy of r132, but the depth file has been changed to '2018DEM_Breached_RemovedAboiteaux_MaxPoint_Neg.dep'. This was a necessary fix to the 2018 DEM because we want not only the dykes to be breached, but the aboiteaux (3 of them) removed as well.
- r141 = copy of r140, but the depth file has been changed to '2018DEM_Breached_RemovedAboiteaux_MaxPoint_Neg_NorthRiverfix.dep'. In the previous runs it seems there is a barrier or a disconnect in the North River upstream of the CN Rail bridge, preventing the river water from meeting the tidal water, so I attempted to alter the depth file in order to allow the river water to flow through properly.
- r142 = copy of r141, but the depth file has been changed to '2018DEM_Breached_RemovedAboiteaux_MaxPoint_Neg_NorthRiverfix_Culverrtfix.dep'. For this run, I smoothed out the North River a bit so that there wasn't any water pooling where it shouldn't be, I smoothed out a part of the Salmon River just upstream of the confluence so that water didn't pool where it shouldn't

- (this was the boundary between the 2018 HydroSurveyor data and the 2013 LiDAR data), and I burned the DEM where the culvert exists in McCurdy's Brook, hoping tidal water will now pass through (if the tide is high enough).
- r143 = copy of r142, but the depth file has been changed to '2018DEM_Breached_RemovedAboiteaux_MaxPoint_Neg_NorthRiverfix2_Culvertfix.dep'. I smoothed out the North River even more so water wouldn't artificially build up like it did slightly in r142.
- r144 = copy of r133, but the depth file has been changed to '2018DEM_Breached_RemovedAboiteaux_MaxPoint_Neg_NorthRiverfix2_Culvertfix.dep'. For this run, the upper bounds of tidal heights will be approximately 9.65m.
- r145 = copy of r134, but the depth file has been changed to '2018DEM_Breached_RemovedAboiteaux_MaxPoint_Neg_NorthRiverfix2_Culvertfix.dep'. For this run, the upper bounds of tidal heights will be approximately 9.7m.
- r146 = copy of r135, but the depth file has been changed to '2018DEM_Breached_RemovedAboiteaux_MaxPoint_Neg_NorthRiverfix2_Culvertfix.dep'. For this run, the upper bounds of tidal heights will be approximately 9.75m.
- r147 = copy of r136, but the depth file has been changed to '2018DEM_Breached_RemovedAboiteaux_MaxPoint_Neg_NorthRiverfix2_Culvertfix.dep'. For this run, the upper bounds of tidal heights will be approximately 9.8m.

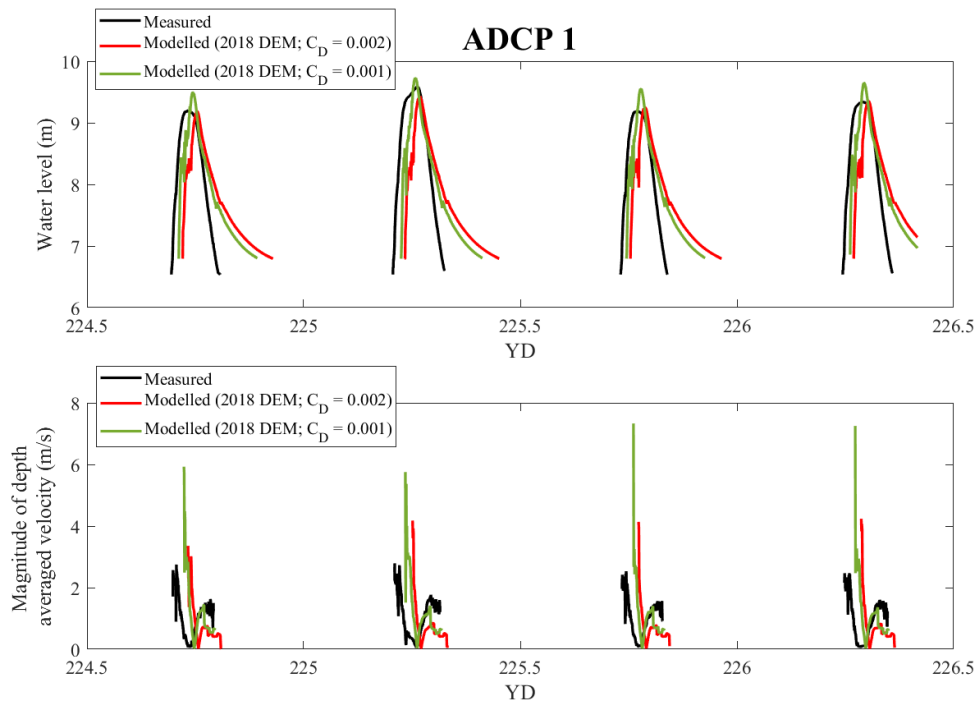
Appendix G

Water depth (a) and speed (b) measured at the ADCP 2 location for all four tides.

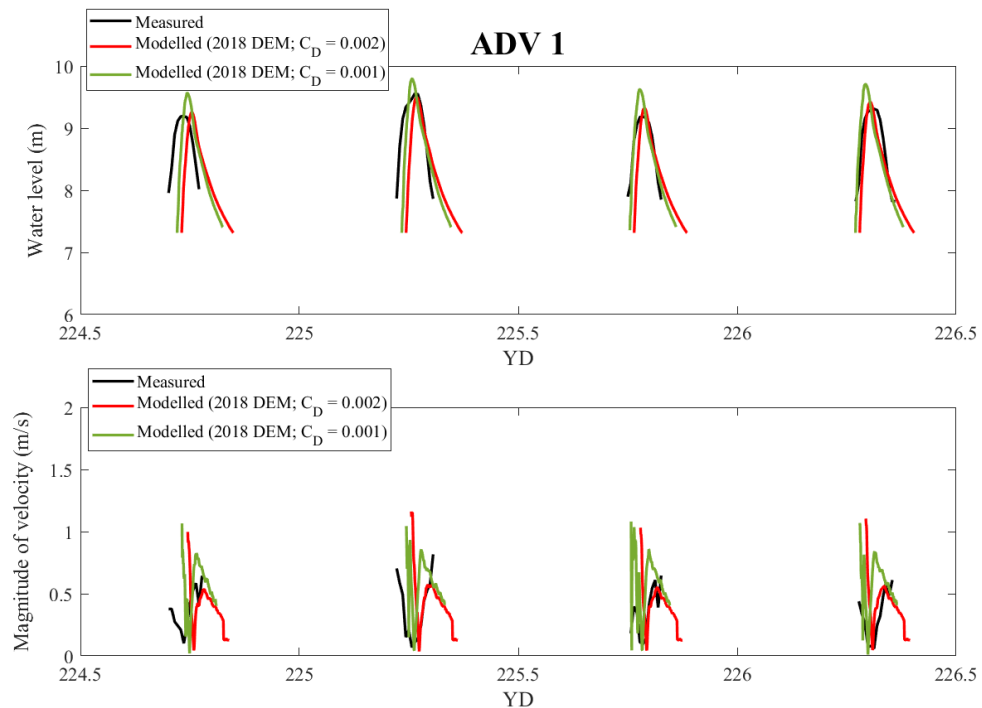


Appendix H

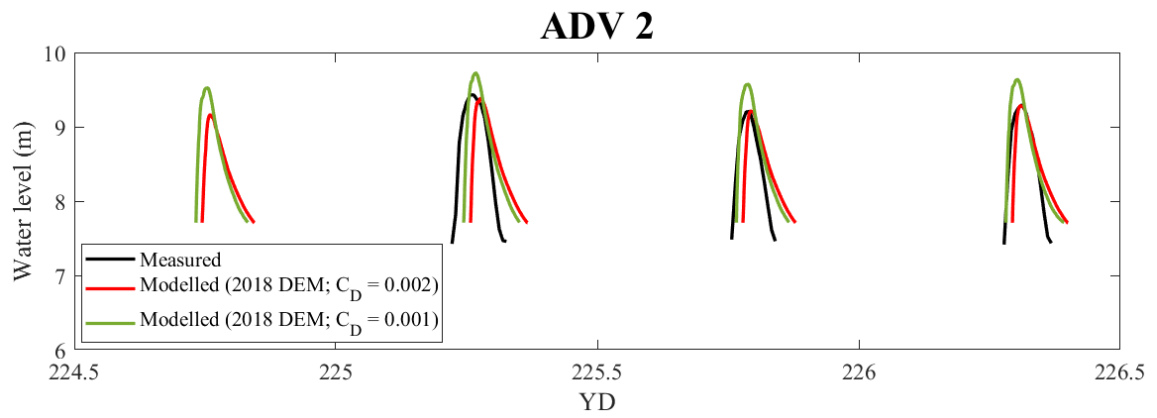
Measured and modelled water levels and velocities at ADCP 1 prior to recalibration.



Measured and modelled water levels and velocities at ADV 1 + OBS 1 prior to recalibration.

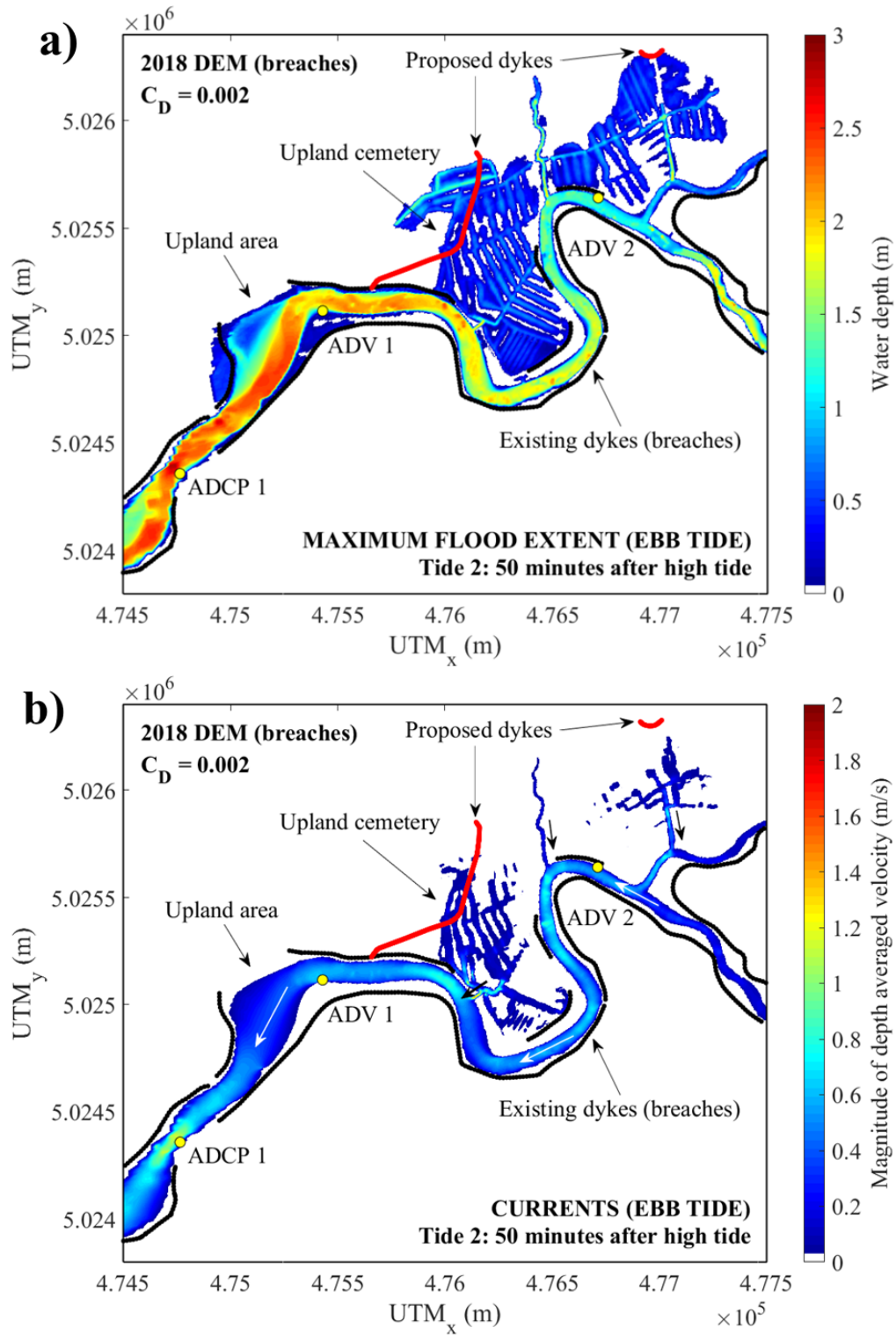


Measured and modelled water levels and velocities at ADV 2 + OBS 2 prior to recalibration.

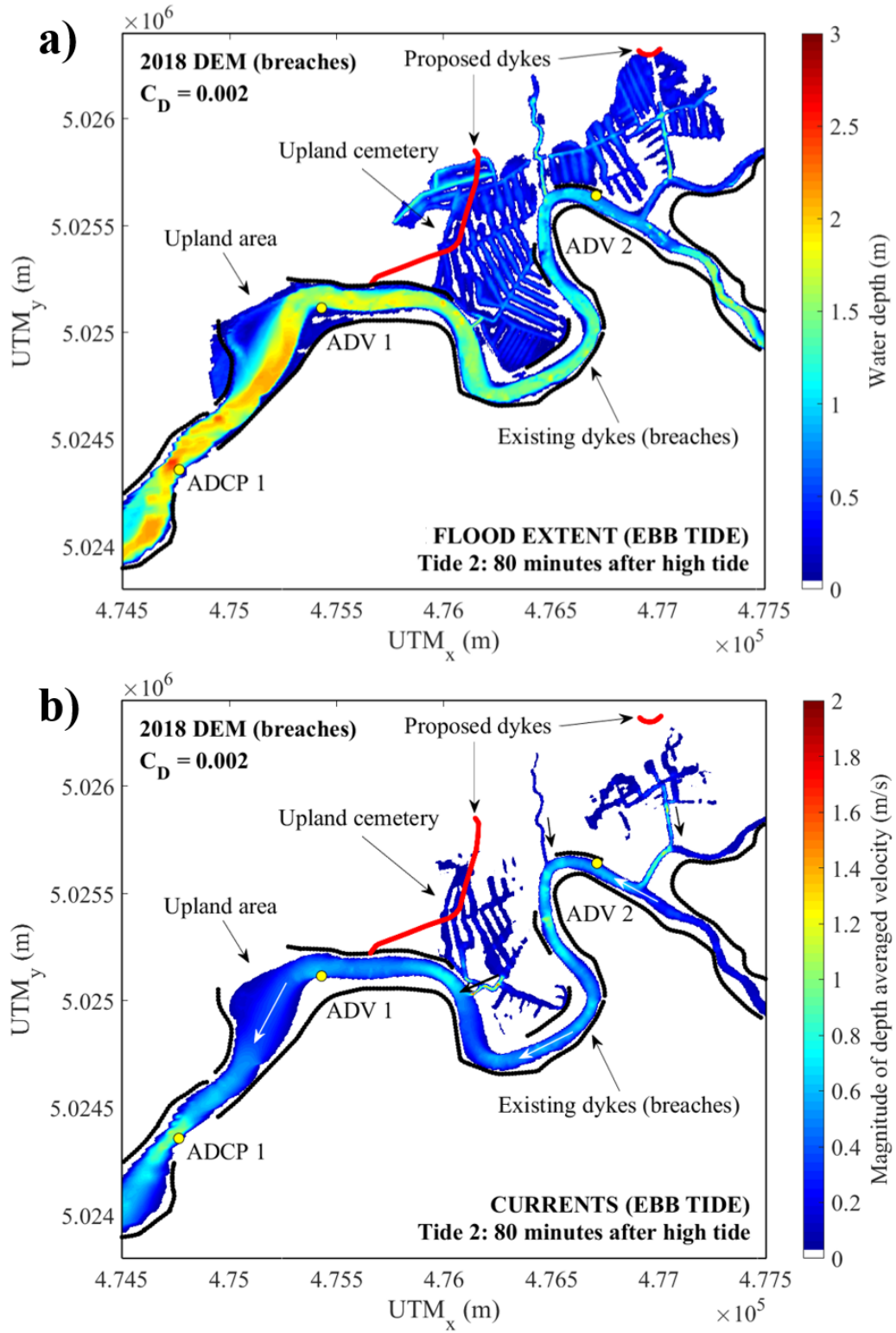


Appendix I

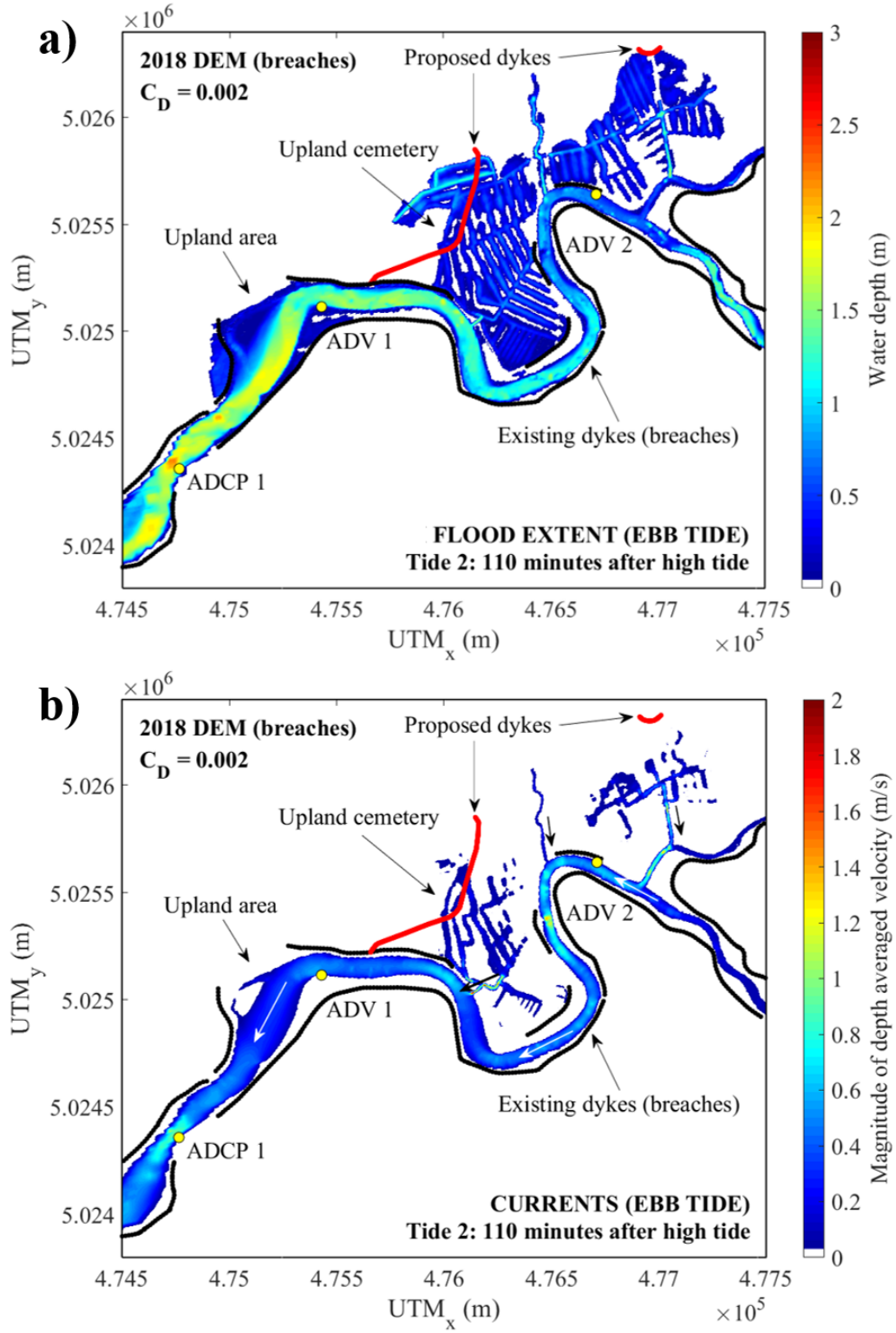
Modelled maximum flood extent and currents 50 minutes after high tide for Tide 2.



Modelled flood extent and currents 80 minutes after high tide for Tide 2.

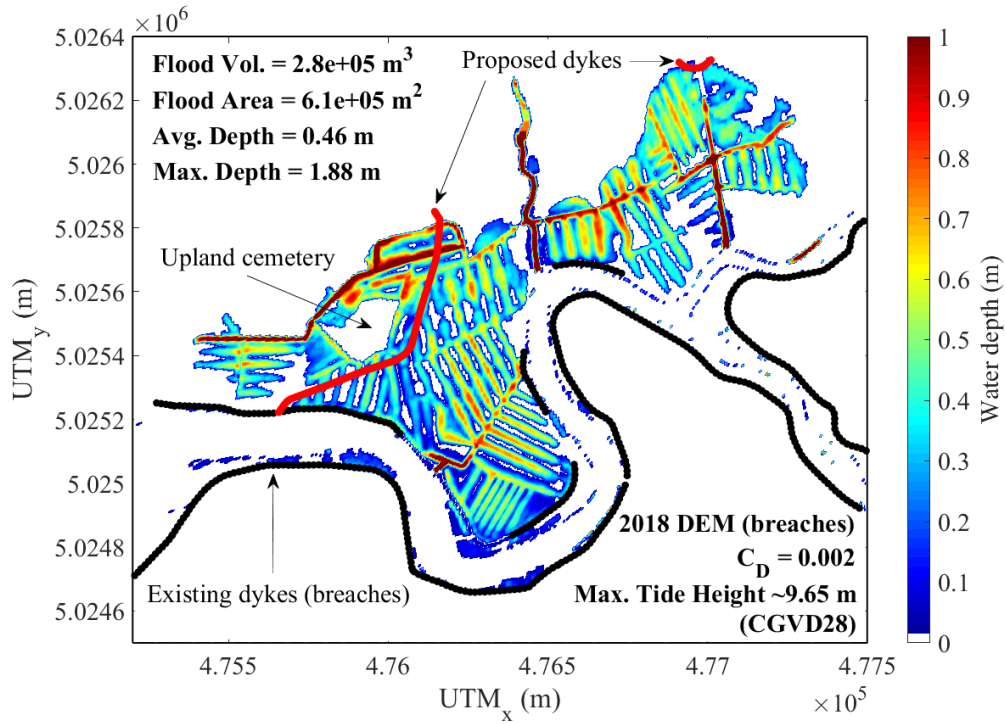


Modelled flood extent and currents 110 minutes after high tide for Tide 2.

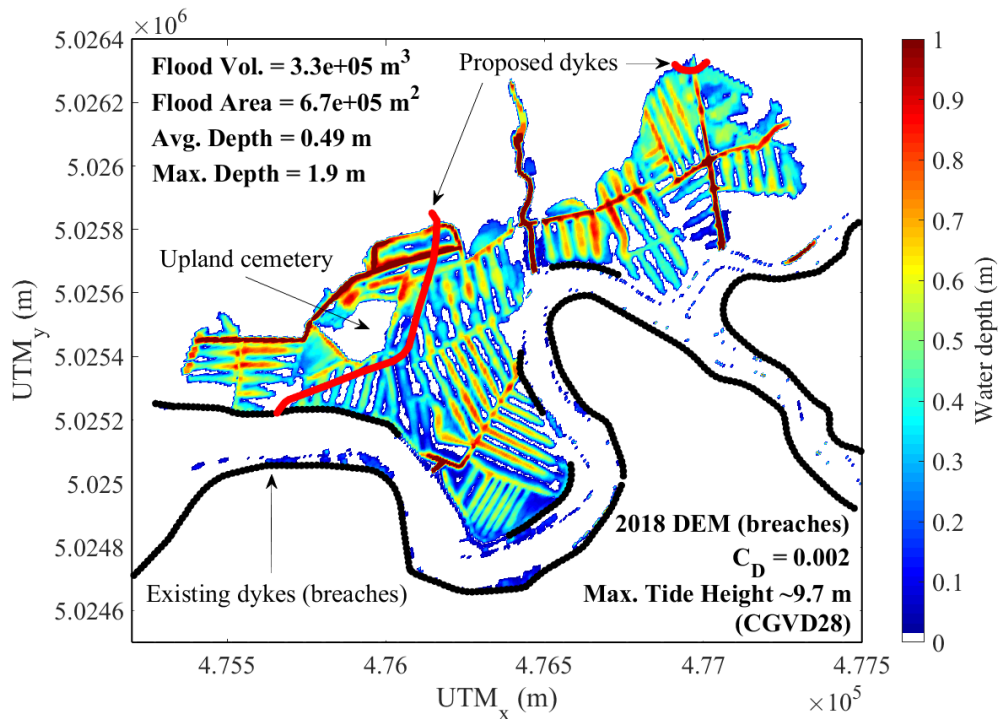


Appendix J

Flood statistics at high tide (Tide 2) for a maximum tide height of 9.65 m (CGVD28).



Flood statistics at high tide (Tide 2) for a maximum tide height of 9.7 m (CGVD28).



Flood statistics at high tide (Tide 2) for a maximum tide height of 9.75 m (CGVD28).

